Lib
4/8/80

Indian J. pure appl. Phys., Vol. 18 No. 7 pp. 465-548
July 1980
CODEN : IJOPAU ISSN : 0019-5596
18 (7) 465-548 (1980)

428
4-8-80

INDIAN JOURNAL OF PURE & APPLIED PHYSICS

Published by
PUBLICATIONS & INFORMATION DIRECTORATE, CSIR, NEW DELHI
in association with
THE INDIAN NATIONAL SCIENCE ACADEMY, NEW DELHI

AA PRE-EMINENCE ...AT THE TOUCH OF A BUTTON...

For advanced programme flexibility, Pye Unicam have partnered their atomic absorption spectrophotometers with DATA CENTRE, an exceptionally low cost, touch button, microprocessing system. For example, you can now achieve even more with the Pye Unicam SP2900... the instrument with a performance that is unequalled by literally any other atomic absorption spectrophotometer.

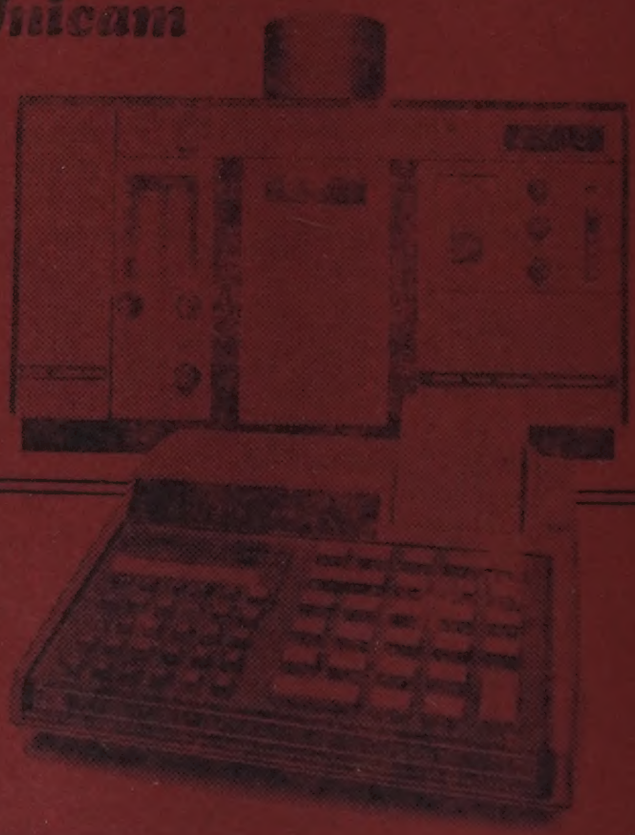

Send for details...

For further details contact:-
Peico Electronics & Electricals Limited
Product Division
Science & Industry
Shivsagar Estate, Block 'A'
Worli, Bombay-400 018

PHILIPS

PEST 4060

Indian Journal of Pure & Applied Physics

VOLUME 18 No. 7 JULY 1980

EDITORIAL BOARD

Dr B A Dasannacharya
Bhabha Atomic Research Centre
Bombay

Prof. B M Deb
Indian Institute of Technology
Bombay

Prof. P Krishna
Banaras Hindu University
Varanasi

Prof. Krishnaji
Allahabad University
Allahabad

Prof. K V Ramanathan
Tata Institute of Fundamental Research
Bombay

Dr S Chandrasekhar
Indian National Science Academy
New Delhi/Raman Research
Institute Bangalore

Prof. A K Saha
Saha Institute of Nuclear Physics
Calcutta

Prof. N C Sil
Indian Association for
Cultivation of Science
Calcutta

Prof. R Srinivasan
Indian Institute of Science
Bangalore

Prof. K Venkata Ramiah
Osmania University
Hyderabad

Dr K L Chopra
Indian National Science Academy
New Delhi/Indian Institute of
Technology New Delhi

Shri Y R Chadha, *Ex-officio* Secretary & Chief Editor

EDITORIAL STAFF

Editors
D S Sastry & K S Rangarajan

Assistant Editors
G N Sarma, J B Dhawan & Tarun Banerjee

Published by the Publications & Information Directorate, CSIR, Hillside Road, New Delhi 110 012

Chief Editor : Y R Chadha

The Indian Journal of Pure & Applied Physics is issued monthly. The Directorate assumes no responsibility for the statements and opinions advanced by contributors. The editorial staff in its work of examining papers received for publication is assisted, in an honorary capacity, by a large number of distinguished scientists, working in various parts of India.

Communications regarding contributions for publication in the journal should be addressed to the Editor, Indian Journal of Pure & Applied Physics, Publications & Information Directorate, Hillside Road, New Delhi 110 012.

Correspondence regarding subscriptions and advertisements should be addressed to the Sales & Distribution Officer, Publications & Information Directorate, New Delhi 110 012.

Annual Subscription
Rs. 100.00 £ 16.50 $ 42.00

Single Copy
Rs. 10.00 £ 1.80 $ 4.50

50% Discount is admissible to research workers and students and 25 % discount to non-research individuals, on annual subscription. Payments in respect of subscriptions and advertisements may be sent by cheque, bank draft, money order or postal order marked payable *only* to **Publications & Information Directorate, New Delhi 110 012.** Claims for missing numbers of the journal will be allowed only if received within 3 months of the date of issue of the journal plus the time normally required for postal delivery of the journal and the claim.

© 1980 The Council of Scientific & Industrial Research, New Delhi.

CSIR SCIENTIFIC PERIODICALS

JOURNAL OF SCIENTIFIC & INDUSTRIAL RESEARCH (monthly)

With a fine record of over 35 years' service to the scientific community, this Journal has grown into India's leading general science periodical. Intended to fulfil the responsibility of helping the research workers to keep themselves abreast of current developments in various fielps of science and technology, the Journal carries editorial features highlighting important scientific events in India and abroad; articles on science policy and management of science; review articles on topics of current research interest; technical reports on international and national conferences; reviews of scientific and technical publications; and notes on major advances in various fields.

Annual subscription	**Rs 60.00**	**£ 10.00**	**$ 25.00**
Single copy	6.00	1.00	2.50

INDIAN JOURNAL OF CHEMISTRY (monthly)

This Journal which is running the 18th year of its publication, Consists of the following two sections.

Section A : This section is devoted to papers in Inorganic, Physical, Theoretical and Analytical Chemistry.

Annual subscription	**Rs 70.00**	**£ 12.00**	**$ 30.00**
Single copy	7.00	1.20	3.00

Section B : This section is devoted to papers in Organic Chemistry including Medicinal Chemistry.

Annual subscription	**Rs 70.00**	**£ 12.00**	**$ 30.00**
Single copy	7.00	1.20	3.00

INDIAN JOURNAL OF PURE & APPLIED PHYSICS (monthly)

This Journal, which is running the 18th year of its publication, is devoted to original research communications (full papers and short communications) in all conventional branches of physics (except radio and space physics).

Annual subscription	**Rs 100.00**	**£ 16.50**	**$ 42.00**
Single copy	10.00	1.80	4.50

INDIAN JOURNAL OF RADIO & SPACE PHYSICS (bimonthly)

This Journal serves as a medium for the publication of original rearch work (full papers and communications) in various areas of radio and space physics.

Annual subscription	**Rs 60.00**	**£ 10.00**	**$ 25.00**
Single copy	12.00	2.00	5.00

INDIAN JOURNAL OF TECHNOLOGY (INCLUDING ENGINEERING) (monthly)

This Journal publishes papers reporting results of original research of applied nature pertaining to unit operations, heat and mass transfer, products, processes, instruments, and appliances, etc. The Journal is of special interest to research workers in the departments of applied sciences in universities, institutes of higher technology, commodity research laboratories, industrial cooperative research institutes, and industrial research laboratories.

Annual subscription	**Rs 60.00**	**£ 10.00**	**$ 25.00**
Single copy	6.00	1.00	2.50

INDIAN JOURNAL OF EXPERIMENTAL BIOLOGY (monthly)

This Journal, devoted to the publication of research communications in the fields of experimental botany, zoology, microbiology, pharmacology, endocrinology, nutrition, etc. is the only one in India with such a wide coverage and scope.

Annual subscription	**Rs 120.00**	**£ 20.00**	**$ 50.00**
Single copy	12.00	2.00	5.00

INDIAN JOURNAL OF BIOCHEMISTRY & BIOPHYSICS (bimonthly)

This Journal, published in association with the Society of Biological Chemists (India), Bangalore, is the only research Journal in India devoted exclusively to original research communications in biochemistry and biophysics.

Annual subscription	**Rs 40.00**	**£ 7.00**	**$ 17.00**
Single copy	8.00	1.40	3.50

INDIAN JOURNAL OF MARINE SCIENCES (quarterly)

Commencing publication from June 1972, this Journal is devoted to research communications (full papers and short communications) pertaining to various facets of marine research, viz. biological, physical, geological and chemical oceanography.

Annual subscription	**Rs 40.00**	**£ 7.00**	**$ 17.00**
Single copy	12.00	2.00	5.00

RESEARCH & INDUSTRY (quarterly)

Intended to serve as a link between science and industry, this Journal is addressed primarily to technologists, engineers, executives and others in industry and trade. It publishes informative original articles containing practical details of processes and products developed in India, which show promise of ready utilization, and technical digests on new processes, products, instruments and testing methods which are of interest to industry. Developments in Indian industry are regularly reported.

Annual subscription	**Rs 24.00**	**£ 4.00**	**$ 10.00**
Single copy	7.25	1.30	3.50

INDIAN JOURNAL OF TEXTILE RESEARCH (quarterly)

Commencing publication from March 1976, this Journal is devoted to the publication of papers reporting results of fundamental and applied researches in the field of textiles.

Annual subscription	**Rs 36.00**	**£ 6.00**	**$ 15.00**
Single copy	12.00	2.00	5.00

Please contact

THE SALES & DISTRIBUTION OFFICER
PUBLICATIONS & INFORMATION DIRECTORATE, CSIR
HILLSIDE ROAD, NEW DELHI 110 012

Indian Journal of Pure & Applied Physics

VOLUME 18 No. 7 JULY 1980

CONTENTS

Solid State Physics

Excitation of Magnetoacoustic Wave by Acoustic Wave in InSb 465
S GUHA, N APTE & P NAMJOSHI

Photolytic Behaviour of P & P^+ Silicon Crystal in HF 468
V P SUNDARSINGH, P P WARNEKAR & G K BHAGWAT

Mössbauer Spectroscopic Studies on Oxides & Hydrated Oxides of Iron ... 473
P P BAKARE, M P GUPTA & A P B SINHA

Kinetics of Growth & Dissolution of Potassium Dihydrogen Phosphate Crystals in Aqueous Solutions 479
M S JOSHI & A V ANTONY

Characterization of Deep Trapping Centres in *n*-Type Liquid Phase Epitaxial GaAs by Hall Effect 483
ASHOK K SAXENA

Superconductivity in Certain Metals 489
S C JAIN & C M KACHHAVA

Chemical Physics

Thermodynamics of Manganese-bearing Binary Substitutional Solutions ... 494
R D AGRAWAL, V N S MATHUR & M L KAPOOR

Isothermal Compressibility Behaviour of Aqueous Solutions of *tert*-Butyl Alcohol at 25°C 499
K J PATIL & D N RAUT

Charge Transfer Interaction of Some Biomolecules with Chloranil 504
R SAHAI & V SINGH

Cationic Effect on the Intramolecular Forces of $B^{VI}O_6$ Octahedra in Ordered Cubic Perovskites $A_2B^{II}B^{VI}O_6$ 510
A N PANDEY, U P VERMA & J R CHOPRA

Molecular Constants of Some Hexahaloanions of Group IV A & Group V A Belonging to O_h Point Group 516
P C SARKAR & G C SINGH

General Physics

Development of a Horizontal Model of Calculable Cross-Capacitor 524
R N DHAR, S L DAHAKE & K CHANDRA

Spectroscopy

Self-Absorption- Free FeI Spectral Lines For Temperature Measurement in the dc Carbon Arc 528
M A EID, K M EL-BEHERY & S M DIAB

CONTENTS

COMMUNICATIONS

I-V Characteristics of Semiconductor-Insulator-Semiconductor Solar Cells ... 532
K SEN, B K JAIN, V K BHATNAGAR & V K SRIVASTAVA

NOTES

On Sarma & Rao's Relation for τ for Binary Mixtures of Polar Liquids ... 535
B B SWAIN

Linear Potential & Phonons in Aluminium 536
K S SHARMA & C M KACHHAVA

Frequency Moments & Viscosities of Liquid Rubidium 538
N S SAXENA & NILIMA LODHA

Force Field & Vibrational Amplitudes of Alkali Metal Halide Dimers Using Electron Gas Model Data 540
V KUMAR, U P VERMA & A N PANDEY

Estimation of Ground State Wavefunctions & ESR Parameters of Cu^{2+} Ion ... 541
B N MISRA, FAUJDAR & RAMESH BABU

Study of the Cluster-size in p-Nucleon Intraction at 70 GeV/c 544
D C GHOSH, S C NAHA, J ROY, K SENGUPTA & M BASU

Letters to the Editor

Nuclear-Decay Data—The Statement of Uncertainties 548
W B MANN

Indian Journal of Pure & Applied Physics
Vol. 18, July 1980, pp. 465-467

Excitation of Magnetoacoustic Wave by Acoustic Wave in InSb*

S GUHA†, N APTE & P NAMJOSHI
School of Studies in Physics, Vikram University, Ujjain

Received 4 *April* 1979

The possibility of excitation of a magnetosonic wave by an acoustic wave of transverse polarization propagating in a direction perpendicular to a static magnetic field is investigated theoretically, in a piezoelectric semiconductor like InSb at 77 K. The propagation characteristics of the coupled wave (acoustic and magnetoacoustic) have also been studied. The numerical analysis has been done for complex k values of the coupled wave for real values of ω and different values of dc magnetic field and from this, the dependence of the refractive index and the absorption coefficient on dc magnetic field has been studied.

1. Introduction

Alfven wave has been studied theoretically and experimentally in semimetals like Bi by many workers.[1] The coupling of compressional Alfven wave with magnetoacoustic wave has been studied experimentally[2,3] as well as theoretically.[4,5] Guthman *et al.*[6] have studied the propagation of magnetoacoustic mode in Bi at low temperatures. No study has been made regarding the excitation of magnetoacoustic wave in semiconductors by an acoustic mode. In piezoelectric semiconductors, if an acoustic wave propagates in the presence of a magnetic field, there is a possibility of excitation of magnetoacoustic mode. In the present paper, we have investigated analytically this possibility and studied the propagation characteristics of the coupled (acoustic and magnetoacoustic) wave.

2. Theoretical Formulation

We use the hydrodynamic model of the semiconductor-plasma and assume homogeneous and isotropic crystal in which an acoustic wave is propagating along the Z-direction, electric polarization of this wave being in X-direction and the magnetic field $\mathbf{B}_0$ is applied along the Y-direction.

The starting equations are

$$m^* \frac{d\mathbf{v}}{dt} = q\left[\mathbf{E}_1 + \mathbf{v}\times\mathbf{B}\right] - m^*\nu\mathbf{v} - \frac{k_B T \vec{\nabla} n_1}{n_0} \quad \ldots(1)$$

$$\mathbf{J} = q\,(n_0+n_1)\,(\mathbf{v}_0+\mathbf{v}_1) \quad \ldots(2)$$

$$\rho \frac{\partial^2 \mathbf{u}}{\partial t} = C\frac{\partial^2 \mathbf{u}}{\partial x^2} - \beta\frac{\partial \mathbf{E}_1}{\partial x} \quad \ldots(3)$$

$$\nabla \times \mathbf{H} = \mathbf{J} + \mathbf{D} \quad \ldots(4)$$

$$\mathbf{D} = \epsilon_0\,\epsilon_L\,\mathbf{E}_1 + \beta\,\mathbf{S} \quad \ldots(5)$$

$$\mathbf{S} = \frac{\partial \mathbf{u}}{\partial x} \quad \ldots(6)$$

$$\frac{\partial \rho}{\partial t} + \nabla.\mathbf{J} = 0 \quad \ldots(7)$$

The functional dependency of all dynamic quantities involved is taken to be $\exp i\,(\omega t - kz)$. The notations used are explained in Steele and Vural.[7]

From Eqs. (1) and (2), we obtain the time-dependent current J as

$$J = \left[\frac{i\,\omega_{pe}^2\,\epsilon\,\bar{\omega}_e\,R_e}{\omega\,\omega_{ce}^2} + \frac{i\,\omega_{ph}^2\,\epsilon\,\bar{\omega}_h\,R_h}{\omega\,\omega_{ch}^2}\right] E_1 \quad \ldots(8)$$

where $\omega_{ce,h} = q\,B_0/m^*_{e,h}$ is the cyclotron frequency of the carriers, $\omega^2_{pe,h} = n_0\,q^2/\epsilon\,m^*_{e,h}$ is the plasma frequency of the carriers, $\bar{\omega}_{e,h} = (\omega - k\,v_{0e,h})$ is the Doppler shifted frequency. Also

$$R_{e,h} = \bar{\omega}_{e,h} - i\nu_{e,h} - \frac{k^2\,k_B\,T}{m^*_{e,h}\,\bar{\omega}_{e,h}}$$

and $\nu_{e,h}$ is the collision frequency of the carriers. The subscripts e and h correspond to electron and the hole respectively.

From Eq. (3) we have

$$u = -\frac{i\,k\,\beta\,E_1}{\rho\,(\omega^2 - k^2\,v_s^2)} \quad \ldots(9)$$

and from Eqs. (9), (6) and (5), we get

$$\mathbf{D} = \epsilon_0\,\epsilon_L\,\mathbf{E}_1 - \frac{k^2\,\beta^2\,\mathbf{E}_1}{\rho\,(\omega^2 - k^2\,v_s^2)} \quad \ldots(10)$$

* Work partially supported by the University Grants Commission, New Delhi

† Present address : Department of Physics, Ravishankar University, Raipur

Using Eqs. (4), (8) and (10), we obtain the dispersion relation for the coupled wave as

$$\left(k^2 v_s^2-\omega^2\right)\left[k^2C_1^2-\omega^2-\frac{\omega_{pe}^2 R_e \bar{\omega}_e}{\omega_{ce}^2}-\frac{\omega_{ph}^2 R_h \bar{\omega}_h}{\omega_{ch}^2}\right] = \omega^2 k^2 v_s^2 K_p^2 \quad ...(11)$$

where $K_p^2 = \beta^2/\rho\, v_s^2$ is the electromechanical coupling constant for the crystal. We have assumed that $\omega_c > \omega$, $\omega > \nu$.

In the absence of piezoelectric coupling $\left(k_p^2 = 0\right)$, the solutions of the dispersion relation (11) correspond to : (i) an acoustic wave with the dispersion relation

$$k^2 v_s^2 - \omega^2 = 0 \quad ...(12)$$

and

(ii) an electromagnetic mode with the dispersion relation

$$k^2 C_1^2-\omega^2-\frac{\omega_{pe}^2 R_e \bar{\omega}_e}{\omega_{ce}^2}-\frac{\omega_{ph}^2 R_h \bar{\omega}_h}{\omega_{ch}^2} = 0 \quad ...(13)$$

The phase velocity of the mode given by Eq. (13), for collisionless case is given by

$$v_\phi^2 = \frac{\omega^2}{k^2} = C_1^2 \frac{v_A^2 + v_T^2}{v_A^2 + C_1^2} \quad ...(13A)$$

where v_T is the thermal velocity of the carriers and v_A is the velocity of the Alfven wave. In Eq. (13A) if $v_A \gg v_T$, i.e. at high magnetic fields

$$v_\phi = v_A$$

which identifies an Alfven wave. For low magnetic fields $(v_A \ll v_T)$, $v_\phi = v_T$

which is no longer an electromagnetic mode but represents a nonlocal acoustic-like mode propagating with a velocity near the thermal velocity of the carriers. The two modes couple at magnetic fields when the thermal pressure is equivalent to the magnetic pressure[3] and the result is a magnetoacoustic mode.

To study the effect of dc electric field we have considered the momentum transfer of the electron due to acoustic phonons and the energy transfer due to optical phonons. The electron temperature is obtained from the principle of conservation of energy. On solving the zero-order momentum equation, we get the components of drift velocity as

$$v_{0xe} = \frac{-e\,(\nu_e E_{0x} + \omega_{ce} E_{0z})}{m_e^*\,(\nu_e^2 + \omega_{ce}^2)} \quad ...(14)$$

and

$$v_{0ze} = \frac{-e\,(\nu_e E_{0z} - \omega_{ce} E_{0x})}{m_e^*\,(\nu_e^2 + \omega_{ce}^2)} \quad ...(15)$$

The collision frequency for momentum transfer for the electron is given by

$$\nu_e = \left(\nu_{e0}^2 \frac{T_e}{T_0}\right)^{1/2} \quad ...(16)$$

where ν_{e0} is the collision frequency at $T_e = T_0$. For hole, $\nu_h = \nu_{h0}$ where ν_{h0} is the collision frequency at T_0, the lattice temperature.[8] From the energy conservation principle and Eqs. (14), (15) and (16), we get

$$E_0^2 = \left(\frac{2 k_B \theta_D}{\pi m_e^*}\right)^{1/2} e F_R \frac{[\exp.(x_0 - x_e) - 1]}{(\exp. x_0 - 1)} x_e^{1/2} \exp x_e/2\, K_0(x_e/2)\, m_e^* \frac{(\nu_e^2 + \omega_{ce}^2)}{e^2 \nu_e} \quad ...(17)$$

where $$e F_R = \frac{m_e^* e^2 \hbar \omega_l}{\hbar^2}\left(\frac{1}{\epsilon_\infty} - \frac{1}{\epsilon_l}\right)$$

$$x_0 = \theta_D/T_0$$

and

$$x_e = \theta_D/T_e$$

The symbols are those given in Conwell's book.[8]

3. Results and Discussion

From the above analysis it is clear that a magnetoacoustic wave can be excited by an acoustic wave when the magnetic pressure is equivalent to the kinetic pressure. Propagation characteristics of the coupled mode in InSb in the hot carrier region have been studied using the following parameters of the crystal :

$$m_e^* = 0{\cdot}013\, m_0$$

$$m_h^* = 0{\cdot}4\, m_0$$

$$T_0 = 77 \text{ K}$$

$$\nu_{e0} = 3{\cdot}5 \times 10^{11} \text{ sec}^{-1}$$

$$\nu_{h0} = 4{\cdot}4 \times 10^{11} \text{ sec}^{-1}$$

Eq. (11), has been solved numerically with the help of IBM 360/44 computer and the roots of $k = (k_r + i k_i)$, corresponding to the coupled wave for real values of ω were obtained. The refractive

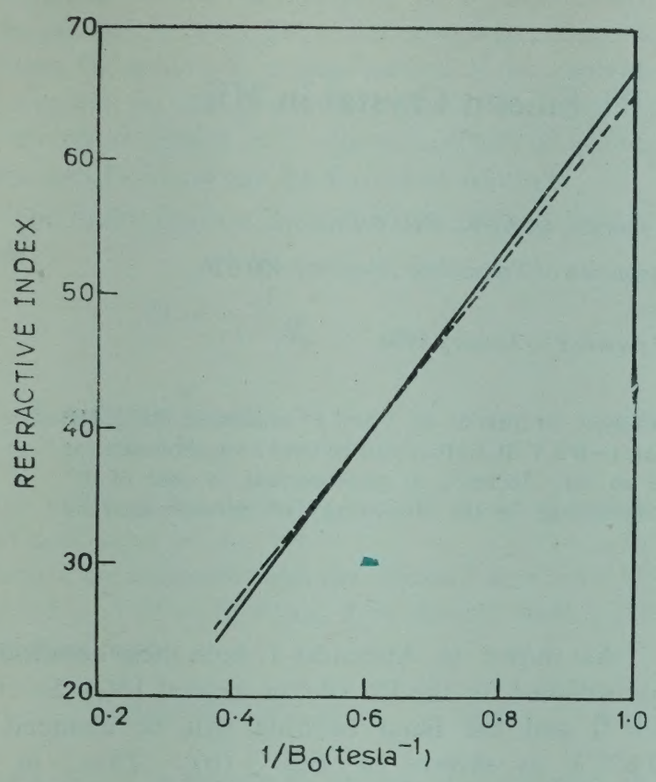

Fig. 1—Variation of refractive index with $1/B_0$ at $\omega=0{\cdot}5\times10^{13}$ Hz, $E=14400$ V m^{-1} and $\theta=0°$

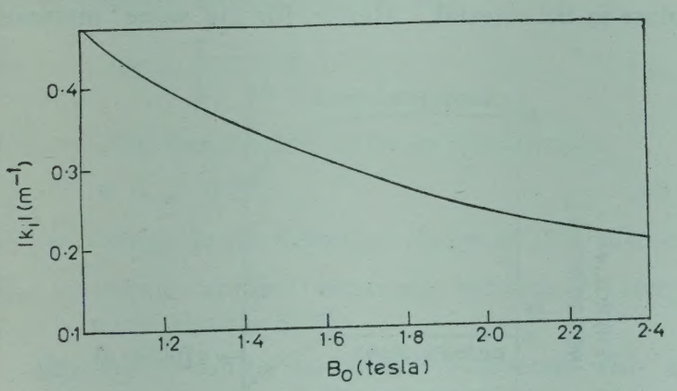

Fig. 2—Variation of $|k_i|$ with applied magnetic field (B_0) at $\omega=0{\cdot}5\times10^{13}$ Hz, $E_0=14400$ V m^{-1}

indices ($n=c\,k_n/\omega$) have been calculated and plotted against the magnetic field (Fig. 1) which shows that the refractive index of the coupled mode decreases with the increasing magnetic field. The attenuation constant is found to be smaller at higher magnetic fields (Fig. 2). The effect of high electric field on the refractive index as well as attenuation constant was found to be small. It is seen that wavenumber of the order of 10^7-10^5 m^{-1} of acoustic wave excites magnetosonic wave of wavenumber within the range of 10^5-10^2 m^{-1}.

Acknowledgement

It is a pleasure to thank Dr D R Kulkarni and Dr K S Rao of the Physical Research Laboratory, Ahmedabad, for their help in computation work. Two of the authors (P N and N A) thankfully acknowledge the financial support from CSIR, New Delhi. They are also thankful to Dr P K Sen and Dr S K Ghosh for many helpful discussions.

References

1. Buchsbaum S J, *Proc. Conf. Plasma effects in Solids* (Dunod, Paris), 1965, 3.
2. Yokota I, *J. phys. Soc. Japan*, **21** (1966), 1851.
3. Luptakin W L & Nanney C A, *Phys. Rev. Lett.*, **20** (1968), 212.
4. Tatsuki Ogino & Susumu Takeda, *J. phys. Soc. Japan*, **43** (1977), 1371.
5. Prokolab M, *Physica*, **82C** (1976), 86.
6. Guthmann C, D'Haenens J P & Libchaber A, *Phys. Rev.*, **B4** (1971), 1538.
7. Steele M C & Vural, *Wave interactions in solid state plasmas* (McGraw-Hill, New York), 43-45, 134-138.
8. Conwell E M, High field transport in semiconductors, in *Solid state physics* (Academic Press, New York), 1967, 159.

Indian Journal of Pure & Applied Physics
Vol. 18, July 1980, pp. 468-472

Photolytic Behaviour of P & P+ Silicon Crystal in HF

V P SUNDARSINGH, P P WARNEKAR & G K BHAGWAT
Department of Electrical Engineering, Indian Institute of Technology, Bombay 400 076

Received 7 *March* 1979; *revised received* 16 *January* 1980

Investigations were carried out to determine photolytic properties of P and P^+ silicon in 0·5% HF solutions. It is shown that below the etching potentials (−0·3 V SCE) they can be used as a photocatalyst generating much higher photocurrents than those reported so far. Increase in photocurrent in case of P^+ silicon is explained in terms of field generated carriers and the change in the free-energy of minority carriers under illumination.

1. Introduction

p-Type silicon in salt water has been experimented for photolysis of water by Rodica *et al.*[1] Photocurrents reported in their paper are of small magnitudes and the reason for this may be the presence of SiO_2 on silicon surface which cannot be reduced even in the cathodic conditions.[2] *n*-Type silicon which shows good photolytic properties in anodic direction cannot be used in HF electrolyte because of predominance of etching reaction[2] under illumination. On the other hand, *p*-type silicon if used in the cathodic direction, does not show any electrochemical reaction other than the photolysis of water and hence P and P^+-silicon crystals are investigated here for their photolytic properties.

2. Theory

When a *p*-type silicon crystal is immersed in an electrolyte, an interface is formed and the energy levels at the interface are shown in Fig. 1. The presence of surface states on the silicon surface makes the bands bend downwards for *p*-type silicon crystals resulting in a built-in potential. A P-crystal which has low doping concentration can support a large built-in potential without resulting in avalanche multiplication or tunnelling. But a P^+-crystal may not be able to support large voltage because tunnelling can occur when the valence band level in the bulk of the semi-conductor coincides with the H^+/H_2O level and hence the bending will be clamped at this position. Two conditions must be satisfied for this, viz. (a) the flat-band potential should be greater than the potential difference between H^+/H_2O level and the valence band level at the surface, (b) the depletion width must be sufficiently small so that tunnelling is possible.

As shown in Appendix-1, both these conditions are satisfied for the P^+ silicon crystal [$N_A = 5 \times 10^{19}$ cm^{-3}] and the band bending will be clamped at 0·637 V as shown in Fig. 1 (b). Thus, in a P^+-crystal one must observe a large dark current. Further, avalanche multiplication will also take place in this crystal. Hence, for the same intensity

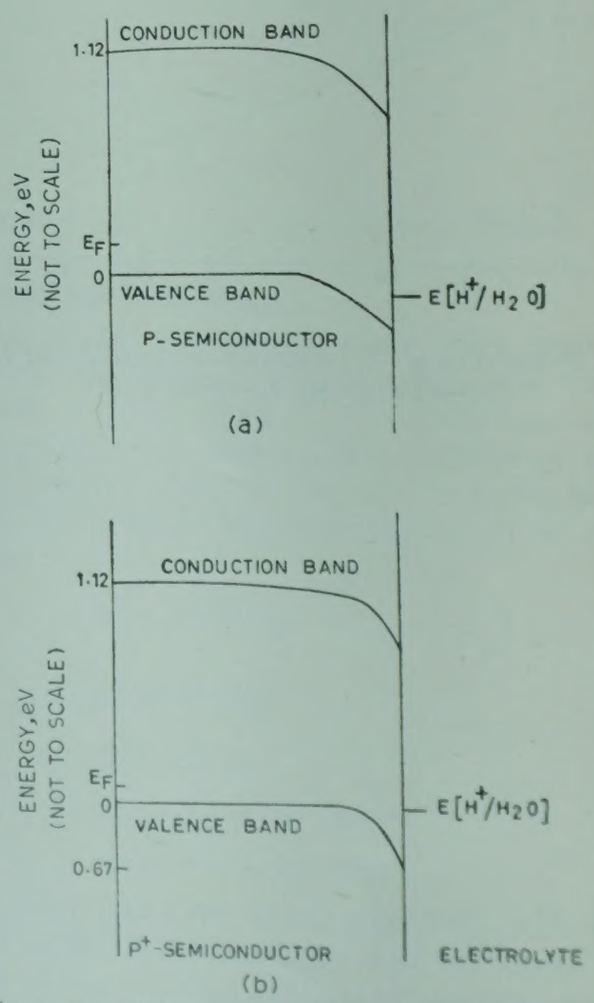

Fig. 1—Equilibrium band diagram for P and P^+ silicon crystal and HF electrolyte system in dark

of illumination, the photocurrent in P^+-crystal will be larger due to two factors (i) free-energy change of carriers, (b) avalanche multiplication of the generated carriers in the depletion region. An equation for the photocurrent in P^+-silicon in terms of photocurrent in P-silicon can be derived as follows.

The multiplication factor[3] M can be determined from

$$M = \frac{1}{1 - N_s} \qquad ...(1)$$

$$\text{where } N_s = \int_0^W \alpha(E)\, dx \qquad ...(2)$$

W = width of the depletion region, $\alpha(E)$ = ionization coefficient $= A\, e^{-b/E}$ ...(3)

A and b are constants and for silicon,[5] $A = 3{\cdot}8 \times 10^6$ cm^{-1}, $b = 1{\cdot}75 \times 10^6$ V/cm, E = electric field in the depletion region

$$E = \frac{q N_a}{\epsilon_r \epsilon_0}[W - x] \qquad (4)$$

In Eq. (4), q = electronic charge, ϵ_r = relative dielectric constant, ϵ_0 = permittivity of free-space, N_a = acceptor doping density, and

$$W = \left[\frac{2\epsilon_r \epsilon_0 V_{P^+}}{q N_a}\right] \qquad ...(4a)$$

V_{P_+} = (Flat band potential under illumination $+ V_{ap} - 0{\cdot}24$) ...(4b)

V_{P_+} = voltage in the depletion region of P^+ silicon

V_{ap} = voltage applied externally between P^+ electrode and the SCE

Eqs. (1)-(4) can be numerically evaluated with a computer using Simpson's rule and hence M evaluated. Hence, considering only the electrons, the photocurrent in case of P^+ crystal relative to P-crystal is given by

$$I_{P+1} = M I_{P1} + I_{P_+} \qquad ...(5)$$

where I_{P+1} = photocurrent in P_+-crystal, I_{P1} = photocurrent in P-crystal, I_{P^+} = dark current in case of P^+-crystal

Since the holes generated in the depletion region will also get multiplied resulting in electron generation, this portion of the current is taken into account as follows :

The light intensity variation in silicon is given by

$$I(x) = I_0 \exp(-\alpha x) \qquad ...(6)$$

In Eq. (6)

I_0 = intensity of light at the surface

α = absorption coefficient

Hence, the fraction of carriers generated in the depletion region is given by

$$f = \frac{I_0 \int_0^W \exp(-\alpha x)\, dx}{I_0 \int_0^\infty \exp(-\alpha x)\, dx} \qquad ...(7)$$

$$= 1 - \exp(-\alpha W) \qquad ..(8)$$

Assuming the same $\alpha(E)$ for holes for simplicity, the total current is given by

$$I_{P+1} = M I_{P1}(1 + f) + I_{P_+} \qquad ...(9)$$

Finally, the change in free-energy for electrons in P^+-semiconductor under illumination[6] is taken into account as follows :

$$\left.\begin{array}{l}\text{Change in free-energy}\\ \text{of electron}\end{array}\right\} = R\,T \ln\left(1 + \frac{\Delta n}{n_0}\right) \qquad ..(10)$$

In Eq. (10)

Δn = change in electron concentration (minority carrier)

n_0 = equilibrium electron concentration (minority carrier concentration)

Hence, the ratio of change of free-energy for electron in case of P^+ and P-crystal is

$$A = \frac{\ln\left(1 + \frac{\Delta n\, M}{n_0}\right)}{\ln\left(1 + \frac{\Delta n}{n_0}\right)} \qquad ...(11)$$

Eq. (10) is valid only if the carriers generated in both the cases are same.

Hence, the photocurrent in P^+ crystal is given by

$$I_{P+1} = I_{P_+} + A M I_{P1}(1 + f) \qquad ...(12)$$

In Eq. (12) it is assumed that the photocurrent is directly proportional to free-energy change of the minority carriers. The following experiment was conducted to determine the validity of the equation.

3. Experimental Details and Results

Experiments were conducted on P, P^+ and N^+ single crystal silicon to determine their photolytic properties. The resistivities of P, P^+ and N^+ crystals are 10, 0·003 and 0·01 ohm-cm respectively. They were chemically polished using CP-4 solution and ohmic contacts were taken from one side by bonding a small molybdenum disk using appropriate alloys and then attaching a lead wire to these disks. Except for an area of one square centimetre, rest of the surface was covered with Apiezon wax to prevent

secondary reactions. The *I-V* characteristics were then taken in 0·5% HF solution using an electrochemical cell which has a platinum counter electrode, the above prepared Si working electrode, a saturated calomel reference electrode and a static potentiostat.

Fig. 2 shows the *I-V* characteristics of different silicon crystals with and without illumination from which it is clear that above −0·3 V (SCE), silicon etching reaction predominates resulting in film formation.[2] This is indicated by the P-type silicon dark current, where, above −0·3 V (SCE) approximately, etching reaction predominates as shown by anodic currents. Thus, if P-type silicon is to be used for photolysis in HF, it should be biased below −0·3 V (SCE) to overcome the etching reaction. Fig. 2 also shows that with illumination the current flowing in P-type silicon is more than that in n-type silicon proving that light has transferred some of its energy for generating hydrogen. Further, the magnitude of current is more than that observed by Rodica *et al.*[1] demonstrating the superiority of P-type silicon in HF for photolysis. These *I-V* characteristics below the etching range are highly reproducible. Hydrogen evolution was checked by collecting the gas and igniting it.

As explained in the theory one observes that the photocurrent in P^+-silicon is higher than that in P-silicon. To determine whether Eq. (12) is valid the parameters are determined as follows :

M is determined by solving Eqs. (1)-(4) in a computer for the following constants :

$$A = 3{\cdot}8 \times 10^6\ \text{cm}^{-1} \qquad \epsilon_r = 12$$

$$b = 1{\cdot}75 \times 10^6\ \text{V/cm} \qquad \epsilon_0 = 8{\cdot}85 \times 10^{-14}\ \text{F/cm}$$

$$N_a = 5 \times 10^{19}/\text{cm}^3 \qquad q = 1{\cdot}6 \times 10^{-19}\ \text{Coul}$$

Flat-band potential under illumination for P^+-crystal is determined by plotting the Mott-Schottky curve for the same intensity of light and is found to be 0·29 V (SCE). The variation of M with voltage in the depletion region (V_{P^+}) is shown as follows the next page.

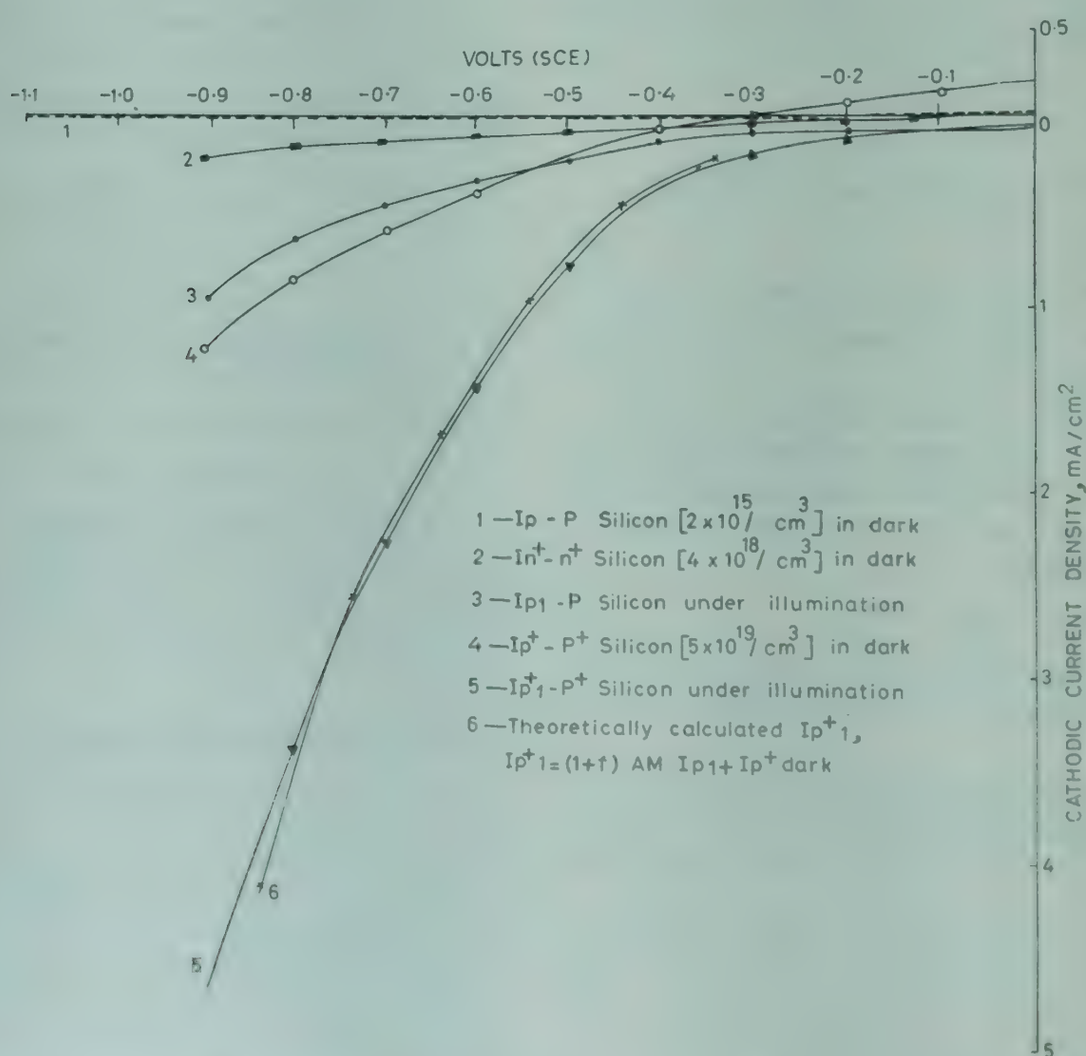

Fig. 2 *I-V* characteristics of single crystal silicon in 0·5% HF solution. Tungsten lamp intensity is approximately 50 m W/cm²

V_{P^+}	M for $5\times10^{19}/cm^3$ Conc.
0·94	2
0·84	1·74
0·74	1·56
0·64	1·398
0·54	1·26
0·44	1·14

A is determined from Eq. (11) and is evaluated for the following conditions :

$$P^+ = 5 \times 10^{19}\ cm^{-3}$$
$$P = 2 \times 10^{15}\ cm^{-3}$$
$$\Delta n = 0{\cdot}8 \times 10^{13}\ cm^{-3}$$

Value of n is measured from the change in resistivity of high resistivity silicon crystal when light used in the experiment illuminates the crystal. The actual value during the experiment will be less than this value because external photocurrent will reduce the concentration of carriers. This variation is not taken into account in determining A. However, since the efficiency of photolysis is small, the reduction will also be small.

Value of f is evaluated to be 0·003 for $\alpha = 4500$ and $W = 52$ Å. Since this is small it is neglected in Eq. (12).

Using the above values, Eq. (12) is evaluated and plotted in Fig. 2. The match between experimental and theoretical curve is very good, clearly proving the importance of free-energy change for minority carriers in semiconductors.

4. Conclusion

This experimental investigation proves that P-type silicon in HF electrolyte can be used as a photo-catalyst if it is biased below the etching potential and the observed photocurrents are larger than that in salt water. The increased current in P^+-crystal when compared with P-crystal is because of avalanche multiplication and change in free-energy of minority carriers confirming the importance of free-energy change for photolysis using semiconductors.

References

1. Rodica Condea M, Kastner M, Goodman R & Hiekok N, *J. appl. Phys.*, 47 (1976), 2724
2. Holmes H, *The electrochemistry of semiconductors*, (Academic Press, London), 1962.
3. Seymour J, *Physical electronics*, (Pitman Publishing, Great Britain), 1972.
4. Moll J L, *Physics of semiconductors*, (McGraw-Hill, New York), 1964.
5. Sze S M, *Physics of semiconductors*, (John Wiley, New York), 1969.
6. Gerischer H, *J. electrochem. Soc.*, 11 (1966), 1174.
7. Mollers F & Memming R, *Berichteder Bunsen : Gesellsehaft*, 76 (1972), 469.

Appendix 1

Field Condition at the Surface of Silicon in Contact with an Electrolyte

To determine the field condition existing in the depletion layer of P^+ silicon, it is necessary to know the flat-band potential for P^+-crystal. Since the P^+ dark current is high (Fig. 2) it is difficult to determine the flat band potential (U_{FB}) by plotting Mott-Schottky plot. Hence, first, U_{FB} for P-crystal (10 ohm-cm) is determined by plotting series capacitance versus voltage characteristics as shown in Fig. A1. From this, U_{FB} for 10 ohm-cm P-type silicon is given by

$$U_{FB} = (1{\cdot}58 - 0{\cdot}06\ pH)\ (SCE) \quad ...(A.\ 1)$$

For 2·5 pH, $U_{FB} = 1{\cdot}43$ V

The flat band potential for P^+ silicon can be determined by following the same procedure of F Mollers *et al.*[7] Flat-band potential depends on the acceptor concentration of the semiconductor. Increasing the acceptor concentration by a factor of 10, the distance between valence band and the Fermi level in the bulk is decreased by 60 mV. Since the energy bands are fixed at the surface, the band bending is larger by 60 mV. Hence,

$$U_{FBP^+} = U_{FBP} + 0{\cdot}06 \log \frac{N_{AP^+}}{N_{AP}} \quad ..(A.\ 2)$$

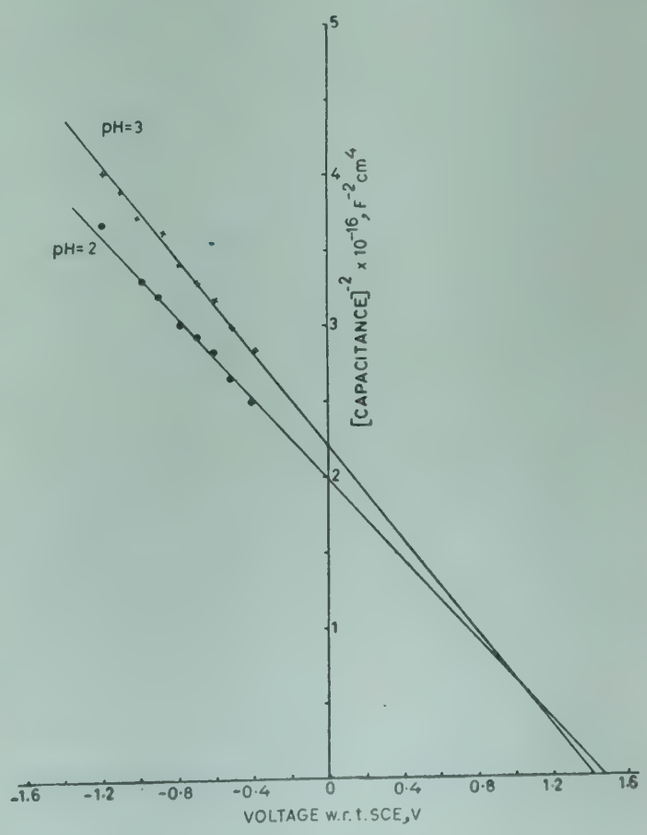

Fig. A1—Mott-Schottky plot for P silicon (10 ohm-cm) in in 0·5% HF

for $N_{AP^+} = 5 \times 10^{19}$ cm^{-3}

$N_{AP} = 2 \times 10^{15}$ cm^{-3}

$U_{FBP^+} = 1{\cdot}69$ V (SCE)

P^+-crystal cannot support this voltage in the depletion region because tunnelling will take place beyond 0·67 V as shown in Fig. A1. Hence, the voltage in the depletion region is given by

$$| V_{P^+} | = (0{\cdot}67 + V_{ap} - 0{\cdot}24)$$
$$= (V_{ap} + 0{\cdot}43) \qquad \text{...(A. 3).}$$

Thus, the field condition in the depletion region should be calculated corresponding to Eq. (A. 3), The maximum electric field in the depletion region of *p*-type semiconductor is given by

$$E_{max} = \frac{q\, N_a\, W}{\epsilon_r\, \epsilon_0} \qquad \text{...(A. 4)}$$

In Eq. (A. 4)

$$W = \left[\frac{2\, \epsilon_r\, \epsilon_0\, V_{P^+}}{q\, N_a} \right]^{1/2}$$

Eq. (A. 4) is evaluated for

$N_a = 5 \times 10^{19}$ cm^{-3}, $V_{P^+} = 1$ V and $W = 52$ Å,

then $E_{max} = 3{\cdot}84 \times 10^6$ V/cm.

This field is well above the avalanche breakdown field[3] in silicon which is 5×10^5 V/cm. Hence, under illumination, avalanche multiplication can take place resulting in additional electron hole pairs in P^+ crystal. The electrons thus generated can take part in breaking H_3O^+ ions. Since W is also small, tunnelling will also take place resulting in large dark current in P^+ crystal.

Indian Journal of Pure & Applied Physics
Vol. 18, July 1980, pp. 473-478

Mössbauer Spectroscopic Studies on Oxides & Hydrated Oxides of Iron

P P Bakare, M P Gupta & A P B Sinha
National Chemical Laboratory, Poona 411 008

Received 6 *March* 1979

Mössbauer spectra of the thin film of iron hydroxide formed at the surface of a solution of ferrous ammonium sulphate on its exposure to ammonia vapour as well as the products formed on stepwise dehydration of this film, were studied. These materials were characterized by chemical analysis, X-ray diffraction, thermal analysis and saturation magnetization. The dehydration of the surface film [$Fe(OH)_3$] was found to lead, successively, to the formation of $Fe_2O(OH)_4$, β-FeOOH and a mixture of α- and γ-Fe_2O_3. β-FeOOH, when heat treated at 800 K for 60 hr, converted to α-Fe_2O_3. Mössbauer spectra of these materials, heated at different temperatures reveal interesting new results.

1. Introduction

The oxides of iron extensively studied are crystalline FeO; α-, β-, γ- and ε-Fe_2O_3 and Fe_3O_4.[1] They find varied uses, e.g. in the preparation of magnetic materials, catalysts, pigments and as raw materials for many chemical preparations. The properties of these oxides are sensitive to the methods of preparation. Thin insoluble films formed on the surface of iron salt solution seemed to show new interesting properties. They were amorphous to start with and on heating they lost bound water and developed crystalline structure. Mössbauer spectra of these compounds were particularly interesting. In this paper, we report our results on the study of amorphous $Fe(OH)_3$, $Fe_2O(OH)_4$, β-FeOOH and products of dehydration.

2. Experimental Details

Samples were prepared from the thin film[2] formed on the surface of the solution of ferrous ammonium sulphate in distilled water (2 to 5%) enclosed in an atmosphere of ammonia for a few minutes. This thin film was collected on a glass plate and washed with distilled water repeatedly. The film was dried below 370 ± 5 K and then scraped out: (I) This sample was indexed as B_1. (II) The scraped off material B_1 heated at 570 to 770 K for 3 hr was indexed as B_2 and (III) B_1 heated at 820 ± 5 K for 4 and 60 hr were indexed as B_{3-1} (a) and B_{3-1} (b), for 3 hr as B_{3-2} and at 970 + 5 K for 50 hr as B_{3-3}. The above materials were studied by X-ray diffraction, thermoanalytical methods, Mössbauer spectroscopy and saturation magnetization measurements for their chemical and magnetic properties.

Powder X-ray diffraction patterns were obtained by using Debye-Scherrer camera of 9 cm diameter and with Cu-$K\alpha$ radiation filtered through nickel foil. Diffraction pattern of sample B_1 (dried below 370 K) and B_2 (i.e. B_1 heated at 570 K, 670 K and 770 K for 3 hr) did not contain any sharp line. However, X-ray diffraction pattern of B_3 sample (i.e. B_1 heated at 820 K) exhibited a crystalline nature and was found to be a mixture of α- and γ-Fe_2O_3.

Samples B_1 and B_2 were chemically analyzed for their ferrous and ferric ions volumetrically[3] by dissolving them in conc. H_2SO_4 and titrating with 0·1*N* $K_2Cr_2O_7$ before and after reduction with $SnCl_2$. Only sample B_2 showed presence of very slight ferrous iron ≃ 0·4% while rest of it was Fe^{3+}.

Thermogravimetric measurements[4] were carried out on a MOM-Budapest Derivatograph, type 00-102, of Hungary. Samples of 100 mg were taken and DTA, TGA and DTG graphs were recorded simultaneously on a photographic paper.

Mössbauer spectra of the samples were taken on a Mössbauer spectrometer (MBS-35 of Electronic Corporation of India) using electromechanical drive which was operated in constant acceleration time mode coupled to a ND 100 multichannel analyzer. A 3 mCi ^{57}Co source in palladium matrix was used throughout the experiments.

Saturation magnetization measurements were done by ponderometric method described by Rathnaue and Snoek.[5] The measurements of saturation magnetization were carried out in a field of 10 kOe in 1·5 in. pole gap. The calibration was carried out using pure nickel metal as standard.

3. Results and Discussion

3.1 Thermoanalytical Studies

The DTA, TGA and DTG graphs of sample $B_1[Fe(OH)_3]$ are shown in Fig. 1. A hump in the DTA graph in the temperature range 323-513 K indicated an endothermic reaction taking place. In this temperature range the weight loss as calculated from the TGA graph is 8%. This loss is indicative of a loss of one molecule of water per two molecules of $Fe(OH)_3$ which would lead to the conversion of the sample to $Fe_2O(OH)_4$. The reaction can be explained by the following equation

$$2Fe(OH)_3 \xrightarrow{heat} Fe_2O(OH)_4 + H_2O \quad ...(1)$$
$$(Fe_2O_3 \cdot 2H_2O)$$

The reaction seems to be completed when the sample is slowly heated to about 523 K.

The product $Fe_2O(OH)_4$ formed, when further heated underwent another endothermic reaction between 523 and 573 K, shown by a sharp DTA peak at 553 K. The calculated weight loss in this temperature range is also 8% of the original weight. The new product formed is identified as β-FeOOH. The reaction can be represented as

$$Fe_2O(OH)_4 \xrightarrow{heat} 2\beta FeOOH + H_2O \quad ...(2)$$

The total weight loss of 16% agrees well with the theoretical value of 16·846% on the basis of the above equations. Sample β-FeOOH is indexed as B_2.

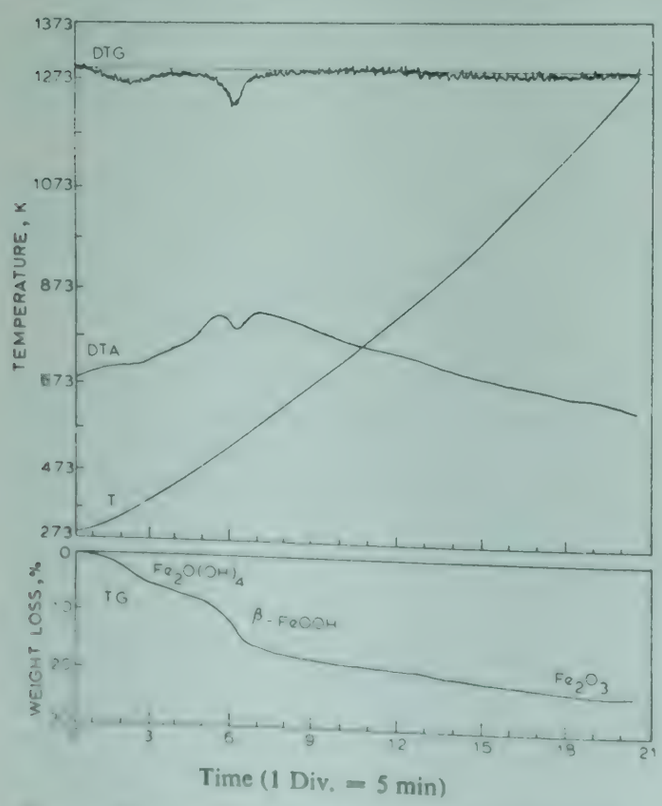

Fig. 1—The DTA, TGA and DTG graphs of sample B_1

The 3rd endothermic reaction takes place when the sample is further heated from 663 K. In this reaction, β-FeOOH is slowly converted to Fe_2O_3 (sample B_3) which is identified as a mixture of α- and γ- phases by Mössbauer spectrometry and X-ray diffraction pattern. The β-FeOOH sample suffers a weight loss of 5% which agrees with the calculated value of 5·0645% on the basis of the following equation:

$$2\beta\text{-}FeOOH \longrightarrow Fe_2O_3 + H_2O \quad ...(3)$$

The formation of Fe_2O_3 was confirmed by DTA, DTG and TGA graphs on a fresh sample of B_1, i.e. $Fe(OH)_3$ which was preheated at 573 K for 3 hr.

3.2 Mössbauer Spectroscopy

Mössbauer effect measurements were carried out on sample B_1 identified as $Fe(OH)_3$ at 77 K and 298 K and also *in situ* at different temperatures from 298 K to 573 K. The Mössbauer spectra of sample B_1 at different temperatures are two-line spectra and are all nearly identical. A representative spectrum is given in Fig. 2, and the calculated parameters are shown in Table 1. Spectra of sample B_1 at both these temperatures are of paramagnetic nature. The isomer shift IS (Fe^{3+}) at 298 K is $0{\cdot}35 \pm 0{\cdot}03$ mm/sec with respect to natural iron and a quadrupole splitting ΔE_Q of $0{\cdot}62 \pm 0{\cdot}06$ mm/sec. The observed isomer shift value is characteristic of high-spin ferric ion and is in agreement with the earlier reported value of 0·42 mm/sec by Karpachevskii *et al.*[6] in $Fe(OH)_3$ at room temperature. The same authors also observed a quadrupole splitting of 0·72 mm/sec in the same system which is in agreement with our observed value of 0·62 mm/sec.

Mössbauer parameters calculated from the spectra recorded at different temperatures from 298 to 573 K on a fresh sample of B_1 are shown in Table 1. An

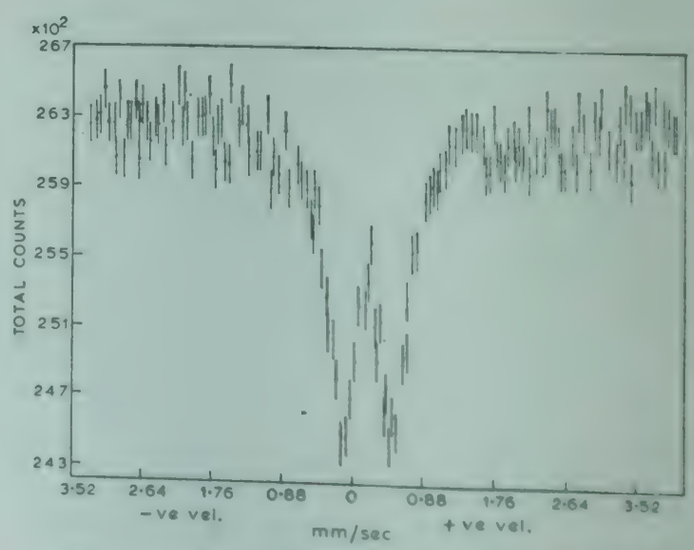

Fig. 2—Mössbauer spectrum of sample B_1 at 298 K

Table 1—Calculated Values of Different Mössbauer Parameters at Different Temperatures

Sample	Sample temp. K	Heat treatment	IS w r t natural iron (mm/sec±0·03 mm/sec.)	QS ΔE_Q (mm/sec ± 0·06 mm/sec)	Effective hyperfine field (H_n) kOe	Linewidth (Γ) (mm/sec ± 0·04 mm/sec)
B_1	77	Dried below 370K	0·41	0·63	—	—
,,	298	-do-	0·35	0·62	—	—
,,	*In situ*					
,,	298	-do-	0·39	0·62	—	—
,,	373	-do-	0·26	0·53	—	—
,,	423	-do-	0·19	0·49	—	—
,,	473	-do-	0·17	0·71	—	—
,,	523	-do-	0·10	0·57	—	—
,,	573	-do-	0·01	0·49	—	—
B_2	77	Prepared by heating B_1 at 573 K, 3 hr	0·61	—0·01	441	—
,,	193	-do-	Relaxation effect			
,,	298	-do-	0·41	0·81	—	—
,,	513	-do-	0·32	0·73	—	—
B_{3-1}(a)	298	Prepared by heating B_2 at 823 K, 4 hr	0·40	—0·12	494	0·55
B_{3-1}(b)	298	-do- 60 hr	0·23	—0·18	499	0·41
B_{3-2}	298	-do- 3 hr	0·45	—0·03	493	0·55
,,	558	-do- 3 hr	0·21	—0·03	419±10	—
B_{3-3}	298	Prepared by heating B_2 at 973 K, 50 hr	0·15	—0·18	513	0·45

interesting observation is the sharp change of quadrupole splitting value from 0·49 ± 0·06 mm/sec at 423 K to 0·71±0·06 mm/sec at 473 K. This confirms the earlier thermoanalytical results of $Fe(OH)_3$ transformation to $Fe_2O(OH)_4$ shown by DTA, DTG graphs in the temperature range 423-473 K. The temperature dependence of isomer shift is $-1{\cdot}38 \times 10^{-3}$ mm/sec/K or $(1/E)(\delta E/\delta T) = -4{\cdot}6 \times 10^{-15}$/K which is about twice the high temperature limiting value of $-2{\cdot}44 \times 10^{-15}$/K and could not be ascribed as only due to the second order Doppler shift arising from lattice vibrations. The continuous decrease in isomer shift value (Table 1) with increase of temperature of the absorber may be due to the slow water loss from the sample. This conclusion is also supported by the DTA and DTG graphs in the temperature interval 295-550 K. However, in the temperature interval 423-475 K where transformation of $Fe(OH)_3$ to $Fe_2O(OH)_4$ takes place, there is no marked change in the isomer shift.

Mössbauer studies of sample B_2 (β-FeOOH) were carried out at 77, 193, 298 and 513 K. The observed spectra at 77, 193 and 298 K are shown in Fig. 3 (a, b, c). The calculated parameters are tabulated in Table 1. At 77 K [Fig. 3 (a)], a six-line spectrum is observed, each line having linewidth = 0·6 mm/sec (Full linewidth of natural iron foil of 0·001 in. thick is 0·34 mm/sec). The calculated parameters are IS (Fe^{3+})=0·61±0·03 mm/sec, $\Delta E_Q = -0{\cdot}01 \pm 0{\cdot}06$ mm/sec and effective magnetic field H_n (Fe^{3+}) = 441±10 kOe. These values are in agreement with the earlier reported value of IS (Fe^{3+})=0·70 mm/sec, ΔE_Q=0·2 mm/sec and H_n (Fe^{3+})=480 kOe calculated from the graph reported by Dezsi *et al.*[7] Also our H_n (Fe^{3+}) value is in good agreement with the values of 445 kOe of Moreira *et al.*[8] and 466 kOe of Rossister *et al.*[9] in the same compound. However, it may be stated that β-FeOOH obtained by us did not give a sharp X-ray diffraction pattern, while that synthesized by Dezsi *et al.*[7] and others[8,9] was of crystalline state. At 193 K [Fig. 3 (b)], the Mössbauer spectrum of B_2 (β-FeOOH) showed electronic relaxation effect with broadening of the central lines at the expense of other lines. Similar effects in β-FeOOH have also been observed by Dezsi *et al.*[7] in the temperature range 120-295 K. It is well known that

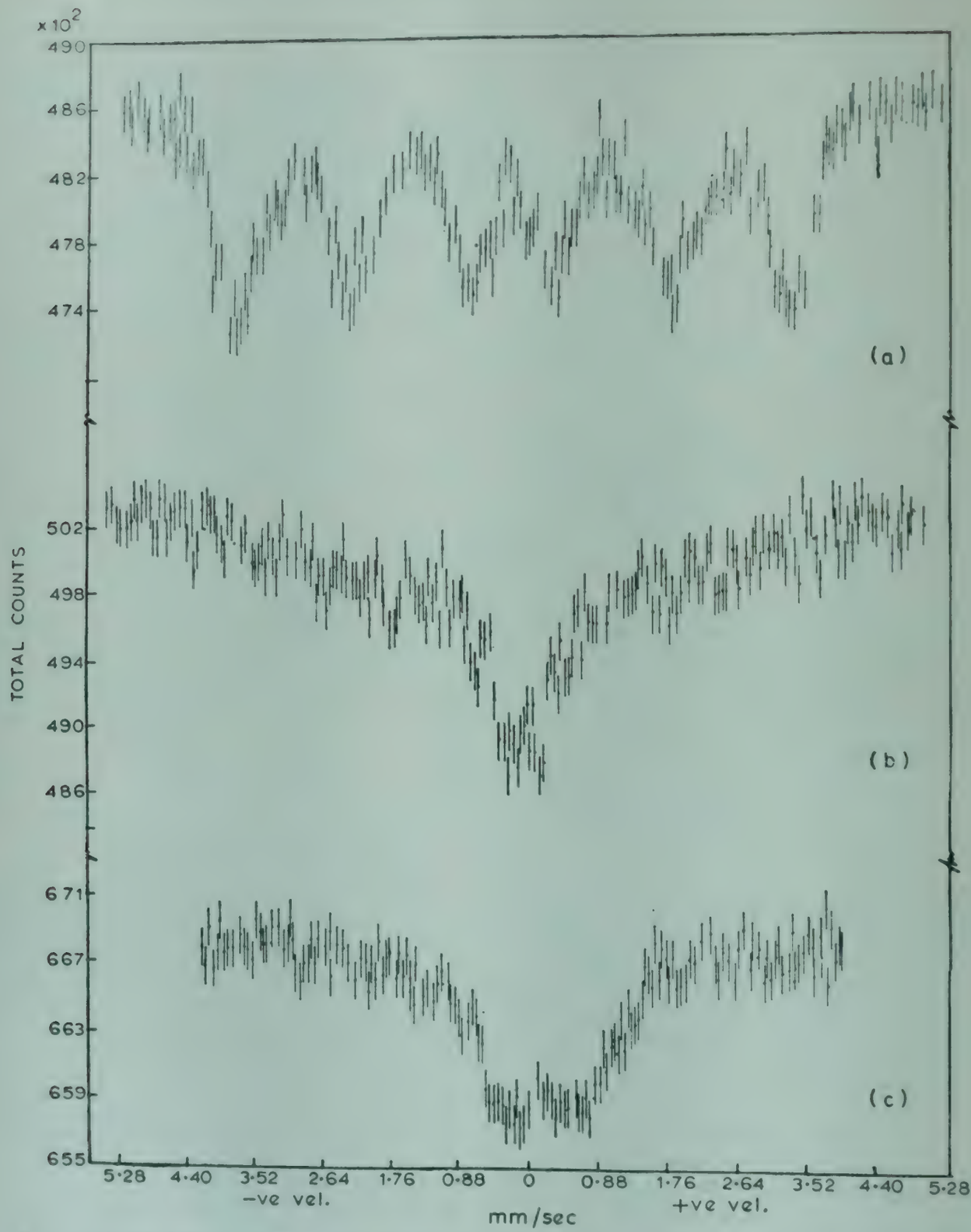

Fig. 3—Mössbauer spectra of sample B_2 (prepared by heating sample B_1 at 553 K for 3 hr) [(a) at 77 K, (b) at 193 K, (c) at 298 K]

such effects are observed when relaxation frequency of the spin of *d*-shell electrons is of the same order of magnitude as the Larmour frequency of the magnetic moment of 14·4 keV level of the iron nucleus in the internal magnetic field. At 298 K [Fig. 3(c)], paramagnetic spectrum of sample B_2(β-FeOOH) was obtained having Mössbauer parameters IS (Fe^{3+}) = 0·41 ± 0·03 mm/sec and ΔE_Q = 0·81 ± 0·06 mm/sec. The earlier reported values for β-FeOOH at 298 K are 0·36 mm/sec and 0·62 mm/sec of Van der Giessen[10] and 0·38 mm/sec and 0·69 mm/sec of Terrell *et al.*[11] respectively. The Neel temperature reported by Rukosev *et al.*[12] for β-FeOOH is 283 K and that by Dezsi *et al.*[7] is 295 K. Detailed measurements of Neel temperature, however, could not be carried out due to non-availability of

the variable temperature cryostat. However, the fact that at 298 K, the observed Mössbauer spectrum was of paramagnetic state and at 193 K of electronic relaxation nature, suggests that the transition from anti-ferromagnetic to paramagnetic state takes place between these two temperatures.

The transformation of B_2 (β-FeOOH) to B_2 (Fe_2O_3) was studied further. Different samples of β-FeOOH were given different heat treatments as shown in Table 1. Samples B_{3-1} and B_{3-2}, heat treated at 820±5 K for 3-4 hr and then for 60 hr (Fig. 4, a and b) respectively show a Zeeman shift six-line pattern. Each line of the six-finger pattern of the sample heated for 3-4 hr has the fullwidth of 0·55 ±0·04 mm/sec, which is about one and a half times greater than that obtained for α-Fe_2O_3, i.e. 0·36 mm/sec.[13] Therefore, it can be concluded that sample B_{3-1} (a) and B_{3-2} heat treated at 820 K for 3-4 hr were a mixture of α- and γ-Fe_2O_3. The observed hyperfine magnetic interaction value of 494±5 kOe of these samples is smaller than that observed for α-Fe_2O_3, viz. 515±5 kOe (Ref. 14). The observed isomer shift value of 0·40±0·03 mm/sec for sample B_{3-1} is also an indication of the fact that sample B_2 heat treated for 3-4 hr at about 820 K contains some γ-Fe_2O_3, because the reported values of IS (Fe^{3+}) with respect to natural iron at A and B sites are respectively 0·27±0·04 mm/sec and 0·41±0·04 mm/sec.[15] Samples B_{3-1} and B_{3-2}, when subjected to long heat-treatment, viz. at 820 K for 60 hr, were converted to α-Fe_2O_3 as is evident from the study of the Mössbauer data taken at 298 K after the heat treatment. The observed parameters, viz. IS (Fe^{3+}) =0·23±0·03 mm/sec, $\Delta E_Q = -0{\cdot}18 \pm 0{\cdot}06$ mm/sec and H_n (Fe^{3+})=499±8 kOe, are consistent with the corresponding reported value of IS (Fe^{3+})=0·23 ±0·03 mm/sec, $\Delta E_Q = -0{\cdot}17$ mm/sec and H_n (Fe^{3+}) =510±5 kOe[13] and with IS (Fe^{3+})=0·21±0·03 mm/sec, H_n (Fe^{3+})=515±5 kOe (Ref. 14). The presence of α-Fe_2O_3 in greater degree in a long heat-treated sample B_2 [indexed as $B_{3-1(b)}$ and B_{3-3}] is also reflected in the decrease in linewidth from 0·55 ±0·04 mm/sec to 0·41±0·04 mm/sec which is closer to the measured linewidth 0·36 mm/sec of α-Fe_2O_3 (Ref. 13). Dezsi *et al.*[7] have confirmed that the conversion of β-FeOOH to α-Fe_2O_3 is completed only when β-FeOOH is heated at 675 K for 12 hr. The study of X-ray diffraction patterns of both 4- and 60-hr heat-treated samples of B_2 also confirms the presence of α- and γ-phases of Fe_2O_3 in the samples B_3. This fact is also borne out from the Mössbauer spectra of both these heat-treated samples. The samples heat treated for 4 hr [Fig. 4 (a)] show low resonance peaks as the iron Mössbauer nuclei in

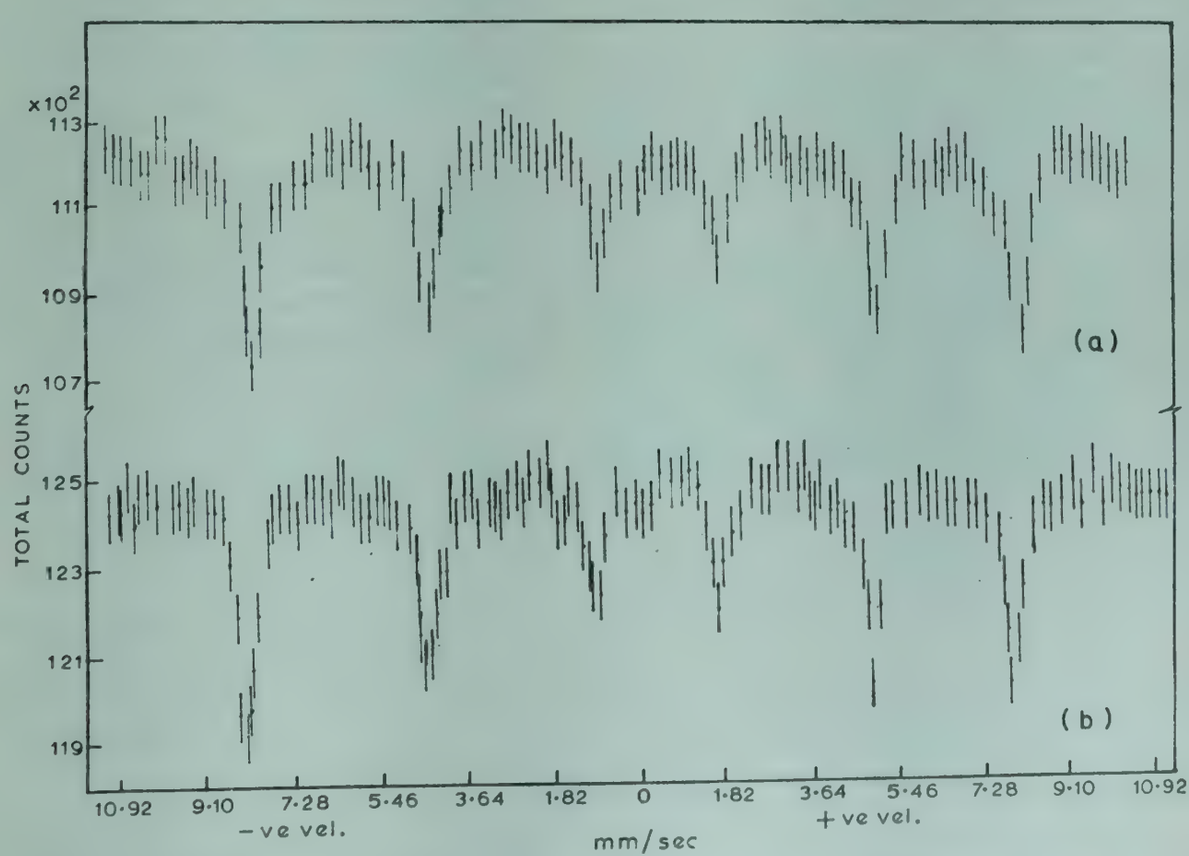

Fig 4—Mössbauer spectra of sample B_{3-1} at 298 K (prepared by heating sample B_2 at 823 K) [(a) for 4 hr and (b) for 60 hr)]

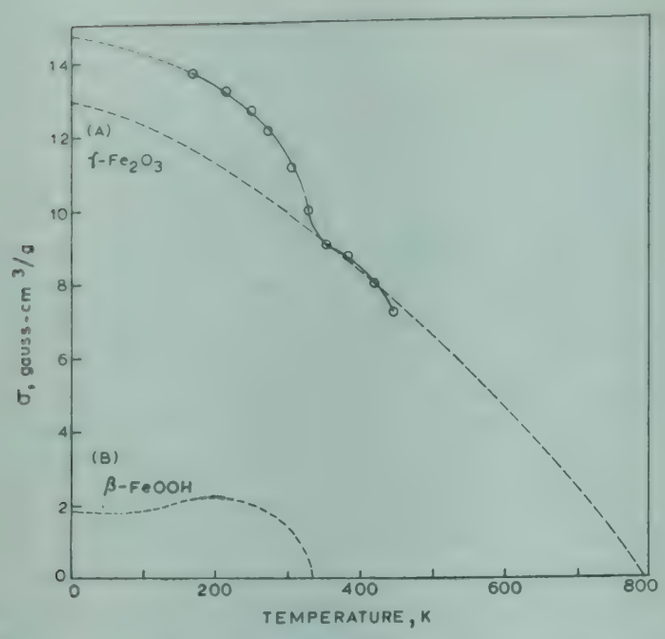

Fig. 5—Graph of saturation magnetization σ versus temperature for the sample B_2

γ-Fe_2O_3 get distributed over A and B sites in the lattice. Compared to this, the samples heat treated for 60 hr, show very narrow, well developed 6-line pattern [Fig. 4(b)] similar to that obtained for α-Fe_2O_3. It is significant to note from the thermo-analytical data obtained during the temperature interval 820-1250 K that there can be no appreciable change in the structure of α-Fe_2O_3.

3.3 Saturation Magnetization

Saturation magnetization measurements of sample B_2 were carried out between 77 and 450 K. Observed values of saturation magnetization (denoted by circles) versus temperature are plotted in Fig. 5. It is clear from the graph that there is a break at 370 K. It can be concluded that sample B_2 is composed of two different magnetic materials, β-FeOOH and a small quantity of γ-Fe_2O_3. Assuming the observed saturation magnetization values are due to these two materials, the values due to β-FeOOH material (graph B) were obtained after subtracting the values due to γ-Fe_2O_3 (values due to γ-Fe_2O_3 are plotted as broken line graph A as calculated from the saturation magnetization at T_0 K (Ref. 16) data taking σ for pure γ-Fe_2O_3 as 78 gauss-cm^3/g). The γ-Fe_2O_3 present in sample B_2 (β-FeOOH) was of amorphous nature and less than 18% by weight, hence could not be detected by Mössbauer spectroscopy.

Acknowledgement

Thanks are due to Dr S Badrinarayan and Dr S D Sathaye for the valuable cooperation during the course of this work.

References

1. *Solid state chemistry*, edited by C N R Rao (Marcel Dekker, New York), 1974.
2. Sathaye S D & Sinha A P B, *Thin Solid Films*, **44** (1977), 57.
3. Vogel A I, *Quantitative inorganic analysis* (The English Language Book Society, London), 1968.
4. Paulik F, Paulik J & Erdey L, *Talanta*, **13** (1966), 1405.
5. Rathenau G W & Snoek J C, *Philips Res. Rep.*, **1** (1946), 239.
6. Karpachevskii I O, Babanin V F, Gendler T S, Opalenko A A & Kuzmin R H, *Mössbauer effect data index*, edited by J G Stevens & V E Stevens (IFI/Plenum, New York), 1973.
7. Dezsi I, Keszthelyi L, Kulgawozuk D S, Molnar B & Eissa N A, *Phys. Status Solidi*, 22 (1967), 617.
8. Moreira J E, Kundsen J M, DeLima C G & Dufresne A, *Anal. Chim. Acta*, 63 (1973), 295.
9. Rossister M J & Hodgson A E M, *J. inorg. nucl. Chem.*, 27 (1965), 63.
10. Van der Giessen A A, *Philips Res. Rep. Suppl.*, 12 (1968), 39.
11. Terell J H & Spijkerman J J, *Appl. Phys. Lett.*, 13 (1968), 11.
12. Rukosev M N, Yamzin II, Chikachev V A & Lyubimstev A A, *Soviet Phys. Crystallogr.*, 16 (1971), 452.
13. Gupta M P & Sinha A P B, unpublished work.
14. Kistner O C & Sunyar A W, *Phys. Rev. Lett.*, 4 (1960), 412,
15. Armstrong R J, Morish A H & Sawatzky G V, *Physics Lett.*, **31** (1966), 414.
16. Goto Y, *Japan J. appl. Phys.*, 3 (1964), 742.

Indian Journal of Pure & Applied Physics
Vol. 18, July 1980, pp. 479-482

Kinetics of Growth & Dissolution of Potassium Dihydrogen Phosphate Crystals in Aqueous Solutions

M S Joshi & A V Antony

Physics Department, Sardar Patel University, Vallabh Vidyanagar 388 120

Received 3 *May* 1979

Growth and dissolution rates of potassium dihydrogen phosphate (KDP) crystals in aqueous solutions measured along [001] and [100] directions are reported. Effects of temperature and *p*H on growth rates along *z*- and *x*-axes are discussed. It is concluded that these growth rates are enhanced with increase in crystallization temperature and also with decrease in *p*H. It is shown that the habit of crystals is independent of temperature, but it changes with *p*H values; more acidic solutions yield more elongated crystals. Dissolution kinetics along *z*- and *x*-axes, investigated as a function of undersaturation and temperature of the solution, are also reported.

1. Introduction

To understand the mechanism of interfacial reactions and to obtain relationship between growth and dissolution reactions, several investigators[1-6] have carried out studies on the kinetics of growth and dissolution of crystals. Potassium dihydrogen phosphate (KDP) crystals, elongated in the [001] direction could be had from their pure supersaturated aqueous solutions. Substantial literature[5-10] is available about various aspects of growth of KDP crystals as well as for ammonium dihydrogen phosphate (ADP) crystals.

In the present paper, further experimental information is given in regard to growth and dissolution of KDP crystals in aqueous solutions. The growth and dissolution rates have been computed from the change in the dimensions of the crystal along [001] and [100] directions. Effects of temperature and *p*H on growth of KDP crystals were also studied. The present investigation also deals with observations on dissolution rates in different undersaturated solutions and also in pure water, at different temperatures.

2. Experimental Details

Apparatus, materials used and the methods for preparing seed crystals for the present work are the same as those reported by us earlier.[6] Both in the growth and dissolution studies, the crystals concerned were kept under a travelling microscope, and their dimensions along [001] and [100] directions were measured at different stages. Aqueous solutions of KDP were prepared in 250 ml glass vessels and allowed to equilibrate, at the desired temperature of the experiment, on the platform of the constant-temperature bath. The solubility of KDP at different temperatures is given in Table 1.

For measurements on growth rates, the supersaturation of the solution is expressed as the concentration driving force $\Delta C = C - C_0$, where C_0 is the saturation concentration and C is the concentration at any instant in grams of the solute in 100 ml of the solvent. To measure dissolution rates, the undersaturation of KDP solution is expressed as a relative term, $\rho = (C_0 - C)/C_0$. When the aqueous solution attains temperature equilibrium, the seed crystal (in the case of growth rate studies) or the crystal (in the case of dissolution studies), of known dimensions, was suspended symmetrically in the solution. At the end of fixed intervals of time, its dimensions along [001] and [100] directions (along *z*-and *x*-axes respectively) were measured. From these measurements the growth rate or the dissolution rate, as the case may be, was determined along these two directions. In either case, about 16 trials were taken and the average is used to mark each of the points in the graphs (Figs. 1-5) drawn to depict the results.

Table 1—Solubility of KDP at Different Temperatures

Temperature, °C	20	25	30	35	40	45	50
Solubility, g/100 ml water	23·5	25·2	27·8	30·5	33·5	36·8	41·0

Table 2—Solubility of KDP at Different pH Values of Solution

pH of solution	4·10	5·20	5·65	5·90	6·10
Solubility, g/100 ml solvent	27·8	31·6	37·3	43·7	49·5

2.1 Growth Kinetics

To study the effect of temperature on growth, observations were taken for 5 different temperatures ranging from 25 to 45°C and, for each temperature, two supersaturations, viz. $\Delta C = 2$ g and 4 g were used. Such observations were taken both for unagitated and agitated systems. In the latter, the solution was stirred by a paddle-shaped glass stirrer, driven by a geared ac motor at a speed of 250 rpm.

Addition of KOH to aqueous solutions of KDP leads to an increase in the solubility of the salt and also an increase in the pH of the solution. Table 2 shows the solubility of KDP in water at different pH values of the solution. To investigate the effect of pH on the growth rate, observations were taken for 5 different supersaturations of the solution at three different values of the pH.

2.2 Dissolution Kinetics

To study the dissolution kinetics of KDP along [001] and [100] directions, dissolution rates were computed at different values of undersaturations, at three different temperatures, 20°C, 30°C and 40°C.

Finally, to study dissolution rates of KDP crystals in water along x- and z-axes, eight observations were taken for each direction, at temperatures between 20 and 55°C.

3. Results and Discussion

3.1 Growth Kinetics

Effect of temperature—Fig. 1 presents the results of growth rates R_z and R_x of KDP crystals along z- and x-axes respectively, at different temperatures between 25 and 45°C, for the unagitated system. On the other hand, Fig. 2 shows graphs of growth rate versus temperature for the agitated system. These graphs show increase in growth rate, along z- (R_z) and x-axes (R_x), with increase in temperature. This may be attributed to increase in growth rates of [011] and [100] planes respectively. Further, the slope of the curve increases with increase in the supersaturation. Joshi *et al.*[5] have reported that the habit of KDP crystals (ratio of growth rate along z-axis to that along x-axis) changes with supersaturation and fluid shear. In the present study, however, it is found that habit is not altered with temperature. It may be noted that the graphs for unagitated and agitated systems are almost identical, except that growth rates are comparatively greater for the agitated systems. This suggests that increase in growth rate at higher temperatures is not primarily due to diffusion of the ions.

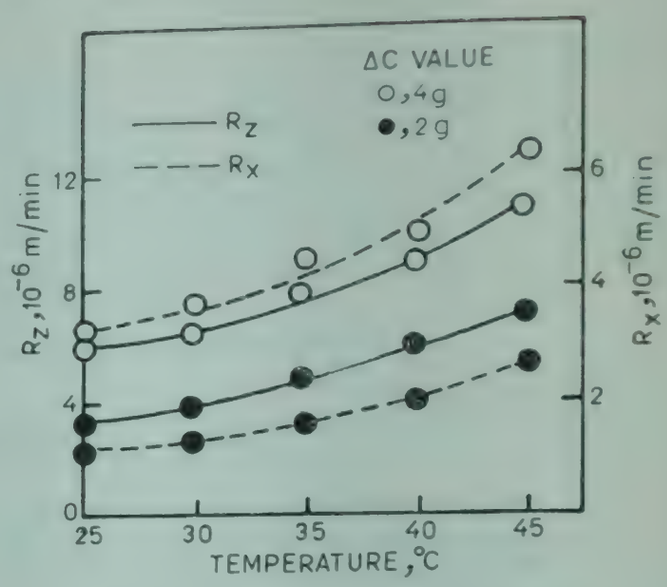

Fig. 1—Plots of R_z and R_x versus temperature (unagitated system)

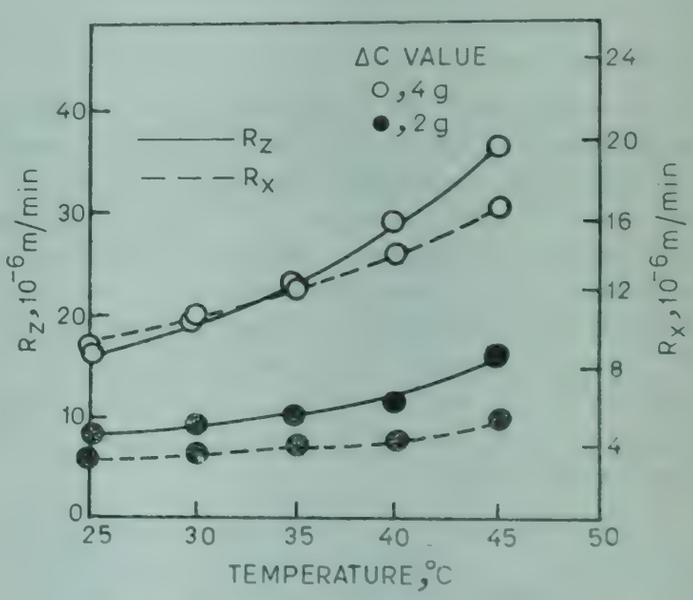

Fig. 2—Plots of R_z and R_x versus temperature (agitated system)

Studies on nucleation rates in supersaturated aqueous solutions of KDP show that the interfacial energy for growth of KDP crystals decreases with increase in temperature.[11] The present study also shows that the rate of growth of the faces of KDP crystals increases with increase in temperature. Consequently, increase in growth rate, at higher

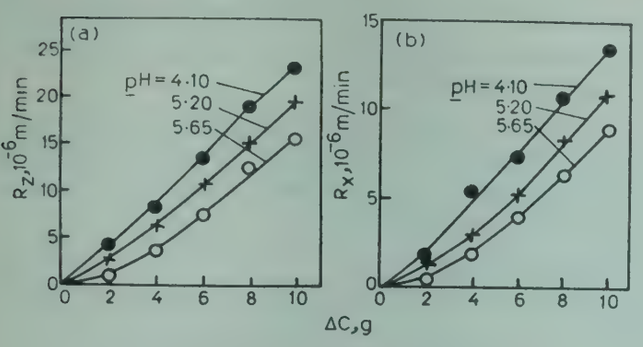

Fig. 3—Plots of R_z and R_x versus Δ C

temperatures, may be attributed to decrease in interfacial energy with temperature.

Effect of pH—According to Mullin *et al.*[7] increase in pH results in the increase in growth rate of ADP crystals along both the principal axes. On the other hand, By teva[10] hasreported that more acidic solutions (lower pH) yield ADP crystals which are more elongated along the z-axis, which means increase in growth rate along z-axis for solutions of lower pH values. Results of Mullin *et al.*[7] and Byteva[10] are contradictory to each other. Our results on KDP crystals (present investigation) are similar to those of Byteva for ADP crystals. This is shown in plots of growth rates along z-axis [Fig. 3(a)] and x-axis [Fig. 3(b)] against supersaturation, for three different pH values.

To investigate the effect of pH on the habit (ratio of length L to breadth B), measurements of dimensions along z- and x-axes were made on a

Table 3 – Habit of KDP Crystals at Different pH Values

pH	4·10	5·20	5·65	5·90	6·10
L/B	2·00 – 2·40	1·85	1·75	1·70	1·60
R_z/R_x	2 00	1·94	1·88	—	—

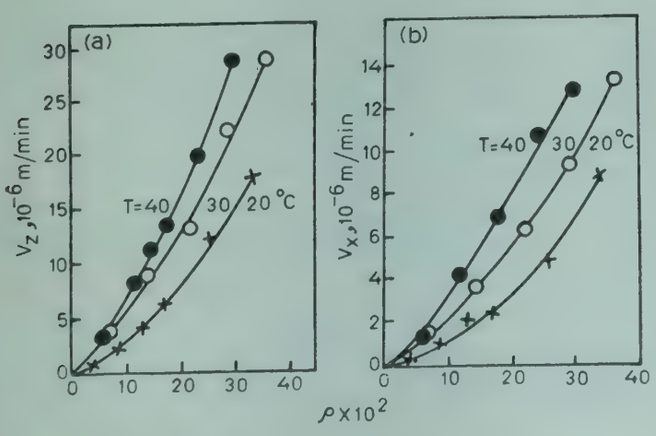

Fig. 4—Plots of V_z and V_x versus ρ

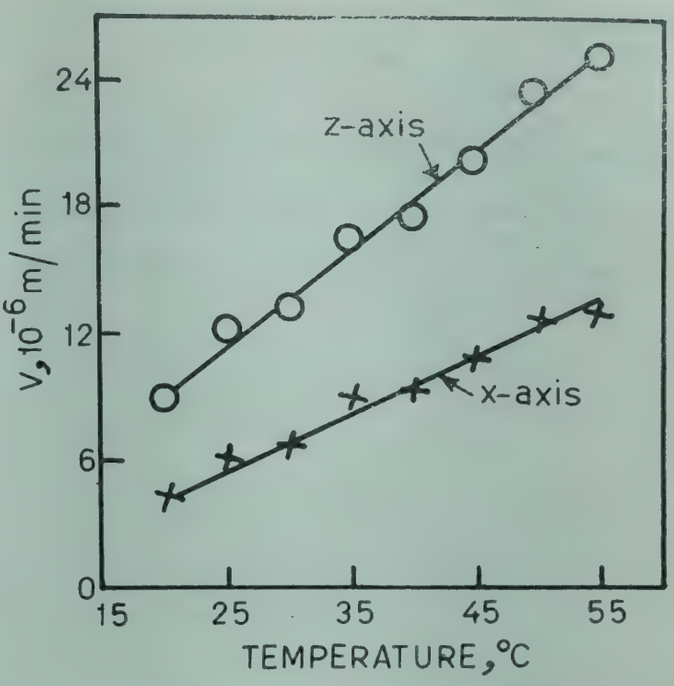

Fig. 5—A plot of dissolution rate versus temperature in pure water

number of crystals grown by slow evaporation of saturated solutions of KDP, at temperature 30°C, at different pH values. Table 3 shows our observations on habit (L/B and R_z/R_x) as a function of pH. These results indicate that crystals more elongated along z-axis result for lower pH values.

3.2 Dissolution Kinetics

Dissolution rates V_z and V_x along z- and x-axes respectively were measured at different undersaturations ρ at temperatures 20, 30 and 40°C. The results are graphically represented in Figs. 4(a) and 4(b). These curves show that dissolution rates, in both these directions, increase with increase in both undersaturation and temperature.

Dissolution rates of KDP crystals, along z- and x-axes, in pure water are also plotted against temperature and straight line graphs are obtained as shown in Fig. 5. Along both the directions, dissolution rates are linearly related to temperature. Consequently dissolution rates $V_{z,x}$ may be related by an equation of the form $V_{z,x} = A_{z,x}\,T$, where $A_{z,x}$ are dissolution rate constants, From these graphs, A_z is found to be $4{\cdot}6 \times 10^{-7}$ m min^{-1} K^{-1} and, A_x is found to be $2{\cdot}0 \times 10^{-7}$ m min^{-1} K^{-1} for the temperature range 20-55°C.

Acknowledgement

One of the authors (AVA) would like to express his sincere thanks to CSIR, New Delhi, for an award of a research fellowship.

References

1. Brice J C, *J. Cryst. Growth*, 1 (1967), 161.
2. Jones A L, Linge H G & Wilson I R, *J. Cryst. Growth*, 12 (1972), 201.
3. Jones A L, Linge H G & Wilson I R, *J. Cryst. Growth*, 26 (1974), 37.
4. Garside J, Mullin J W & Das S N, *Ind. Engng. Chem. Fundam.*, **13** (1974), 299.
5. Joshi M S & Baby K Paul, *J. Cryst. Growth*, **22** (1974), 321.
6. Joshi M S & Antony A V, *J. Phys.*, D **10** (1977), 2393.
7. Mullin J W, Amatavivadhana A & Chakraborty M, *J. appl. Chem.*, **20** (1970), 153.
8. Davey R J & Mullin J W, *Krist. Tech.*, **11** (1976), 625.
9. Byteva I M, in *Growth of crystals*, edited by A V Shubnikov and N N Sheftal (Consultants Bureau, New York), 3 (1962), 213.
10. Ref 9, 4 (1966), 16.
11. Joshi M S & Antony A V, *J. Cryst. Growth*, **46** (1979), 7.

Indian Journal of Pure & Applied Physics
Vol. 18, July 1980, pp. 483-488

Characterization of Deep Trapping Centres in *n*-Type Liquid Phase Epitaxial GaAs by Hall Effect

ASHOK K SAXENA*

Department of Electronics & Electrical Engineering, University of Sheffield, Mappin Street S1 3JD, Sheffield UK

Received 5 *July* 1979, *revised received* 21 *January* 1980

Hall and photo-Hall measurements on van-der Pauw samples of high quality *n*-type GaAs crystals, grown by liquid phase epitaxial technique, are performed in the temperature interval 300-80 K. The dependences of the Hall and photo-Hall mobilities on temperature are analysed to establish the acceptor-like nature of the trapping centres lying in the forbidden energy gap and their concentration is determined. The best crystal shows a Hall mobility of 6100 cm^2/V-sec and carrier concentration of $2{\cdot}0 \times 10^{14}$ cm^{-3} at 300 K.

1. Introduction

The electrical properties of several III-V semiconductors are being investigated because of their potential applications in electroluminscent devices such as light emitting diodes (LED), solar cells, DH-lasers and microwave devices. Deep levels in semiconductors, be they radiative or non-radiative centres, are usually responsible for degradation of performance of semiconductor devices. A knowledge of the nature and origin of these levels is, therefore, of great interest. These centres capture either electrons or holes and emit them back to the conduction or valence bands, respectively, after a characteristic time which is a function of crystal temperature. Observed degradation phenomenon in III-V semiconductor lasers have been attributed to dislocations, defects, radiative and non-radiative deep centres. In order to evaluate the merits of GaAs for various device applications, it is necessary to detect and characterize deep levels which might be present.

Frequently two types of energy levels are distinguished, (i) those which are responsible for the type of conductivity and which have shallow energy levels with hydrogen-like behaviour, and (ii) those which influence the lifetime of free carriers and have deep energy states with significant deviation from the Coulombic potential. The properties of GaAs are affected by the presence of deep levels.

Various techniques have been used in an effort to characterize deep traps in GaAs and other semiconductors. Measurement of the capacitance of Schottky barrier diode is a very powerful technique for characterizing deep energy levels[1,2] since it provides a sensitive measure of the charge in the traps. In this paper, we describe the measurement of the Hall and photo-Hall mobilities of *n*-type liquid phase epitaxy GaAs in the temperature interval 300-80 K. The results are analysed to determine the nature and concentration of the trapping centres lying in the forbidden enegy gap.

The experimental techniques are described in Sec. 2 and the procedure in Sec. 3. The results are presented and analysed in Sec. 4 and discussed in Sec. 5. The conclusions drawn from the present work are summarized in Sec. 6.

2. Experimental Techniques

2.1 Preparation of Hall Samples

The epitaxial layers of GaAs were grown in our laboratory by the liquid phase technique.[3] The crystals of $\sim 4 \times 4$ mm size and approximately 400 μm thick were used. A positive photoresist (AZ-135OH) and a negative glass mask were used to delineate a clover leaf pattern on the epitaxial layers. The unexposed photoresist was dissolved in microstrip solution and the sample baked at 100°C for 45 min. The substrate was protected with a thick layer of negative photoresist (way coat HR 100). The bare epitaxial layer was then etched off together with nearly 10 μm of the substrate using 1% bromine methanol solution. After removing the photoresist, ohmic contacts to the epitaxial layers were made using In. The contacts were alloyed in a conventional furnace in H_2 atmosphere for 1 min at 500°C. Before making any electrical measurements, the contacts were checked for ohmic characteristics.

*Present address : Department of Electronics & Communication Engineering, University of Roorkee, Roorkee

2.2 Experimental Arrangement for Hall Measurement

The sample was placed inside a double walled quartz tube dewar which had a vacuum of $\sim 10^{-4}$ torr in between the walls. The temperature of the sample was changed by pumping cooled N_2 gas into the dewar at the required rate. The temperature could be controlled within $\pm 1°C$ by controlling the gas flow during the measurements at a particular temperature. The sample holder was designed for measurements both at high temperatures ($300 < T < 750$ K) and at low temperatures ($80 < T < 300$ K). It consisted of a heater enclosed in between two OFHC (oxide free high conductivity) copper plates. Four metal posts insulated from the copper plates and from each other held the phosphor-bronze shoes making pressure contacts to the sample. Care was taken to avoid any temperature gradients across the samples. The low temperatures ($T < 300$ K) were measured with a copper-constantan thermocouple. Provision was also made to measure high temperatures ($T > 300$ K) with a chromel-alumel thermocouple. These were calibrated at 100, 0 and $-196°C$ (liquid nitrogen temperature) and were placed as close to the sample as possible. A dummy piece of GaAs having the same dimensions as the crystal to be studied, was placed as close to it as possible. The thermocouples were fixed on the top surface of the dummy piece with the help of a thermally conducting paste.

The control unit was a constant current generator for $I = 1$, 10, 100 μA, 1 and 10 mA. All the voltages and currents were accurately measured on a digital electrometer (input impedance $> 10^{15}\ \Omega$). The control unit had the advantage of electrically rotating the sample through 360° in steps of 90°. As will be discussed later, the crystals were photosensitive, so the Hall measurements were carried out in the dark although provision was made for photo-Hall measurements using a source of white light.

3. Experimental Procedure

Hall and photo-Hall measurements on van-der Pauw samples were made in the temperature interval 300-80 K and in a magnetic field strength (B) of 5 kgauss. The sample resistivity (ρ) aud the Hall mobility (μ_h) are given by the equations[4]

$$\rho = \frac{\pi t}{2 \ln 2} (R_{AB,CD} + R_{BC,AD}) f [(R_{AB,CD})/(R_{BC,AD})] \quad \ldots(1)$$

$$\mu_h = \frac{t \cdot \Delta R_{AC,BD}}{B \cdot \rho} \quad \ldots(2)$$

where t is the thickness of the epitaxial layer.

The Hall coefficient (R_H) was then calculated from the relation

$$R_H = r (\rho \cdot \mu_h) = \frac{r}{(n_h \cdot q)} \quad \ldots(3)$$

where r is the Hall scattering factor and q, the electronic charge. The value of the factor r was considered to be unity. $R_{AB,CD}$ is the average resistance obtained by passing a current in both the directions through the contacts A and B and measuring the voltage across C and D. $R_{BC,AD}$ is similarly defined. $\Delta R_{AC,BD}$ is the average change in the resistance $R_{AC,BD}$ due to the application of the magnetic field B in both the directions across the epitaxial layer. The value of the function f in Eq. (1) depends on the ratio $R_{AB,CD}/R_{BC,AD}$ and has been obtained from Ref. 4. The contacts A, B, C and D which are 90° apart follow each other in order along the periphery of the sample.

Considering the finite size of the contacts relative to the sample, the corrections[4] have been made to the measured values of ρ and μ_h. In all the samples, the size of the contacts was kept so small that the correction for ρ was negligible and that for μ_h was less than 5%.

The Hall measurements were made with a small current passing through the epitaxial layers to avoid the heating of the crystals. With every sample so measured, a second set of measurements was also made by changing the direction of the currents through the contacts by 90° to investigate if there were any inhomogeneties in the layers. The magnetic field was found accurate to within $5 \pm 0{\cdot}001$ kgauss.

4. Results and Analysis

The measured temperature variation of the Hall and photo-Hall mobilities for two ctystals is shown in Fig. 1 and the computed values of n_h and μ are given in Table 1. In all the LPE-GaAs crystals studied, the photo-Hall mobility was found to be larger than the Hall mobility at the same low temperature ($200 > T > 80$ K). In analysing these results, the following assumptions have been made.

1. Each scattering process is described by a relaxation time $\tau(x)$ which depends upon the electron energy x in kT.
2. The various scattering mechanisms are independent of each other.
3. The electrons are scattered in a parabolic band. This allows the use of simpler formulations for the various scattering processes.

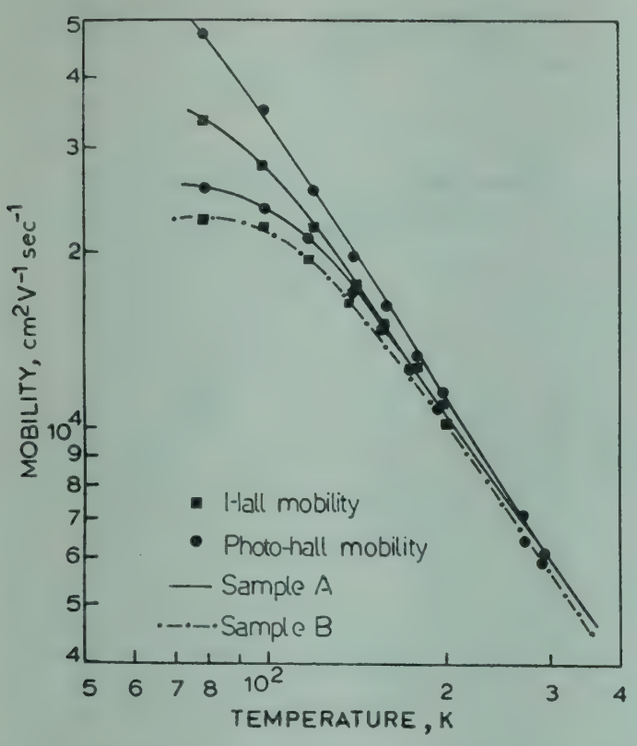

Fig. 1—Temperature dependence of the Hall and photo-Hall mobilities for n-type LPE GaAs

Table 1—Hall Carrier Concentrations (n_h) and Mobilities (μ) of Hall and Photo-Hall carriers

Sample No.	n_h, cm^{-3} 300 K	n_h, cm^{-3} 80 K	μ_h, cm^2/V-sec at 300 K	μ_h, cm^2/V-sec at 80 K	μ(photo-Hall) in cm^2/V-sec at 80 K
A	$2{\cdot}0\times10^{14}$	$1{\cdot}8\times10^{14}$	6100	35,000	49,000
B	$1{\cdot}3\times10^{15}$	$1{\cdot}1\times10^{15}$	5900	22,000	26,000

With the above simplifying assumptions, an average relaxation time $<\tau>$ is calculated from the equation[5]:

$$<\tau> = \frac{4}{3\sqrt{\pi}} \int_0^\infty \tau(x)\, x^{3/2}\, e^{-x}\, dx \qquad ...(4)$$

The electron mobility μ is then calculated from the equation.

$$\mu = \frac{q <\tau>}{m_e^*} \qquad ...(5)$$

where m_e^* is the electron effective mass in the Γ_{1c} minimum of GaAs. The correlation between the various scattering processes is ignored and an overall mobility has been calculated by the equation:

$$\frac{1}{\mu} = \Sigma_i \frac{1}{\mu_i} \qquad ...(6)$$

where μ_i is the mobility due to the individual scattering process. The following scattering mechanisms have been considered.

4.1 Optical Polar Scattering

In optical collisions, the energy change of the electrons can be large compared to their initial energy, and a universal relaxation time cannot be defined except at low and high temperatures. Fortini *et al.*[6] have used an iterative method to solve the Boltzmann's equation to determine the mobility of the electrons which is given by the expression:

$$\mu_{po} = \frac{16\,\hbar\,\epsilon_s\,(2\pi kT)^{1/2}\,(e^{\xi l}-1)}{3\,q\,\omega_l\,(m_e^*)^{3/2}\left(\frac{1}{\epsilon_\infty}-\frac{1}{\epsilon_0}\right)} \int_0^\infty \gamma(\xi, \xi l)\, d\xi \qquad ...(7)$$

where $\xi l = (T_{L0}/T)$, T_{L0} being the optical phonon temperature, ϵ_0, ϵ_∞, ϵ_s and ω_l are the low and high frequency dielectric constants of the semiconductor, vacuum and frequency of the longitudinal optical phonons, respectively. Putting the values of different constants in Eq. (7) from Table 2, we get

$$\mu_{po} = 227{\cdot}6\,(T)^{1/2}\,(e^{\xi l}-1)\,G(\xi l)\ \text{cm}^2/\text{V-sec} \qquad ...(8)$$

The function $G(\xi l)$ has been given by Fortini[6] *et al.*[6]

4.2 Piezoelectric Scattering

The relaxation time for piezoelectric scattering as determined by Zook[10] is given by the expression

$$\frac{1}{\tau_{PE}} = 1{\cdot}05\times10^7\times\hbar^2_{14}\left(\frac{4}{C_t}+\frac{3}{C_l}\right) \times\left(\frac{m_e^*}{m_0}\right) T^{1/2}\, x^{-1/2} \qquad ..(9)$$

where h_{14} ($= e_{14}/\epsilon_s\,\epsilon_0$) is the piezoelectric constant. C_t, C_l are the transverse and longitudinal elastic constants, respectively, and are given by the expressions:

$$C_t = \frac{1}{5}(C_{11}+3\,C_{44}-C_{12}),$$

$$C_l = \frac{1}{5}(3\,C_{11}+2\,C_{12}+4\,C_{44})$$

Table 2—Values of Various Constants for GaAs

Constant	Value	Ref.
m_e^*/m_0	0 072	6
ϵ_0/ϵ_s	12·91	6
$\epsilon_\infty/\epsilon_s$	10·91	7
T_{L0} (K)	419	7
C_{11} (dyne/cm^2)	$1{\cdot}37\times10^{12}$	7
e_{14} (c/cm^2)	$0{\cdot}16\times10^{-4}$	8
C_{11} (dyne/cm^2)	$1{\cdot}54\times10^{12}$	8
C_{12} (dyne/cm^2)	$1{\cdot}188\times10^{12}$	8
C_{44} (dyne/cm^2)	$0{\cdot}538\times10^{12}$	9

From Table 2 and Eqs. (4) and (5), we get

$$\mu_{PE} = 3{\cdot}16 \times 10^5 \times \sqrt{300/T}\ \text{cm}^2/\text{V-sec} \quad ..(10)$$

4.3 Deformation Potential Scattering

The relaxation time for deformation potential scattering based on the theory of Bardeen and Shockley[11] is given by Wolfe *et al.*[5] as

$$\frac{1}{\tau_{Dp}} = 4{\cdot}17 \times 10^{19} \left(\frac{E_1}{C_1}\right)^2 \left[\frac{m_e^*}{m_0}\right]^{3/2} T^{3/2}\, x^{1/2} \quad ...(11)$$

Using Table 2 and Eqs. (4) and (5), we get

$$\mu_{DP} = \frac{3{\cdot}22 \times 10^{10}}{E_1^2}\, T^{-3/2}\text{cm}^2/\text{V-sec} \quad ...(12)$$

where E_1 is the acoustic deformation potential in eV.

4.4 Ionized Impurity Scattering

An expression for the mobility due to ionized impurity scattering has been derived by Broooks[12] and is given by the equation:[13]

$$\mu_{II} = \frac{3{\cdot}28 \times 10^{15}\,(m_0/m_e^*)^{1/2}\ \epsilon_s^2\ T^{3/2}}{(2N_A+n)\,[l_n\,(b+1)-(b/b+1)]} \quad ...(13)$$

where $b = \dfrac{1{\cdot}29 \times 10^{14} \times (m_e^*/m_0)\,\epsilon_s\, T^2}{n^*}$

and $n^* = n + [(n + N_A)(N_D - N_A - n)/N_D]\ \text{cm}^{-3}$

N_A and N_D are the acceptor and donor concentrations, respectively, and n, the electron concentration.

The resultant electron mobility is then calculated from Eq. (6). In order to explain the temperature dependence of the Hall and photo-Hall mobilities, the acoustic deformation potential E_1 and N_A, N_D are kept as adjustable parameters. The comparison between the experimental and calculated results is shown in Fig. 2. The agreement is satisfactory except at low temperatures ($100 \lesssim T \lesssim 80$ K) where the calculated mobilities are slightly lower than experimental values. The results of the analysis are also tabulated in Table 3.

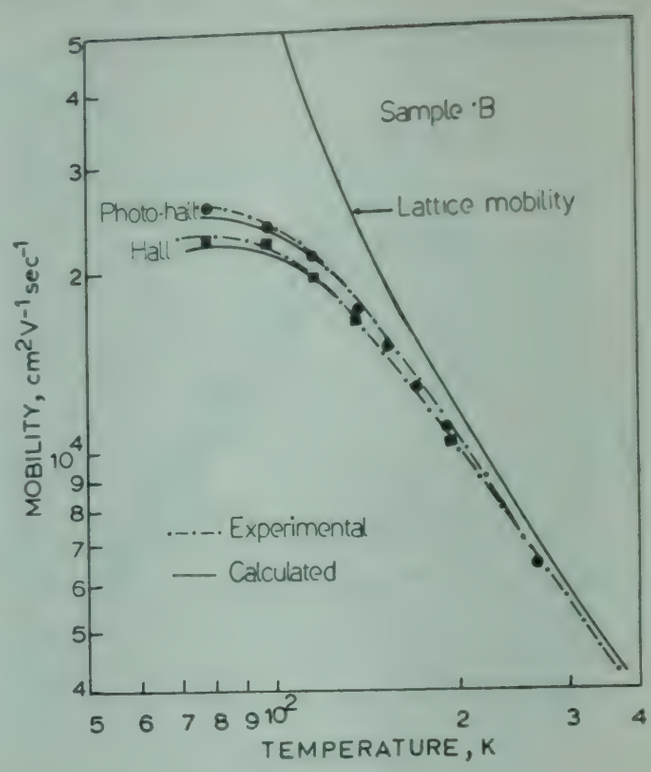

Fig. 2—Comparison between calculated and experimental temperature dependence of electron mobilities in n-type LPE GaAs. Also shown is the temperature dependence of lattice mobility

Table 3—Results of the Analysis of the Temperature Dependence of the Hall and Photo-Hall Mobilities

Sample No.	Nature of trap	E_1 (eV)	$(N_D^+ + N_A^-) = a$ in cm^{-3} (Hall)	$(N_D^+ + N_A^-) = b$ in cm^{-3} (photo-Hall)	Hole trap concentration $(a-b)$, in cm^{-3}
A	Hole	22·5	$3{\cdot}1\times10^{15}$	$1{\cdot}3\times10^{15}$	$1{\cdot}8\times10^{15}$
B	Hole	22·5	$8{\cdot}4\times10^{15}$	$7{\cdot}0\times10^{15}$	$1{\cdot}4\times10^{15}$

5. Discussion

In all LPE GaAs crystals studied, photo-Hall mobility was greater than the Hall mobility. On photo-excitation, the hole traps (negatively charged in the dark) become neutral after capturing holes from the valence band. Thus the total concentration of ionized impurity centres decreases on photo-excitation. This results in an increase in the electron mobility on photoexcitation at low temperatures where electron scattering by ionized impurities becomes dominant. At low temperatures, the photo-Hall mobility would have been lower than the Hall mobility if the crystals had only deep electron traps (neutral in the dark). On photoexcitation, these will get positively charged, thereby increasing the total concentration of charged impurity centres. The experimental results also show that the hole traps have non-shallow energy levels since at 80 K there is an appreciable increase in the electron mobility on photo-excitation. Since the energy of the shallow donors is of the order of 5 meV, these remain almost positively charged in the dark even at 80 K and do not complicate the present analysis.

In the analysis, we have made use of the assumption that the relaxation times and, therefore, the mobilities due to various scattering mechanisms are independent of each other. This considerably simplified the present analysis. We have checked the validity of this assumption in the following way. Rode[7] has obtained an exact solution of the

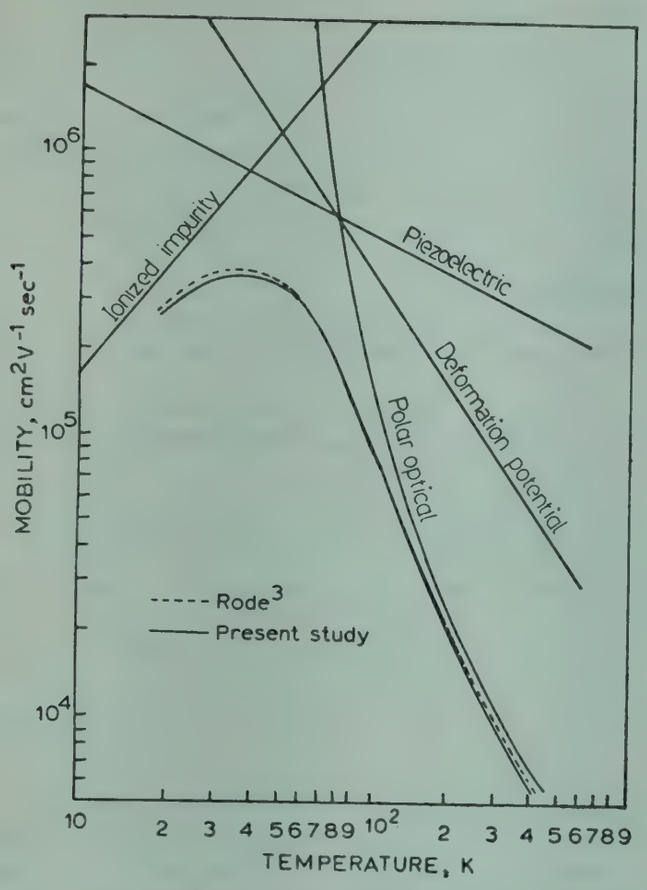

Fig. 3—Calculated temperature dependence of the electron mobility in n-type LPE GaAs due to various scattering mechanisms and a comparison with the results obtained from an exact solution of the Boltzmann's equation[7]

Boltzmann's equation using the values given in Table 2 and considering $E_1 = 8{\cdot}6$ eV for GaAs with $N_A = 2{\cdot}2 \times 10^{13}$ cm^{-3}, $N_D = 5{\cdot}2 \times 10^{13}$ cm^{-3}. The results of this analysis are plotted in Fig. 3. For comparison, the calculated temperature dependence of mobility according to Eqs. (4)-(12) using the same values as by Rode, is also plotted. The comparison shows the justification in using the approximation given by Eq. (6).

One might suspect that the low mobilities obtained for samples A and B might be due to the presence of space charge scattering centres. The electron mobility due to this scattering mechanism varies[14] as $(1/T)$ and the inclusion of this mechanism did not explain the results over the entire temperature interval 300-80 K. Since the ratio $R_{AB,CD}/R_{BC,CD}$ also remained independent of temperature, it is hard to believe that the crystals are inhomogeneous and the space charge centres are present. For these reasons, we were forced not to include the space charge scattering in our analysis and the acoustic deformation potential E_1 was varied to obtain a good fit between experimental and calculated results.

The value of the potential E_1 of 22·5 eV needed to explain the present results is rather high. The value of E_1 determined from elastic tensor and pressure rate coefficients of the band edge in GaAs, assuming the valence band to be stationary with strain is 8·6 eV.[7] The present values of E_1 cannot be taken as correct. It may, therefore, mean that another scattering mechanism having the same temperature dependence as the acoustic mode scattering is present in the samples studied.

Regarding the accuracy of the comparison, one may wonder why we generally plot theoretical drift mobility for comparison with the experimental Hall mobility. The Hall factor corrections are less than 20% except for temperatures near $(\hbar\omega_l)/2K$ and the theory is probably no more accurate than 20% in most cases because of some uncertainty in material parameters. Secondly the experimental data are taken for the magnetic field such that $\mu B \gg 1$, then the Hall factor is very nearly unity. This fact is reflected in Fig. 3, where the mobility determined by Rode is slightly higher than that calculated in the present study in the temperature interval $150 \lesssim T \lesssim 450$ K. The difference may result from the fact that Eq. (13) for the ionized impurity scattering is only valid if the electric potential resulting from the ionized impurities is small compared with the thermal energy of the electron. As the temperature goes down, this condition no longer holds true.

Measurement of Schottky barrier diode capacitance as a function of applied bias and time is a powerful technique for the detection and characterization of deep traps in semiconductors. From such measurements on samples A and B, it was confirmed that these had only one hole trap at an energy of 0·64 eV above the valence band maximum and that no deep electron traps were detected.[3] A comparison of the hole trap concentration as determined from the analysis of the temperature dependence of the Hall and photo-Hall mobilities and Schottky barrier technique is shown in Table 4. There is a reasonable agreement between the two results although the hole trap concentration determined from the present analysis is low. This might be due to the fact that light intensity may not be strong enough to neutralize all the hole traps.

If many electron and hole trapping centres are present in the crystal or it is desired to know their activation energy, it is imperative to use the monochromatic light source rather than the white light. It has been shown that the energy of the hole trapping centres in samples A and B is 0·64 eV above the valence band maximum and that these are related to complexes involving As vacancies in the lattice.[3]

Table 4—Comparison of Results obtained from the Hall/Photo-Hall Experiments and Schottky Barrier Capacitance Technique

Sample No.	Hall and Photo-Hall technique Hole trap concentration (cm^{-3})	Schottky barrier technique Hole Trap concentration (cm^{-3})	Schottky barrier technique Activation energy of the trap above the valence band edge in eV
A	$1{\cdot}8\times10^{15}$	$4{\cdot}0\times10^{15}$	0·64
B	$1{\cdot}4\times10^{15}$	$1{\cdot}1\times10^{15}$	0·64

6. Conclusions

It has been shown that a deep hole trap level lying in the forbidden energy gap is present in *n*-type LPE GaAs. The concentration of the centres in the level is determined. The results show that either the acoustic deformation potential in GaAs is probably 22·5 eV or another scattering mechanism having the same temperature dependence as the acoustic mode scattering is present in the crystals studied.

Acknowledgement

The authors are grateful to Dr A Majerfeld for his assistance and Mr A Walker for technical advice. Financial assistance from the Ministry of Education and Social Welfare, Government of India, which enabled the author to carry out the work at the University of Sheffield, is gratefully acknowledged.

References

1. Lang D V *J. appl. Phys.*, 45 (1974), 3023.
2. Hasegawa F & Majerfeld A, *Electron. Lett.*, 11 (1975), 286.
3. Saxena A K, *Electrical characterization of LPE grown GaAs layers*, M. Engng. Thesis, Sheffield University Sheffield, U K, 1975.
4. Van-der Pauw L J, *Philips Tech. Rev.*, 20 (1958/59), 220.
5. Wolfe C M, Stillman G E & Lindley W T, *J. appl. Phys.*, 41 (1970), 3088.
6. Fortini A, Diguet D & Lugand J J, *J. appl Phys.*, 41 (1970), 3121.
7. Rode D L, *Semiconductor and semimetals – Transport Phenomenon* (Academic Press, New York), 10 (1975), 1.
8. Rode D L *Phys. Rev.*, 2 (1970), 1012.
9. Madelung O, *Physics of III-V compounds* (John-Wiley, New York), 141.
10. Zook J D, *Phys, Rev.*, 136 (1964), A 869.
11. Bardeen F & Shockley W, *Phys. Rev.*, 77 (1950), 407.
12. Brooks H, *Adv. Electron. Electron Phys.*, 7 (1955), 158.
13. Wolfe C M, Stillman G E & Dimmock J O, *J. appl. Phys.*, 41 (1970), 504.
14. Weisberg L R, *J. appl. Phys.*, 33 (1962), 1817.

Indian Journal of Pure & Applied Physics
Vol. 18, July 1980, pp. 489-493

Superconductivity in Certain Metals

S C JAIN* & C M KACHHAVA
Department of Physics, University of Rajasthan, Jaipur

Received 3 *August* 1979

The existence of superconductivity in eleven metals is studied through three state parameters $\langle V_{ph} \rangle$, $\langle V_c \rangle$, and Z_0 by adopting plane wave states for the electron-phonon and Coulomb interactions and using Harrison's point-ion model for the electron-ion interaction. The metals under investigation are classified as superconducting and non-superconducting on the basis of the sign of the effective interaction strength parameter N_0V, which is obtained directly from the state parameters. The calculations of N_0V and the transition temperature T_c for the super-conductors lead to better values as compared to the existing theoretical results, thereby justifying the motivation envisaged in the proposed approach.

1. Introduction

Bardeen-Cooper-Schrieffer[1] (BCS) in their original paper calculated the value of the effective interaction strength N_0V in which N_0 is the electronic density of states at the Fermi surface and V is the pairing potential arising from the electron-phonon (e-p) interaction. Their results were qualitative in nature and the superconducting properties were found to be insensitive to the precise form of the interaction. This theory was unable to explain adequately the isotope effect even in the simple non-transition metals. To explain the results in a more precise way, the modern superconducting theories require the introduction of three state parameters. These are: $\langle V_{ph} \rangle$, the electron-phonon coupling strength which measures the phonon mediated attractive electron-electron (e-e) interaction in the metal; $\langle V_c \rangle$, the Coulombian e-e coupling strength or simply the Coulomb pseudopotential which accounts for the effectiveness of the Coulomb repulsion in inhibiting superconductivity; and Z_0, the quasiparticle mass (or energy) renormalization parameter which takes into account the many-body effects due to e-p and Coulomb interactions. The calculations[2-4] of these superconducting-state parameters, performed using screened Coulomb potential for the e-p coupling and jellium models of the phonon spectrum, had some qualitative success in explaining the distribution of superconductivity in the periodic table, but with little quantitative agreement. Now, with the sufficiently improved knowledge of the phonon spectrum and electron-ion coupling, more realistic calculations are possible wherein one uses the theory of superconductivity, with its sophisticated Green's-function formalism[5-6], taking into account the retarded e-p interaction and including the important energy renormalization effects due to many-body interactions. McMillan[7] calculated the superconducting transition temperature and other superconducting properties as a function of the e-p and e-e coupling constants within the framework of the strong-coupling theory. McMillan argued that the e-p coupling constant depends primarily on the phonon frequencies rather than on the electronic properties of the metal. Allen and Cohen[8] had estimated the value of the e-p coupling constant and the transition temperature for several simple metals and alkaline earth metals using Animalu-Heine model potential[9] and empirical pseudopotentials (whenever possible) obtained from band-structure calculations fitted to Fermi surface measurements. Rajput and Gupta[10] calculated theoretically the three superconducting-state parameters for both non-superconductors and simple-metal superconductors. Their calculations differ from those of Morel and Anderson[4] first in using e-p and Coulomb-interaction matrix elements between Bloch states, secondly in incorporating for the e-p matrix element the form (known as point-ion model) suggested by Harrison[11] for the OPW form-factors, and lastly in the inclusion of renormalization effects due to e-p and Coulomb interactions. Rajput[12] also evaluated the values of the three superconducting-state parameters for both non-superconductors and simple-metal superconductors using the exact OPW form-factors based on the

*On leave from the Physics Department, Government College, Jhalawar.

model pseudopotential of Heine and Abarenkov.[13] Rajput and Jain[14] have studied the effect of the screening on the superconducting-state parameters for the sodium and zinc only using six different forms of the screening function.

In this paper, we intend to re-estimate the values of parameters $\langle V_{ph} \rangle$, $\langle V_c \rangle$, Z_0 and consequently the effective interaction strength N_0V for using them in the calculations of e-p and Coulomb-interaction matrix elements between plane wave states. The present work is an extension of the application of the approach of Rajput and Jain (whose present calculations are for Na and Zn only) to eleven metals, and aims at improving upon their results in as much as it involves a better form for $\langle V_c \rangle$ as also a precise determination of the repulsive strength parameter β. We also intend to undertake calculations of T_c for some simple metals on the lines followed by McMillan.[7]

2. Theory

The three fundamental parameters are defined as follows:[10]

$$\langle V_{ph} \rangle = \left(\frac{m^*}{m}\right) \frac{1}{\Omega_0 M} \frac{2k_F^3}{\pi^2 \omega_D^2} \times \int_0^1 x^3\, dx\, |V_s(x)|^2 \qquad \ldots(1)$$

$$\langle V_c \rangle = \frac{\left(\frac{m^*}{m}\right)\left(\pi k_F\right)^{-1} \int_0^1 \frac{dx}{x\epsilon(x)}}{1 + \left(\frac{m^*}{m}\right)\left(\pi k_F\right)^{-1} \ln\left(\frac{k_F^2}{10\,\theta_D}\right) \int_0^1 \frac{dx}{x\epsilon(x)}} \qquad \ldots(2)$$

and

$$Z_0 = Z_0^{ph} + Z_0^c - 1 \qquad \ldots(3)$$

The parameters $\langle V_{ph} \rangle$ and $\langle V_c \rangle$ are analogous to the parameters λ and μ^* of Morel and Anderson. $V_s(x)$ is the screened OPW form-factors per unit volume. Further Ω_0, M, Z, m^*/m, k_F, β, and ω_D are the atomic volume, ionic mass, ionic valency, reduced effective mass, Fermi wavenumber, repulsive δ-function contribution from orthogonalization of the conduction states to the core states, and Debye frequency respectively.

We adopt the Harrison's point-ion from potential and write $V_s(x)$ as follows:

$$V_s(x) = \left(-\frac{2\pi Z}{k_F^2 x^2} + \beta\right) \Big/ \epsilon(x) \qquad \ldots(4)$$

in which

$$\epsilon(x) = 1 + \frac{1}{2\pi k_F} \frac{1}{x^2} \left\{ 1 + \frac{1-x^2}{2x} \ln\left|\frac{1+x}{1-x}\right| \right\} \qquad \ldots(5)$$

is the Hartree dielectric screening function, and $x = q/2k_F$. Further Z_0^{ph}, the phonon contribution to the renormalization parameter, is given by:[10]

$$Z_0^{ph} \simeq 1 + \frac{10}{11} \langle V_{ph} \rangle \qquad \ldots(6)$$

and Z_0^c, the Coulomb contribution to the renormalization parameter, is given by:[10]

$$Z_0^c = Z_{DF}^{-1} \qquad \ldots(7)$$

where Z_{DF} is the quasiparticle renormalization parameter, which is taken directly from the estimates of Rice,[15] who lists its values as a function of electron density parameter, r_s. The McMillan's equation for transition temperature (T_c), in terms of our notation for e-p and e-e coupling strengths is given by the following equation:

$$T_c = \frac{\theta_D}{1{\cdot}45} \times \exp\left[-\frac{1{\cdot}04\left(1 + \langle V_{ph} \rangle\right)}{\langle V_{ph} \rangle - \langle V_c \rangle \left(1 + 0{\cdot}62 \langle V_{ph} \rangle\right)} \right] \qquad \ldots(8)$$

The present parameters $\langle V_{ph} \rangle$ and $\langle V_c \rangle$ can be expressed in the language of BCS as follows:

$$N_0 V = \frac{\langle V_{ph} \rangle - \langle V_c \rangle}{Z_0} \qquad \ldots(9)$$

We compare our calculated values of $N_0 V$ [using Eq. (9)] for superconductors with the experimental values obtained from the following relation:[3]

$$\left[N_0 V\right]_{expt1} \simeq \frac{-1}{\ln\left(T_c/0{\cdot}85\,\theta_D\right)} \qquad \ldots(10)$$

3. Results and Discussion

Table 1 lists the relevant parameters and data used in the calculations The results for the state parameters $\langle V_{ph} \rangle$, $\langle V_c \rangle$, Z_0 and $N_0 V$ for some non-superconductors are given in Table 2 and for superconductors in Table 3. For comparison, we have given other theoretical results also for the parameters $N_0 V$ along with $(N_0 V)_{expt1}$ as obtained from Eq. (10). Table 4 gives the calculated results

Table 1—Relevant Parameters and Data Used in Calculation

Element	r_s (au)	k_F (au)	Ω_0 (au)	m^*/m (Ref. 11, p. 128)	θ_D (K) (Ref. 10)	β (ryd) (Ref. 11, p. 57)
Na	3·931	0·4882	245·5	1·3	158	31·8
K	4·862	0·3947	481·4	1·1	90	44·4
Mg	2·650	0·7242	155·9	1·33	400	31·6
Ca	3·272	0·5865	293·5	0·8	230	50·6
Cu	2·661	0·7163	78·9	1·5	343	2·2
Hg	2·661	0·7213	157·8	1·8†	71·9‡	45·9
Al	2·069	0·9276	111·3	1·6	428	29·4
In	2·407	0·7972	175·3	1·3	108	39·0
Tl	2·480	0·7738	191·7	1·15	87	40·8
Sn	2·213	0·8674	181·5	1·2	199	41·1
Pb	2·298	0·8350	203·4	2·1	110	46·0

†This value is from Ref. 16.

‡This value is from Ref. 8.

Table 2—Superconducting-state Parameters for Non-Superconductors

Element	Present work					Effective interaction strength N_0V			
	$\langle V_{ph} \rangle$	$\langle V_c \rangle$	Z_0^{ph}	Z_0^c	Z_0	Present work	Ref. 10	Ref. 12	Ref. 4*
Na	0·1504	0·1846	1·1367	1·5699	1·7066	−0·0200	−0·006	−0·0836	+0·076
K	0·1275	0·1816	1·1159	1·7544	1·8703	−0·0289	+0·03	−0·027	+0·0695
Mg	0·1527	0·1628	1·1388	1·3812	1·5200	−0·0066	+0·01	—	+0·131
Ca	0·0820	0·1341	1·0745	1·4684	1·5429	−0·0337	−0·07	−0·0442	+0·1037
Cu	0·1862	0·1696	1·1692	1·3831	1·5523	+0·0106	+0·06	—	+0·0663

*The net effective interaction strength obtained with renormalization

for T_c obtained on the basis of Eq. (8) for some simple-metal superconductors and these are compared with the results found from the parameters of Rajput and Gupta[10] and with those based on the various pseudopotentials which are taken from Allen and Cohen.[8]

From Table 2 it may be inferred that the estimated values of the three superconducting-state parameters for the five non-superconductors reveal that our estimated effective interaction strengths are negative except for Cu, even which is meagrely positive. The reported calculations show that our results are much better than those of Rajput and Gupta as well as of Morel and Anderson. The fact that the present result of $N_0 V$ for Cu is much less positive as compared to those of Rajput and Gupta and more negative for Na, K and Mg, demonstrates that our results are much nearer to the actual physical situation prevailing in a metallic system. Our results for non-superconductors (Na, K, Ca, Mg and Cu) agree well with those based on our available present-day knowledge, that these metals are still non-superconducting.

Our results for N_0V lead to best agreement with the experimental data. A comparison with the results of Rajput and also with those of Morel and Anderson, (with renormalization effects) shows that our results lead to best values. For example, Rajput's value of N_0V in case of Hg is too low while that for Pb is higher, whereas our values are much nearer to N_0V_{exptl}. The present results for N_0V are also an improvement over those of Rajput and Gupta in case of the simple-metal superconductors In, Tl, Pb and Sn. Our value of electron-phonon interaction

Table 3—Superconducting-state Parameters of Simple-Metal Superconductors

Element	Present work					Effective interaction strength, N_0V				N_0V_{expt}
	$\langle V_{ph} \rangle$	$\langle V_e \rangle$	Z_0^{ph}	Z_0^e	Z_0	Present work	Ref. 10	Ref. 12	Ref. 4	
Hg	0·9980	0·1423	1·9007	1·3831	2·2838	0·3747	0·34	0·0763	0·1267	0·35
Al	0·4732	0·1497	1·4302	1·3089	1·7391	0·1860	0·18	0·0874	0·1322	0·175
In	0·8405	0·1250	1·7641	1·3495	2·1136	0·3385	0·16	—	0·1135	0·30
Tl	0·6263	0·1175	1·5694	1·3587	1·9281	0·2638	0·22	0·0496	0·1192	0·27
Sn	0·4352	0·1229	1·3956	1·3245	1·7201	0·1815	0·04	0·031	0·1395	0·26
Pb	1·2190	0·1461	2·1082	1·3369	2·4451	0·4387	0·54	0·6505	0·1226	0·39

Table 4—Experimental and Calculated Superconducting Transition Temperature (T_c) by Various Workers

Element	Method		T_c (K)
Al	Experimental		1·196
	Theoretical	Harrison (PW)	1·2
		HA[9]	2·6
		Aschroft[17]	3·0
		Harrison[10]	1·1
In	Experimental		3·404
	Theoretical	Harrison (PW)	3·9
		HA[9]	4·6
		Cohen[18]	7·2
		Aschroft V_1[19]	4·4
		Aschroft V_2[19]	4·0
		Harrison[10]	0·26
Hg	Experimental		4·153
	Theoretical	Harrison (PW)	3·5
		HA[9]	2·5
		Brandt[20]	3·4
		Harrison[10]	3·3
Tl	Experimental		2·39
	Theoretical	Harrison (PW)	1·6
		HA[9]	4·8
		Harrison[10]	0·82
Sn	Experimental		3·722
	Theoretical	Harrison (PW)	0·6
		HA[9]	6·2
		Weisz[21]	10·2
		Harrison[10]	$< 10^{-7}$
Pb	Experimental		7·193
	Theoretical	Harrison (PW)	6·9
		HA[9]	7·6
		Harrison[10]	10·4

PW, Present work; HA, Heine & Animalu

parameter in case of Sn is better than that of these authors, but it is worse than what had been predicted empirically by McMillan.[7]

We have also estimated the value of the transition temperature T_c, for these superconductors using McMillan's Eq. (8) as well as from Rajput and Gupta's values for the e-p and e-e coupling strengths. A comparison with the experimental values of T_c indicates that our calculated T_c values in case of Al, In, Pb and Hg are quite satisfactory as compared to others but our result in case of Tl and Sn is quite low. This reveals that our value of e-p interaction in case of Sn and Tl is low while in case of Al, In, Hg and Pb it is quite satisfactory. This fact can also be judged from the comparison of our e-p interaction strength with McMillan's empirical values. Further, the present T_c values are definitely better than those that would be obtained on the basis of parameters calculated by Rajput and Gupta. Table 4 also supports the conclusion that our values are superior in comparison to those found by any others.

However, it may be pointed out that the form of electron-ion pseudopotential employed in this paper is really an oversimplification of the actual state of affairs inside a metal. In fact, one may expect considerable improvement by adopting a realistic potential instead of the crude point-ion model. It is also common knowledge that the various theories of screening available in the literature differ from each other to a large extent in the small wavevector region, which is of interest in the present problem. Therefore, for simplicity we have embraced the Hartree form of screening without incorporating its exchange and correlation modifications, as the expected errors in the various screenings would not permit any definite conclusion to be drawn. The calculations based on a more realistic electron-ion pseudopotential as well as a model screened potential are in progress and the corresponding results will be reported in due course.

Acknowledgement

The authors acknowledge greatefully the computer and departmental facilities extended respectively by Prof. B Saraf and Dr M P Saksena. One of us (SCJ) wishes to express his gratitude to the University Grants Commission, New Delhi for offering him a teacher-fellowship.

References

1. Bardeen J, Cooper L N & Schrieffer J R, *Phys. Rev.*, **108** (1957), 1175.
2. Pines D, *Phys. Rev.*, **109** (1958), 280.
3. Morel P, *J. Phys. Chem. Solids*, **10** (1959), 277.
4. Morel P & Anderson P W, *Phys. Rev.*, **125** (1962), 1263.
5. Schrieffer J R, *Theory of superconductivity*, (Benjamin Inc., New York), 1964.
6. Abrikosov A A, Gorkov L P & Dzyaloshinski I E, *Method of quantum field theory in statistical physics*, (Prentice Hall, Englewood Cliffs N J), 1963.
7. McMillan W L, *Phys. Rev.*, **167** (1968), 331.
8. Allen P B & Cohen M L, *Phys. Rev.*, **187** (1969), 525.
9. Animalu A O E & Heine V, *Phil. Mag.*, **12** (1965), 1249.
10. Rajput J S & Gupta A K, *Phys. Rev.*, **181** (1969), 743.
11. Harrison W A, *Pseudopotentials in the theory of Metals*, (Benjamin Inc., New York), 1966.
12. Rajput J S, *Phys. Status Solidi*, (*b*), **45** (1971), 287.
13. Heine V & Abarenkov Z, *Phil. Mag.*, **9** (1964), 451.
14. Rajput J S & Jain L K, *Indian J. pure appl. Phys.*, **14** (1976), 533.
15. Rice T M, *Ann. Phys.*, **31** (1965), 100.
16. Daunt J G, *Prog. Low-Temp. Phys.*, **1** (1955), 210.
17. Ashcroft N W, *Phil. Mag.*, **8** (1963), 2055.
18. Cohen M L & Bergstresser T K, *Phys. Rev.*, **141** (1966), 789.
19. Ashcroft N W & Lawrence W E, *Phys. Rev.*, **175** (1968), 938.
20. Brandt G B & Ryne J A, *Phys. Rev.*, **148** (1966), 644.
21. Weisz G, *Phys. Rev.*, **149** (1966), 504.

Indian Journal of Pure & Applied Physics
Vol. 18, July 1980, pp. 494-498

Thermodynamics of Manganese-bearing Binary Substitutional Solutions

R D Agrawal, V N S Mathur & M L Kapoor
Department of Metallurgical Engineering, Roorkee University, Roorkee 247 672

Received 30 *April* 1979; *revised received* 20 *August* 1979

Applicability of new statistical thermodynamic approach based on free-volume theory is tested on manganese-bearing binary substitutional alloy systems. A good agreement is observed between the experimental data and those computed using parameters at infinite dilution and based on expressions developed in this approach for the entire range of composition of these alloy systems. Asymmetric nature of some systems is also explained successfully.

1. Introduction

Metallic solutions, because of their importance in alloy-development and chemical metallurgy, have been an important topic of both theoretical and experimental study. Several theoretical models,[1-6] based on quasi-crystalline lattice concept, have been developed to explain the behaviour of these solutions and have been critically reviewed by Kapoor.[7] But these do not take into account the changes in the free-volumes of atoms on mixing and hence only explain the behaviour of such solutions to a limited extent. Recently, Kapoor[8] has developed a new approach based on the free-volume theory to explain the properties of binary substitutional solutions and has tested it successfully on silver-bearing, iron-bearing,[9] copper-bearing,[10] zinc-bearing,[11] lead-bearing[12] and several other systems also. The aim of the present work is to test the applicability of this new approach to manganese-bearing binary substitutional alloy-systems.

2. Theory

The basic assumptions of the new approach are :

(i) A metallic solution, liquid or solid, of substitutional components can be assumed to form a quasi-crystalline lattice with each atom having an average coordination number, Z.

(ii) Each atom moves around its lattice site, within a cell which is determined by the interaction of this atom with its nearest neighbours.

(iii) The energy of an atom is a function of the type of atoms in its first coordination shell.

On the basis of expressions developed for the changes in energy and free-volume of different atoms on mixing, Kapoor[8] has evaluated the configurational partition function of the substitutional binary alloy system (A-B) and on further computation and substitution of theoretical parameters, in terms of experimentally determinable parameters, has arrived at the following expressions for the excess thermodynamic properties of the solution, using partial molar properties and self-interaction parameters at infinite dilution of each of the components.

$$\Delta G^{XS}_{\mathrm{Mix}} = \left(\Delta \bar{G}^{XS}_{A,\infty} N_B + \Delta \bar{G}^{XS}_{B,\infty} N_A \right) N_A N_B + \left[\left(\epsilon^A_A/2 - \Delta \bar{G}^{XS}_{B,\infty} + 2\Delta \bar{G}^{XS}_{A,\infty} \right) N_B + \left(\epsilon^B_B/2 - \Delta \bar{G}^{XS}_{A,\infty} + 2\Delta \bar{G}^{XS}_{B,\infty} \right) N_A \right] N_A^2 N_B^2 \quad \ldots (1)$$

$$\Delta H_{\mathrm{Mix}} = \left(\Delta \bar{H}_{A,\infty} N_B + \Delta \bar{H}_{B,\infty} N_A \right) N_A N_B + \left[\left(\rho^A_A/2 - \Delta \bar{H}_{B,\infty} + 2\Delta \bar{H}_{A,\infty} \right) N_B + \left(\rho^B_B/2 - \Delta \bar{H}_{A,\infty} + 2\Delta \bar{H}_{B,\infty} \right) N_A \right] N_A^2 N_B^2 \quad \ldots (2)$$

and

$$\Delta S^{XS}_{\mathrm{Mix}} = \left(\Delta \bar{S}^{XS}_{A,\infty} N_B + \Delta \bar{S}^{XS}_{B,\infty} N_A \right) N_A N_B + \left[\left(\sigma^A_A/2 - \Delta \bar{S}^{XS}_{B,\infty} + 2\Delta \bar{S}^{XS}_{A,\infty} \right) N_B + \left(\sigma^B_B/2 - \Delta \bar{S}^{XS}_{A,\infty} + 2\Delta \bar{S}^{XS}_{B,\infty} \right) N_A \right] N_A^2 N_B^2 \quad \ldots (3)$$

In the above expressions, $\Delta \bar{G}^{XS}_{i,\infty}$, $\Delta \bar{H}_{i,\infty}$ and $\Delta \bar{S}^{XS}_{i,\infty}$ are respectively the partial molar excess free-energy, enthalpy and excess entropy of mixing of the constituent i at infinite dilution; also ϵ^i_i, ρ^i_i and σ^i_i are the free-energy, enthalpy and entropy of self-interaction respectively of the component i in its dilute solution.

In case of random-mixing of components, only four parameters $\Delta \bar{H}_{A,\infty}$, $\Delta \bar{H}_{B,\infty}$, $\Delta \bar{S}^{XS}_{A,\infty}$ and $\Delta \bar{S}^{XS}_{B,\infty}$ are required to evaluate all the thermodynamic properties at any concentration as, for these systems, the self-interaction parameters (interaction heats and entropies) are only functions of these infinite dilution properties and are evaluated using the following expressions:

$$\rho^A_A = R\left(\frac{\partial^2 \ln \gamma_A}{\partial T \partial N_A}\right)_{N_B \to 1}$$

$$= 2\left(\Delta \bar{H}_{B,\infty} - 2\Delta \bar{H}_{A,\infty}\right) \quad \ldots(4)$$

$$\rho^B_B = R\left(\frac{\partial^2 \ln V_B}{\partial T \partial N_B}\right)_{N_B \to 1}$$

$$= 2\left(\Delta \bar{H}_{A,\infty} - 2\Delta \bar{H}_{B,\infty}\right) \quad \ldots(5)$$

$$\sigma^A_A = \frac{\partial}{\partial T}\left[R\,T\left(\frac{\partial \ln \gamma_A}{\partial N_A}\right)_{N_B \to 1}\right]$$

$$= 2\left(\Delta \bar{S}^{XS}_{B,\infty} - 2\Delta \bar{S}^{XS}_{A,\infty}\right) \quad \ldots(6)$$

$$\sigma^B_B = \frac{\partial}{\partial T}\left[R\,T\left(\frac{\partial \ln \gamma_B}{\partial N_B}\right)_{N_A \to 1}\right]$$

$$= 2\left(\Delta \bar{S}^{XS}_{A,\infty} - 2\Delta \bar{S}^{XS}_{B,\infty}\right) \quad \ldots(7)$$

and therefore,

$$\epsilon^A_A = R\,T\left(\frac{\partial \ln \gamma_A}{\partial N_A}\right)_{N_B \to 1} = \rho^A_A - R\,T\,\sigma^A_A$$

$$= 2\left(\Delta \bar{G}^{XS}_{B,\infty} - 2\Delta \bar{G}^{XS}_{A,\infty}\right)$$

and,

$$\epsilon^B_B = R\,T\left(\frac{\partial \ln \gamma_B}{\partial N_B}\right)_{N_A \to 1} = \rho^B_B - R\,T\,\sigma^B_B$$

$$= 2\left(\Delta \bar{G}^{XS}_{A,\infty} - 2\Delta \bar{G}^{XS}_{B,\infty}\right) \quad \ldots(9)$$

where γ_A and γ_B are respectively the activity coefficients of component A with mole fraction N_A and of B with mole fraction N_B in their solutions.

From study of above equations, it is evident that the functions $\Delta \bar{G}^{XS}_{\text{Mix}}/N_A N_B$, $\Delta H_{\text{Mix}}/N_A N_B$ and $\Delta \bar{S}^{XS}_{\text{Mix}}/N_A N_B$ will have linear variation with the mole fraction N_B of the component B of the system, for a randomly distributed solution and any deviation from this ideal linear behaviour indicates a preferential distribution of atoms of the solution because of their mutual interactions.

3. Applications and Conclusions

Using the thermodynamic data, tabulated by Hultgren *et al.*,[13] for different manganese-bearing binary substitutional alloy systems (A-B), values of infinite dilution parameters $\Delta \bar{G}^{XS}_{A,\infty}$, $\Delta \bar{G}^{XS}_{B,\infty}$, $\Delta \bar{H}^{XS}_{A,\infty}$ $\Delta \bar{H}_{B,\infty}$, $\Delta \bar{S}^{XS}_{A,\infty}$, $\Delta \bar{S}^{XS}_{B,\infty}$, ϵ^A_A, ϵ^B_B, ρ^A_A, ρ^B_B, σ^A_A and σ^B_B are computed for both the components A and B of the solution, on the basis of procedure outlined in Ref. 8, and are presented in Tables 1 and 2. Table 3 presents some other properties of components of these solutions such as their positions in periodic table, atomic number, atomic radius, atomic volume, electronegativity and lattice structure.

Thermodynamic properties of these different alloy systems, calculated on the basis of these experimental infinite dilution parameters for the entire range of composition of binary alloy systems are plotted (by smooth curves) in Figs. 1 to 3 together with the experimental data (shown by points). These figures show very good correspondence between the calculated and experimental data, thereby indicating the successful applicability of the present approach. As is evident from these curves, the asymmetric behaviour of some of these systems is also explained clearly.

It is important to note that none of the earlier models,[1-7] has so successfully explained all the three thermodynamic parameters $\Delta G^{XS}_{\text{Mix}}$, ΔH_{Mix} and $\Delta S^{XS}_{\text{Mix}}$ of the solution, to the same degree of accuracy as the present one, for the entire range of composition. It is further to be noted from these curves that the thermodynamic properties of the solution at any desired composition can be calculated using this approach but needs a knowledge of both the partial molar properties and self-interaction parameters as indicated above, all of which can be experimentally determined accurately.

Miedema[14] has arrived at certain relations semi-empirically to calculate the enthalpies of mixing at

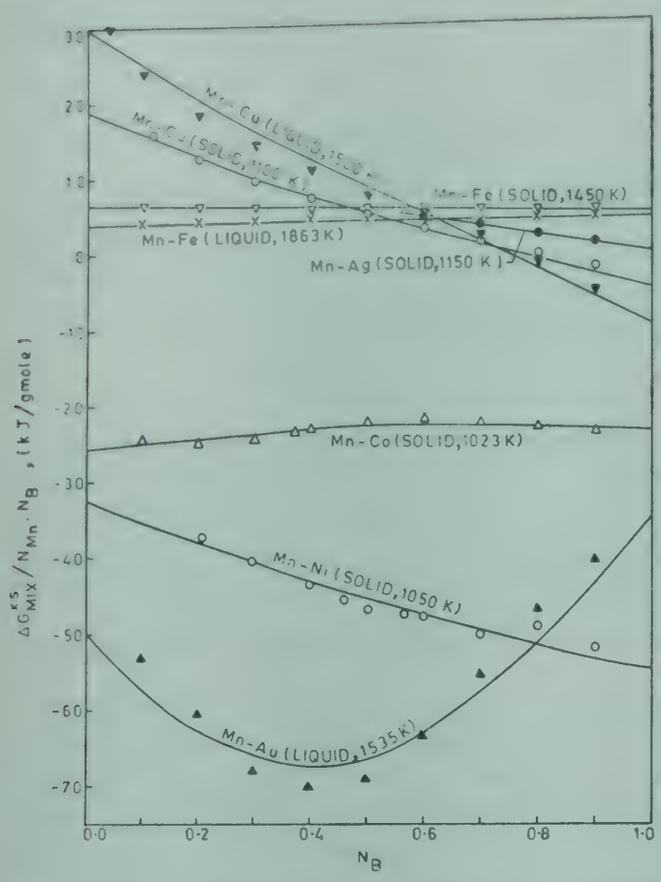

Fig. 1—$\Delta G^{XS}_{Mix}/N_{Mn} \cdot N_B$ versus N_B for manganese-bearing binary alloy systems

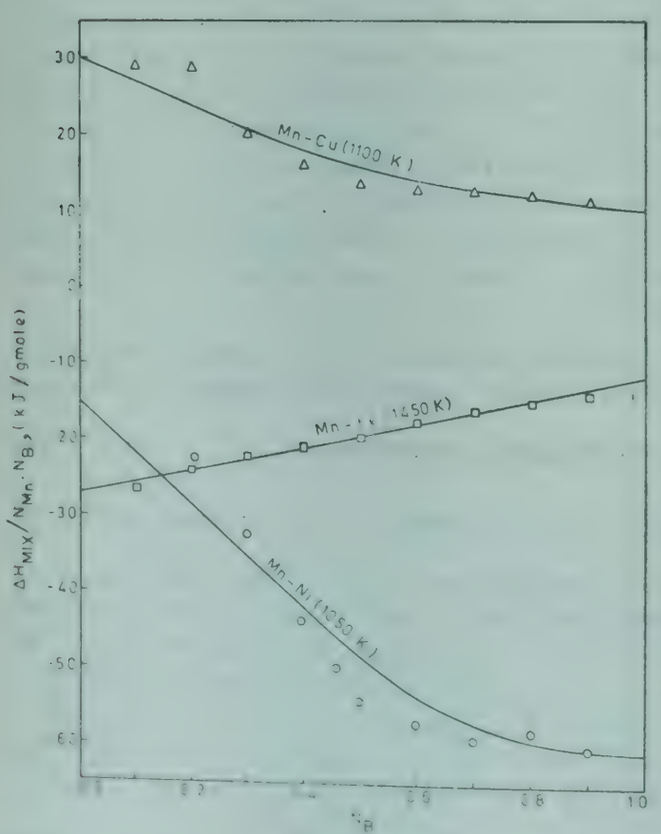

Fig. 2—$\Delta H_{Mix}/N_{Mn} \cdot N_B$ versus N_B for manganese-bearing solid binary alloy systems

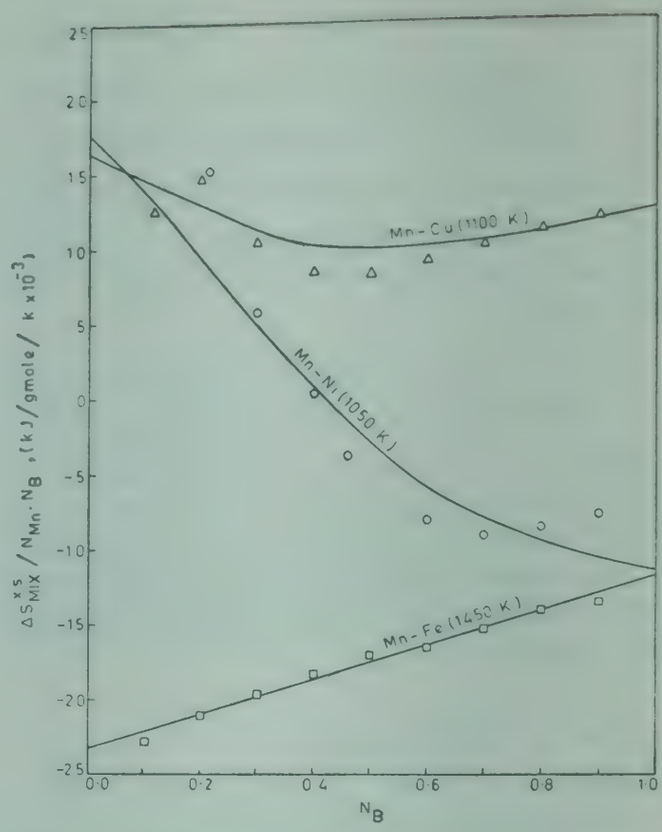

Fig. 3—$\Delta S^{XS}_{Mix}/N_{Mn} \cdot N_B$ versus N_B for manganese-bearing solid binary alloy systems

infinite dilution but his expressions also give values which are far from satisfactory for several systems for which these parameters are known.

Some qualitative characteristics of the infinite dilution parameters of the solutes, which obviously depend upon their properties, from an analysis of the data presented in Tables 1-3 are stated below:

1. Among the solutes of the same group, $\Delta \overline{G}^{XS}_{B,\infty}$ decreases with increase in atomic number of solute from Fe to Co to Ni (of VIII group) and from Cu to Ag to Au (of I-B group). However, $\Delta \overline{H}_{B,\infty}$ decreases in the order from Fe to Ni (of VIII group) and is higher for Cu than for both these metals.
2. In the same period, the $\overline{H}_{B,\infty}$ increases with an increase in atomic radius from Ni to Fe to Cu (of 4th period) and the $\Delta \overline{G}^{XS}_{B,\infty}$ from Ni to Co to Fe to Cu (of 4th period).
3. Among the fcc metals, $\Delta \overline{G}^{XS}_{B,\infty}$ decreases from Cu to Ag to Au (of I-B group) and nickel (of VIII group) has a value in between those for Ag and Au.
4. In the same period, $\Delta \overline{G}^{XS}_{B,\infty}$ decreases with increase in distance from manganese, e.g. from Fe to Co to Ni (of VIII group), Cu (of I-B group)

Table 1—Partial Molar Properties at Infinite Dilution of Binary Manganese-bearing Substitutional Alloy Systems

System (A-B)	Temperature K	State	$\Delta \bar{G}^{XS}_{A,\infty}$	$\Delta \bar{G}^{XS}_{B,\infty}$	$\Delta \bar{H}_{A,\infty}$	$\Delta \bar{H}_{B,\infty}$	$\Delta \bar{S}^{XS}_{A,\infty}$ ($\times 10^{-3}$)	$\Delta \bar{S}^{XS}_{B,\infty}$ ($\times 10^{-3}$)
Mn-Ni	1050	Solid	−54·50	−32·50	−11·50	−27·50	−10·75	17·50
Mn-Ag	1150	do	−0·50	12·00	—	—	—	—
Mn-Co	1023	do	−23·50	−25·50	—	—	—	—
Mn-Cu	1100	do	−5·00	19·00	10·00	30·00	12·50	16·25
Mn-Fe	1450	do	5·00	6·50	−60·00	−15·00	−11·75	−23·25
Mn-Au	1535	Liquid	−35·00	−50·00	—	—	—	—
Mn-Cu	1500	do	−10·00	30·00	—	—	—	—
Mn-Fe	1863	do	4·25	4·00	—	—	—	—

All values are in kJ/g-atom units.

Table 2—Self-Interaction Parameters of Components of Binary Manganese-bearing Substitutional Alloy Systems

System (A-B)	Temperature K	State	ϵ^A_A	ϵ^B_B	ρ^A_A	ρ^B_B	σ^A_A ($\times 10^{-3}$)	σ^B_B ($\times 10^{-3}$)
Mn-Ni	1050	Solid	140·0	10·0	−8·5	86·0	41·5	−117·5
Mn-Ag	1150	do	26·0	−49·0	—	—	—	—
Mn-Co	1023	do	51·0	62·0	—	—	—	—
Mn-Cu	1100	do	52·0	−94·0	0·0	−110·0	−42·5	−65·0
Mn-Fe	1450	do	−7·0	−16·0	130·0	−102·0	0·5	69·5
Mn-Au	1535	Liquid	128·9	−72·5	—	—	—	—
Mn-Cu	1500	do	95·0	−150·0	—	—	—	—
Mn-Fe	1863	do	−9·0	−7·5	—	—	—	—

All values are in kJ/g-atom units.

Table 3—Characteristics of Components of Binary Manganese-bearing Substitutional Alloy Systems

Element	Position in periodic table: Group	Position in periodic table: Period	Atomic number	Atomic radius Å	Atomic volume Å³	Electro-negativity	Structure
Mn	VIIB	4	25	1·26	7·39	1·5	Cubic
Fe	VIII	4	26	1·26	7·10	1·8	bcc
Co	VIII	4	27	1·25	6·7	1·8	hcp
Ni	VIII	4	28	1·24	6·6	1·8	fcc
Cu	IB	4	29	1·28	7·10	1·9	fcc
Ag	IB	5	47	1·44	10·3	1·9	fcc
Au	IB	6	79	1·44	10·2	2·4	fcc

has a higher value of $\Delta \bar{G}^{XS}_{B,\infty}$ than these solutes; $\Delta \bar{H}_{B,\infty}$ decreases from Fe to Ni (of VIII group); however both $\Delta \bar{H}_{B'\infty}$ and $\Delta \bar{S}^{XS}_{B,\infty}$ increase from Fe to Cu.

5. No defined regular effect of electronegativity has been noted.
6. ρ^B_B increases from Cu to Fe to Ni in the same period (4th period), whereas ϵ^B_B increases in the same group (of VIII group) in the order Fe to Ni to Co and from Cu to Au to Ag (of I-B group). Thus no regularly defined effect of either an increase or decrease of atomic number, electronegativity, atomic radius or atomic volume, on these parameters is observed.

References

1. Ising E, *Z. Phys.*, **31** (1925), 253.
2. Hildebrandt J H, *J. Am. chem. Soc.*, **6** (1929), 221.
3. Kirkwood J G, *J. chem. Phys.*, **6** (1938), 70.
4. Guggenheim E A, *Mixtures* (Oxford University Press, Oxford), 1952.
5. Mathieu J C *et al.*, *J. chem. Phys.*, **62** (1965), 1289.
6. Lupis C H P & Elliot J F, *Acta Met.*, **15** (1967), 265.
7. Kapoor M L, *Int. Met. Rev.*, **20** (1975), 150.
8. Kapoor M L, *Trans. Japan Inst. Metals*, **19** (1978), 109.
9. Agrawal R D, Mathur V N S & Kapoor M L, *Z. Metallkunde*, **20** (1979), 536.
10. Agrawal R D, Mathur V N S & Kapoor M L, *Trans. Japan Inst. Metals*, **20** (1979), 54.
11. Agrawal R D, Mathur V N S & Kapoor M L, *Z. Metallkunde*, **20** (1979), 722.
12. Agrawal R D, Mathur V N S & Kapoor M L, *Trans. Indian Inst. Metals*, in press.
13. Hultgren R *et al.*, *Selected values of thermodynamic properties of metals and alloys* (Wiley, New York), 1973.
14. Miedema A R, *J. Less Common Metals*, **46** (1976), 67.

Indian Journal of Pure & Applied Physics
Vol. 18, July 1980, pp. 499-503

Isothermal Compressibility Behaviour of Aqueous Solutions of *tert*-Butyl Alcohol at 25°C

K J Patil & D N Raut
Department of Chemistry, Institute of Science, Nagpur 1

Received 16 *April* 1979; *revised received* 22 *November* 1979

The measurements of sound velocity in aqueous solutions of *tert*-butyl alcohol in the concentration range of 0-8 mole% at 25°C are reported. Using the density, thermal expansion coefficient and volumetric specific heat data, the calculations of adiabatic and isothermal compressibilities were made. The calculated parameters further enable to calculate specific heat at constant volume, the apparent molal isothermal compressibility, the thermal pressure coefficient, energy-volume coefficient (internal pressure) and the cohesive energy density at different concentrations. It has been observed that comparative insensitivity of energy volume coefficient in low concentration region (> 3 mole% of alcohol) results in a slight decrease in apparent molal isothermal compressibility and hence a minimum in isothermal compressibility at 2·6-3 mole% of alcohol. The results have been explained on the basis of strengthening of water structure by means of substitutional dissolution of *tert*-butyl alcohol molecules resembling clathrate-hydrate-type equilibria (which may be insensitive to pressure) in the low concentration region.

1. Introduction

A number of the abnormal properties of pure water can be accounted for in terms of a 'mixture' hypothesis. Abnormalities in the properties of aqueous solutions are attributed to changes in the water structure caused by the added components. The equilibrium existing in the liquid and in aqueous solutions can be written as:

$(H_2O)_b = (H_2O)_d$, where b and d refer to the 'bulky' and 'dense' states respectively. The thermodynamic and physical properties of alcohol-water mixtures have been studied extensively and are well reviewed by Franks and Ives.[1] The properties of interest are the partial molar volumes ($\bar{V}_2$) and their limiting values $\bar{V}_2^0$, the partial molar expansivity ($\bar{\alpha}_2$), adiabatic compressibility $(\phi_K)_{ad}$, the thermal pressure coefficient and the temperature of maximum density. The information regarding these properties has been lucidly reviewed by Frank.[2] The excess limiting partial molar volume $\bar{V}_2^{0E} = (\bar{V}_2^0 - V_{liq})$ for alcohols is always negative. It has been shown that $\bar{V}_2^{0E}$ depends on the size of the solute molecule and its configuration. It has also been established that for dilute solutions, $\bar{\alpha}_2^{0E}$ is negative;[2] with rising concentration $\bar{\alpha}_2^E$ increases and eventually becomes positive at a concentration characteristic of a given solute. The negative $\bar{\alpha}_2^E$ is related to the well known maximum density effect and the property possessed by a number of simple solutes of raising the temperature of maximum density of water has been studied in detail.[2] Unfortunately, for a comparison involving a range of solutes, $\bar{V}_2^E$ and $\bar{\alpha}_2^E$ must be related to reference standard states because they contain sizable contributions due to the intrinsic volumes of the solute molecules, but this problem does not arise with $(\phi_K)_{ad}$ which is solely due to changes in the interactions within the system. The slopes of $\bar{V}_2^E$-x_2 (mole-fraction of solute) curves provide information concerning solute-solute interaction in dilute solution.[2] It has also been shown that for aqueous solution of amines, minimum in $\bar{V}_2$-x_2 curves and a minimum in adiabatic compressibility (β_{ad}) occurs at about the same concentration.[4,5] There appears to exist a one-to-one correspondence between the limiting volumes and compressibilities as well as the slopes of the concentration plots of the partial volumes and apparent compressibility. Thus, available information on dilute solutions of many non-electrolytes indicates (Franks[6]) formation of clathrate hydrate-type structure in solution.

Recently, Kaulgud and Patil[4,5] have shown that for aqueous solutions of methyl amine, dimethyl amine and *tert*-butyl amine, $(\phi_K)_{ad}$ goes through a minimum. The same effect has been observed for aqueous solutions of methanol and ethanol.[7] It has been postulated that this effect must be related (or similar) to temperature of maximum density of water, indicating that the structural interactions are insensitive to pressure effects. Although the sound velocity and adiabatic compressibility measurements have been reported for *tert*-butyl alcohol-water system,[8,9] such analysis has not been made. At the same time, very few points exist in low concentration region. Since, the structural interactions are more pronounced

in case of *tert*-butyl alcohol and many properties have been studied in detail, there is a need for precise adiabatic compressibility data to obtain information regarding the pressure effect. With this view in mind, the authors have measured the sound velocity in low concentration region for *tert*-butyl alcohol-water system at 25°C and using the density data of Desnoyers *et al.*,[10] the adiabatic compressibilities were calculated.

Adiabatic compressibilities (β_{ad}) can be converted to isothermal compressibilities (β_{iso}) with the relation

$$\delta = \beta_{iso} - \beta_{ad} = \frac{\alpha^2 T}{\sigma} \qquad \ldots(1)$$

where α is the coefficient of thermal expansion and σ the volumetric specific heat. Since α and σ are not always available as a function of concentration, the difference δ is always ignored in the interpretation of aqueous non-electrolyte solutions. Fortunately now α and σ are both available[10,11] for *tert*-butyl alcohol in the concentration region of our interest. We have coupled our data with these properties and obtained the values of β_{iso} in the concentration of 0-8 mole% of alcohol, and also other properties like apparent molal isothermal compressibility $(\phi_K)_{iso}$, specific heat at constant volume (C_V), the thermal pressure coefficient $(\partial P/\partial T)_V$ and the energy volume coefficient $(\partial U/\partial V)_T$ were calculated. This analysis permitted us to examine various relationships between the structural properties of the solute (i.e. *tert*-butyl alcohol) and their ability to affect the structure of liquid water.

2. Experimental Details

Tertiary butyl alcohol (BDH grade) was dried over calcium oxide and distilled twice at atmospheric pressure in an efficient still. The refractive index and density (0·7802 g/cc at 25°C) agreed well with accepted values (density = 0·7804 g/cc at 25°C, Ref. 12.) The sound velocity for the liquid was found to be 1121 m/sec at 25°C. Aqueous mixtures were prepared by weight using doubly distilled water in glass stoppered conical flasks.

The sound velocity was measured at 2 MHz by means of ultrasonic Interferometer (NPL patent). The interferometer cell containing sample liquid was maintained at constant temperature (25±0·1°C) by circulating water through it by means of U-10 ultra-thermostat (±0·02°C). The least count of the micrometer screw was 0·0001 cm, and each time measurements of 25 maxima in current were noted. The instrument was calibrated with distilled water and benzene. The sound velocity for water was 1498 m/sec at 25°C which agrees very well with the best literature value, i.e. 1497 m/sec obtained by sing-around technique.[13] Considering the standard deviation in wavelength measurements and temperature accuracy, our velocity measurements are reproducible within ± 1 m/sec. The velocity measurement was repeated at least thrice for each solution.

3. Calculations and Results

The adiabatic compressibilities (β_{ad}) were calculated using our sound velocity (u) data and density data obtained from literature[10] with the usual Laplace equation. The isothermal compressibilities (β_{iso}) were calculated using Eq. (1). The necessary thermal expansion coefficient (α) was obtained from the analysis of apparent molal expansivity (ϕ_E) reported by Neal and Goring.[11] Similarly the volumetric specific heat ($\sigma = c_v d$) was also obtained from literature.[10] The apparent molal isothermal compressibilities $(\phi_K)_{iso}$ were calculated by the expression:

$$(\phi_K)_{iso} = \frac{1000\,(\beta_{iso} - \beta_{0iso})}{m.d_0} + \beta_{iso}.\phi_V \qquad \ldots(2)$$

where m is the molality, ϕ_V is the apparent molal volume of the solute while d_0 and β_{0iso} represent the density and isothermal compressibility of water respectively. Our accuracy in β_{ad} is ± 0·1% which causes an error of $\pm 1 \times 10^{-10}$ cm²/dyne at the lowest concentration for $(\phi_K)_{ad}$. The calculations of specific heat at constant volume (C_V) at different concentrations were made by using the relation

$$\frac{\beta_{iso}}{\beta_{ad}} = \frac{C_p}{C_V} \qquad \ldots(3)$$

Similarly the thermal pressure coefficients $(\partial P/\partial T)_V$ were calculated[14] from Eq. (4)

$$\left(\frac{\partial P}{\partial T}\right)_V = \frac{\alpha}{\beta_{iso}} \qquad \ldots(4)$$

Energy volume coefficients, $(\partial U/\partial V)_T$, were calculated from the thermal pressure coefficients using the 'thermodynamic equation of state'

$$\left(\frac{\partial U}{\partial V}\right)_T = T\left(\frac{\partial P}{\partial T}\right)_V - P \qquad \ldots(5)$$

For solutions investigated in this work $T\,(\partial P/\partial T)_V$ is very much greater than the applied pressure P and Eq. (5) reduces to

$$\left(\frac{\partial U}{\partial V}\right)_T = T\left(\frac{\partial P}{\partial T}\right)_V \qquad \ldots(6)$$

The energy-volume coefficient is related to the cohesive energy density $(\Delta U_V/V)_T$ by Eq. (7) [Ref. 15]:

$$\left(\frac{\partial U}{\partial V}\right)_T = n\left(\frac{\Delta U_V}{V}\right)_T \qquad \ldots(7)$$

where ΔU_V is the energy of vaporization of the liquid to the perfect gas state and V is the molar volume

Table 1—Calculated Values of Different Thermodynamical Parameters at Different Molar Concentrations

Concentration mole%	Velocity (u) m/sec	$\beta_{ad} \times 10^{12}$ cm^2,dyne^{-1}	$\beta_{iso} \times 10^{12}$ cm^2,dyne^{-1}	$\phi_{K\,iso} \times 10^{10}$ cm^3,dyne^{-1} mol^{-1}	C_V JK^{-1}g^{-1}	$(\partial U/\partial V)_T$ atm	$(\Delta U/V)_T$ atm	$n \times 10^2$
0·00	1498·0	44·70	45·16	—	4·136	1683	22684	7·41
0·27	1506·1	44·31	44·78	14	4·166	1699	22462	7·56
0·64	1522·7	43·44	43·92	4	4·193	1763	22265	7·88
0·93	1532·9	42·95	43·43	4	4·211	1847	22034	8·38
1·13	1542·5	42·47	42·98	3	4·230	1857	21930	8·47
1·61	1559·3	41·68	42·22	4	4·269	1977	21580	9·16
2·11	1573·1	41·04	41·68	7	4·303	2174	21266	10·33
2·40	1584·7	40·51	41·24	7	4·312	2339	21054	11·11
2·63	1606·3	39·47	40·26	2	4·327	2511	20852	12·04
3·11	1609·8	39·41	40·42	8	4·343	2814	20638	13·63
3·75	1613·2	39·31	40·62	15	4·366	3212	20286	15·83
4·34	1612·5	39·45	40·86	17	4·402	3613	19945	18·12
4·95	1605·8	40·08	42·14	25	4·375	4016	19603	20·49
5·21	1604·8	40·05	42·80	29	4·320	4470	19294	23·16
6·92	1578·4	41·63	46·33	45	4·142	5382	18982	28·36
7·64	1552·4	45·67	—	—	—	—	—	—

of the liquid at temperature T. The energy of vaporization per mole of mixture can be calculated using the Eq. (8)

$$\Delta U_V = X_1.\Delta H_{V,1} + X_2.\Delta H_{V,2} - \Delta H_M - RT \quad \ldots(8)$$

The quantities $\Delta H_{V,1}$ and $\Delta H_{V,2}$ are enthalpies of vaporization of component 1 and 2, respectively to the perfect gas state and ΔH_M is the heat of mixing per mole of mixture. The enthalpies of vaporization of water and *tert*-butyl alcohol to the perfect gas state at 25°C are 10·52 kcal mole^{-1} and 11·15 kcal mole^{-1} respectively. Energies of vaporization for the various alcohol-water mixtures were calculated using these data and the values of heats of mixing taken from the literature.[1] Division of the ΔU_V values by the corresponding molar volumes (calculated by us) results in the cohesive energy densities. The parameters U, β_{ad}, β_{iso}, $\phi_{K(iso)}$ C_V, $(\partial U/\partial V)_T$, $(\Delta U/V)_T$ and n at different concentrations are listed in Table 1 and except β_{ad} all are represented graphically in Figs. 1 and 2.

4. Discussion

Fig. 1 shows that sound velocity goes through maximum at about 3·75 mole% of alcohol which well corroborates with the concentration of minimum in apparent molal volume and maximum in apparent molal specific heat.[10] The β_{iso} goes through a minimum at a slightly lower concentration (2·63 mole%) which also well corroborates with the concentration of minimum partial molal volume of alcohol.[16] Thus, it can be said that the observed behaviour may be due to maximum solvent structure stabilization by the addition of *tert*-butyl alcohol molecules in a concentration region up to 3 mole% of alcohol. Similarly $C_V = (\partial U/\partial T)_V$ also goes through maximum at about the same concentration. Presently, it is not possible for the authors to calculate the separate contributions from the translational, rotational and vibrational degrees of freedom from the total C_V values. But one must note that C_V values are smaller than C_P as required and vary with concentration in a similar way.

The $\phi_{K(iso)}$-conc. curve reveals a slight negative slope up to 2·6 mole% but after that there is a sudden increase in it thus pointing out the similarity between the volumetric and compressibility behaviour. It has also been shown that activity coefficient of water goes through a mimimum at about the same concentration.[17] There is no way to explain this behaviour but it has to be postulated that *tert*-butyl alcohol molecules get trapped inside the cages in water, replacing the monomeric water molecules from the framework site affecting the compressibility of water to a minimum extent. One must also note that below 2·6 mole% of alcohol, the compressibility of solute is less than that of water, i.e. 8×10^{-10} cm^2.

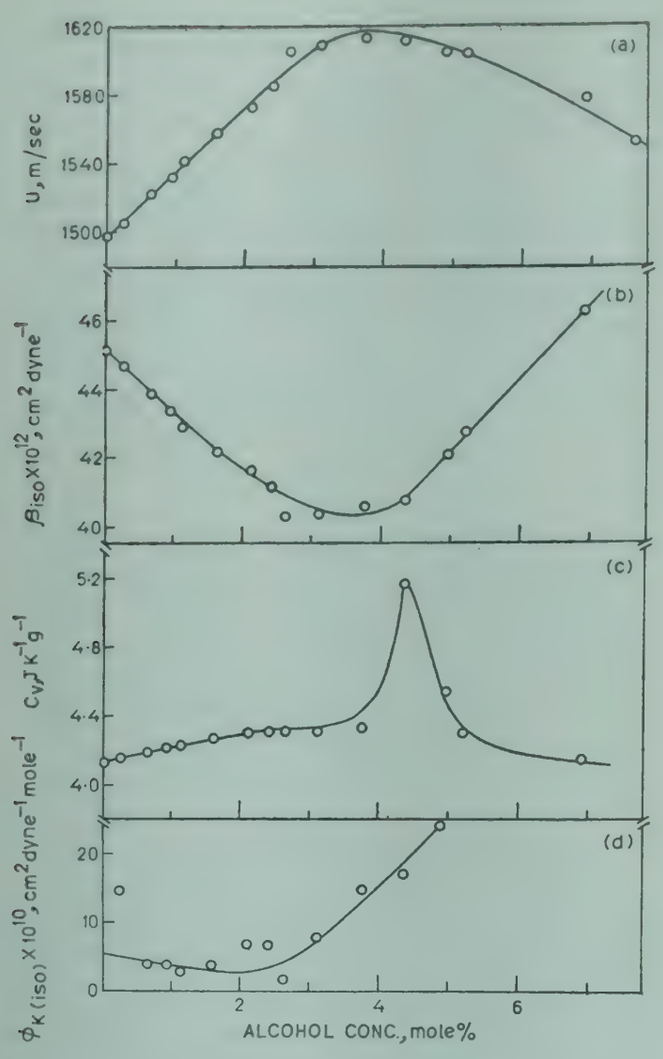

Fig. 1—Variation with conc. (of alcohol) of sound velocity (a) isothermal compressibility (b) specific heat at constant volume (c) and the apparent molal isothermal compressibility parameters (d) for *tert*-butyl alcohol-water mixtures at 25°C

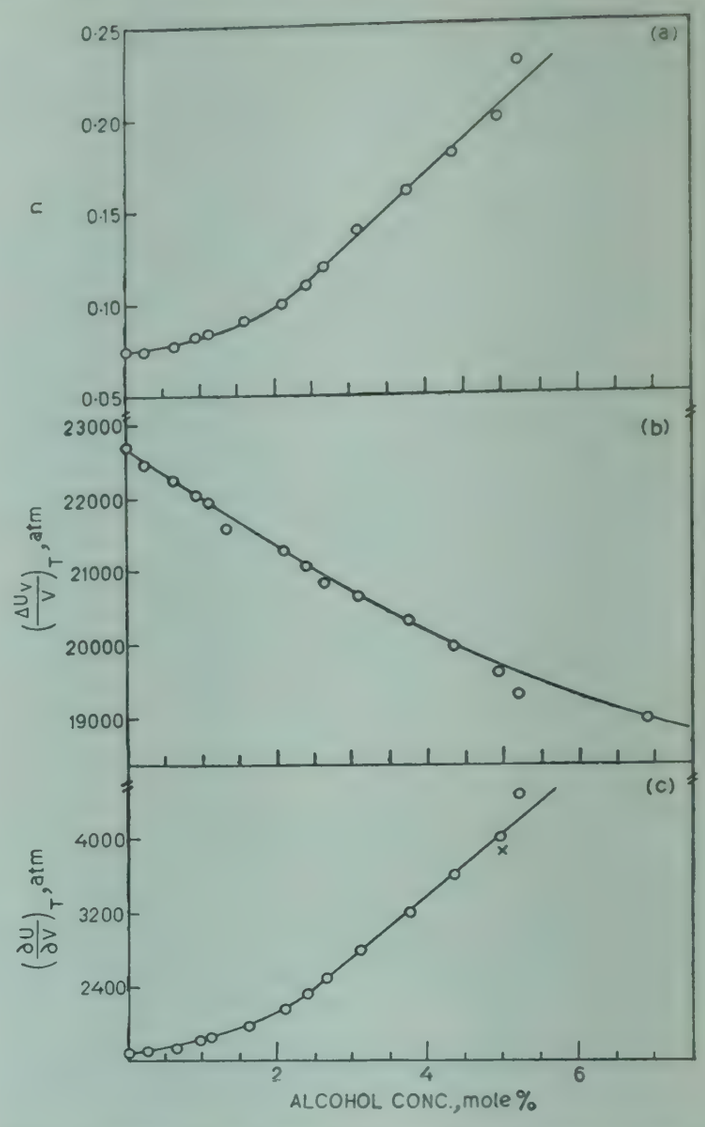

Fig. 2—Variation with conc. (of alcohol) of energy-volume coefficients (c), cohesive energy density (b) and n parameters (a) for *tert*-butyl alcohol-water mixtures at 25°C [The X point in (c) is from the data of Macdonald and Hyne.[15]]

dyne^{-1} at 25°C and where it exceeds this value, there is a sudden rise in ϕ_K curve with concentration. The extrapolation of ϕ_K to infinitely dilute concentrations leeds to ϕ_K^0 value of $5{\cdot}5 \times 10^{-10}$ cm^2 dyne^{-1} which represents the effect of solute-solvent interactions. For hydrophobic solutes (like tetra-butyl ammonium bromide) ϕ_K^0 values are negative,[18] and for methanol and ethanol they are more positive[19] ($>8 \times 10^{-10}$ cm^2 dyne^{-1}) while our value of ϕ_K^0 indicates comparatively less disturbance to water structure as such.

Observation of Fig. 2 indicates that for the internal pressure $(\partial U/\partial V)_T$ and n parameters there are inflections at about 2·6-3 mole% of alcohol again, while the cohesive energy $(\Delta U_V/V)_T$ decreases monotonously with concentration. Although the variation of these properties with concentration for the same system has been reported by Macdonald and Hyne,[15] the lowest concentration used in their studies is 5 mole% of alcohol. They have observed a maximum in $(\partial U/\partial V)_T$ and inflection for n at about 10 mole% of alcohol indicating a maximum solute-solvent interaction (hydrogen bonding). The concentration of 10 mole% of alcohol has also been characterized for maximum in ultrasonic absorption[20] and heat of mixing.[1] Thus, it appears that there are two effects at work in 0 to 10 mole% concentration of alcohol as already suggested by many workers. Our data suggest that in the lower concentration region both $(\partial U/\partial V)_T$ and n are comparatively less sensitive to solute-solvent and solute-solute interactions while after 2·6 mole% of alcohol, these parameters may be governed by the interaction between the —OH group of alcohol and water. The insensitivity of ultrasonic absorption observed by Blandamer *et al.*[20] in the lower concentration region probably can be explained in terms of comparative insensitivity of internal pressure and the maximum for absorption in terms maximum internal pressure. The monotonous

decrease in cohesive energy indicates overall decrease in hydrogen bonding in solvent-water.

Finally, it can be argued that since internal energy and volume are sensitive to intermolecular interactions, one can observe the corresponding subtle structural effect for various properties reflecting changes in the structure and state of intercomponent interaction present in aqueous mixtures.

Acknowledgement

The authors are thankful to Prof. V V Deshpande for his encouragement during this study.

References

1. Franks F & Ives D J G, *Quart. Rev. Chem. Soc.*, **20** (1966), 1.
2. Franks F, *Water, a comprehensive treatise*, Vol. 2 (Plenum Press, New York), 1973, Ch. 1 & 5.
3. Franks F & Watson B, *Trans. Faraday Soc.*, **63** (1967), 329.
4. Kaulgud M V & Patil K J, *J. phys. Chem.*, **78** (1974), 714.
5. Kaulgud M V & Patil K J, *J. phys. Chem.*, **80** (1976), 138.
6. Franks F, in *Physico-chemical processes in mixed aqueous Solvents*, edited by F Franks (American Elsevier, New York), 1967.
7. Kaulgud M V & Patil K J, (unpublished observations).
8. Blandamer M J & Waddington D, *J. phys. Chem.*, **74** (1970), 2569.
9. Burton C J, *J acoust. Soc. Am.*, 20 (1948), 186.
10. Avedikin L, Perron G & Desnoyers J E, *J. Soln Chem.*, **4** (1975), 331.
11. Neal J L & Goring D A I, *J. phys. Chem.*, **74** (1970), 658.
12. Franks F & Smith H T, *Trans. Faraday Soc.*, **64** (1968), 2962.
13. Greenspan M & Tschiegg C E, *J. Res. natn. Bur. Std*, 59 (1957), 249.
14. Hildebrand J H & Scott R L, *The solubility of non-electrolytes*, (Dover Pub. London), 1964.
15. Macdonald D D & Hyne J B, *Can. J. Chem.*, **49** (1971), 2636.
16. Nakanishi K, Kato N & Maruyama M, *J. Phys. Chem.*, 71 (1967), 814.
17. Glew D N, Mak H D & Rath N S, in *Hydrogen-bonded solvent systems*, edited by A K Covington & P Jones (Taylor and Francis, London), 1968.
18. Conway B E & Verrall R E, *J. Phys. Chem.*, 70 (1966), 3952.
19. Nakajima T, Komatsu T & Nakagawa T, *Bull. Chem. Soc. Japan*, **48** (1975), 783.
20. Blandamer M J, Clarke D E, Hidden N J & Symones M C R, *Trans. Faraday Soc.*, **64** (1968), 2691.

Note Added in the Proof

It was found that in Fig. 1 (c), the values of C_v are in error in the higher concentration region due to an error in extrapolation of C_p values. However, the values reported in Table 1 are the corrected values after proper extrapolation which do not affect the conclusions drawn in the text. The authors regret the mistake made in Fig. 1 (c).

Indian Journal of Pure & Applied Physics
Vol. 18, July 1980, pp. 504-509

Charge Transfer Interaction of Some Biomolecules with Chloranil

R SAHAI* & V SINGH

Department of Chemistry, V S S D College, Kanpur University, Kanpur 208 002

Received 26 *December* 1978; *revised received* 5 *December* 1979

Refractometric, differential refractometric and conductometric techniques have been used to investigate the charge-transfer interaction of some biomolecules (e.g. tryptophan, tyrosin and phenylalanine) with chloranil. The equilibrium constant (K_1) and thermodynamic parameters determined by these techniques were found to be in good agreement with the spectrophotometric values. Titration technique from these methods have indicated 1:1 stoichiometry of these complexes. Enthalpy (ΔH) and entropy (ΔS) of these complexes were found to be of the order of 5·5-7·5 kcal/mole and 16-18 eu respectively. The values of electronic polarization (α) have been discussed in terms of electronic polarizability and their use in the evaluation of the dipole moment has been explored.

1. Introduction

The stability of molecular complexes which mainly occurs through interaction between electron donor and acceptor may play an essential role in understanding several fundamental mechanisms involved in the chemical initiation of some vital diseases in biological systems,[1-5] the conformation of proteins and nucleic acids,[6,7] the role of drug interactions,[8] the mechanism of toxicity[9,10] as well as carcinogenecity[11-18] of pesticides. This initiated us to study the role of molecular complexes in the chemical initiation of cancer. In order to investigate at the molecular level the charge-transfer complexation process involved in carcinogenesis, the interaction between some biomolecules (e.g. tryptophan, tyrosin and phenylalanine) and chloranil has been studied in 50% aqueous ethanol using refractometric, differential refractometric and electrical conductance techniques. Tryptophan, tyrosin and phenylalanine have been chosen as donors because they are the basic components of proteins. Chloranil has been taken as acceptor because of its significance in several biological systems.[4]

2. Experimental Details and Data Analysis

Tryptophan, tyrosin and phenylalanine were obtained from Fluka AG and have been used without further purification. Ethanol was used after distilling thrice. AnalaR grade chloranil supplied from E. Merck, was recrystallized from its standard solution in benzene.

Stock solutions of donors (tryptophan, tyrosin and phenylalanine) and acceptor (chloranil) were prepared by weighing in an analytical balance and then diluted to the required volume in volumetric flasks in 50% aqueous ethanol. The solutions employed for conductometric and refractometric measurements were prepared from the stock solution by pipetting the calculated volumes into 10 ml volumetric flasks and then diluted subsequently with the same solvent. All the stock solutions were made on the day of measurements.

The electrical conductance has been measured by Philips PR 9500 conductivity bridge and a conductivity cell (immersion of dip type) having cell constant 0·950. All the measurements were made at 50Hz and at different temperatures. Conductance cell was standardized each day with $N/50$ solution of chemically pure KCl using Lind, Zwolenik and Fuoss[19] constants. The concentration of acceptor was kept constant throughout the study and the concentration of donors was varied.

The refractive indices have been measured by Bausch and Lomb refractometer with an accuracy of $\pm$ 0·0002. All the measurements were made at 35 $\pm$ 0·1°C. The refractive indices were measured for three sets of solutions as follows:

(a) In the first set, the refractive indices of donor solutions (n_D) were measured. (b) In the second set the refractive indices of acceptor solution (n_A) were noted. (c) In the third set, the refractive indices of mixed solution (donor + acceptor) were measured.

The equilibrium constant (K_1) at different temperatures by electrical conductance method[20] has been

*To whom all correspondence should be addressed

calculated using the relation

$$\Lambda/C_D^0 = \left\{ K_1 C_A^0 \Big/ \rho \left(1 + K_1 C_A^0 \right) \right\} - \left\{ K_1 \Lambda \Big/ \left(1 + K_1 C_A^0 \right)^2 \right\} \quad ...(1)$$

where C_A^0 and C_D^0 represent the initial concentration of acceptor A and donor D, respectively and ρ is the extent of polarization. Thus a plot of Λ versus Λ/C_D^0 gives a straight line with a slope $-\{K_1/(1 + K_1 C_A^0)^2\}$ and intercept $K_1 C_A^0/\rho\ (1 + K_1 C_A^0)$. Representative plots are shown in Fig. 1.

The equlibrium constant (K_1) and extent of electronic polarization (α) at 35°C by refractometric[21] and differential refractometric[22,23] methods have been calculated by using the equations developed by Sahai *et al*:[21-23]

$$\delta\phi/C_D^0 = \left\{ K_1 C_A^0 \Big/ \alpha \left(1 + K_1 C_A^0 \right) \right\} - \left\{ K_1 \delta\phi \Big/ \left(1 + K_1 C_A^0 \right)^2 \right\} \quad ...(2)$$

$$\Delta\phi/C_D^0 = \left\{ K_1 C_A^0 \Big/ \alpha \left(1 + K_1 C_A^0 \right) \right\} - \left\{ K_1 \Delta\phi \Big/ \left(1 + K_1 C_A^0 \right)^2 \right\} \quad ...(3)$$

$$\Delta\Omega C_{DA}/C_D^0 = \left\{ K_1 C_A^0 \Big/ \alpha \left(1 + K_1 C_A^0 \right) \right\} - \left\{ K_1 \Delta\Omega C_{DA} \Big/ \left(1 + K_1 C_A^0 \right)^2 \right\} \quad ...(4)$$

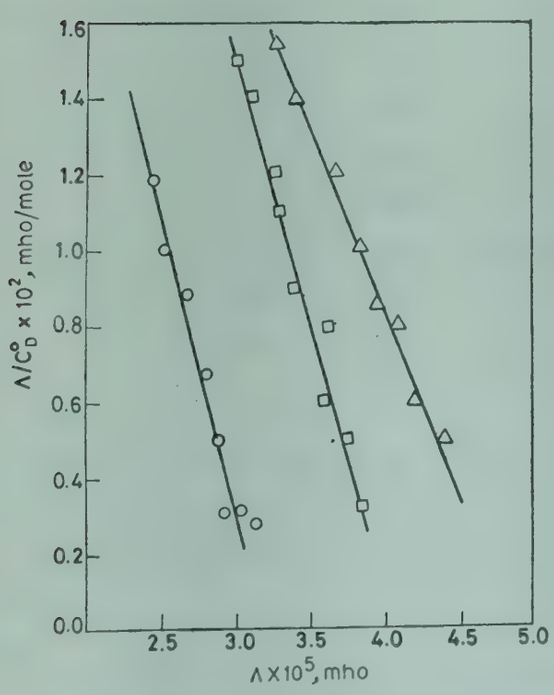

Fig. 1—Plot of Λ versus Λ/C_D^0 for tryptophan-chloranil complex in 50% aqueous ethanol at different temperatures

where α is the extent of electronic polarization, and $\delta\phi$, $\Delta\phi$ and $\Delta\Omega C_{DA}$ may be calculated by the relations,

$$\delta\phi = 10^3 (\phi - \phi_0) = 6000\ (n - n_0)\, n_0/(n_0^2 + 2)^2 \quad ...(5)$$

$$\Delta\phi = 10^3 (\phi - \phi_A) = 6000\ (n - n_A)\, n_A/(n_A + 2)^2 \quad ...(6)$$

$$\Delta\Omega C_{DA} = 10^3 (\phi - \phi_D) - (\phi_A - \phi_0) = \{6000\ (n - n_D)\, n_D/(n_D^2 + 2)^2\} - \{6000\ (n_A - n_0)\, n_0/(n_0^2 + 2)^2\} \quad ...(7)$$

where n, n_D, n_A and n_0 are the refractive indices of solution (donor + acceptor), donor, acceptor and solvent respectively, ϕ, ϕ_D, ϕ_A and ϕ_0 are the refraction/cm³ due to solution, donor, acceptor and solvent respectively and may be calculated as reported earlier.[21] As expected from Eqs. (2)-(4), the plots of $\delta\phi$ versus $\delta\phi/C_D^0$, $\Delta\phi$ versus $\Delta\phi C_D^0$ and $\Delta\Omega C_{DA}$ versus $\Delta\Omega C_{DA}/C_D^0$ were linear with a slope $-\{K_1 C_A^0/(1+K_1 C_A^0)^2\}$ and intercept $K_1 C_A^0/\alpha\ (1+K_1 C_A^0)$. Representative plot of $\Delta\Omega C_{DA}$ versus $\Delta\Omega C_{DA}/C_D^0$ are shown in Fig. 2. Refractometric, differential refractometric and conductometric titration techniques indicating 1 : 1 stoichiometry of these complexes are shown in Figs. 3 and 4. The equilibrium constant have also been calculated by using the Yoshida and Osawa's equation,[24] viz.

$$K_1 = 2\sqrt{k}\,\{\sqrt{k}\,(C+C') - (C+kC')\}/(C-kC')^2 \quad ...(8)$$

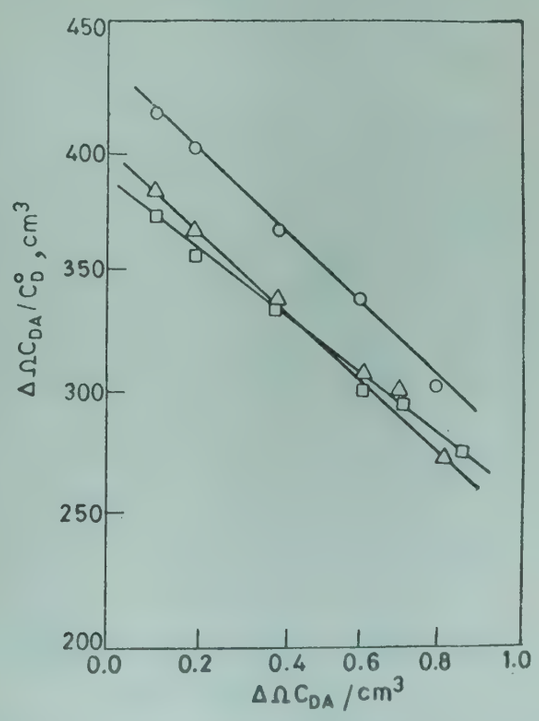

Fig. 2—Plots of $\Delta\Omega C_{DA}$ versus $\Delta\Omega C_{DA}/C_D^0$ for tryptophan-chloranil (○—○—○), tyrosin-chloranil (△—△—△) and phenylalanine-chloranil (□—□—□) complexes in 50% aqueous ethanol at 35°C

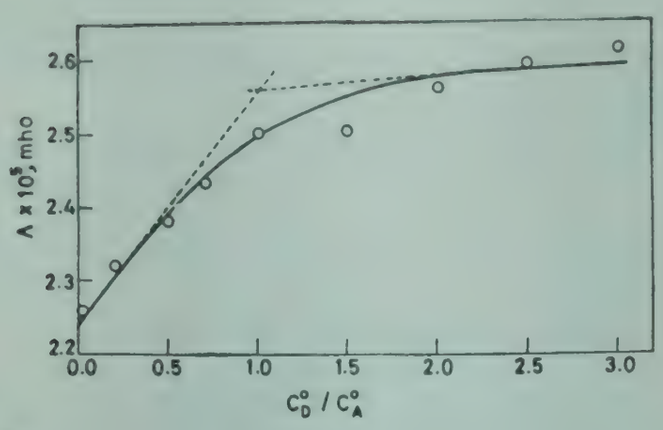

Fig. 3—Molar ratio plot for the tryptophan-chloranil complex in 50% aqueous at 30°C determined by electrical conductance method

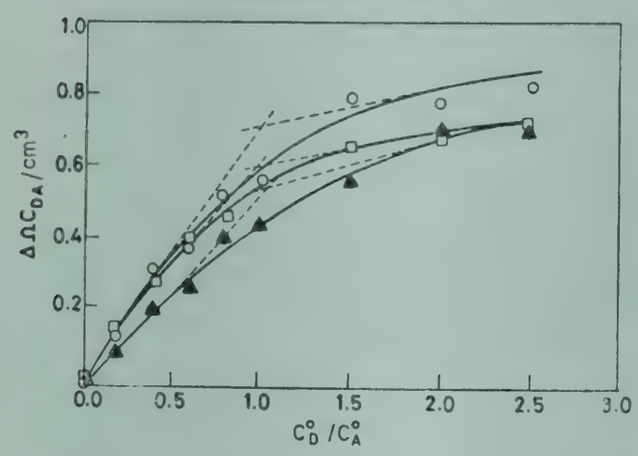

Fig. 4—Molar ratio plots for the tryptophan-chloranil (▲—▲—▲), tyrosin-chloranil (○—○—○) and phenylalanine-chloranil (□—□—□) complexes in 50% aqueous ethanol at 35°C determined by differential refractometric method

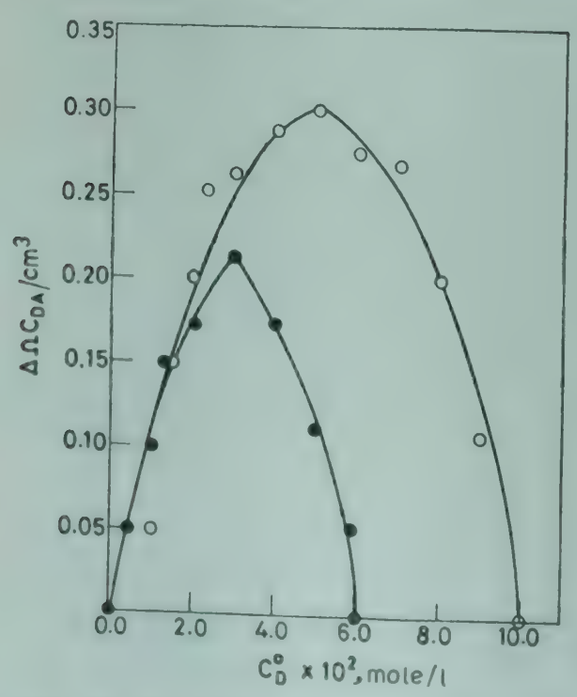

Fig. 5—A plot of refraction/cm³ due to charge-transfer $\Delta\Omega C_{DA}$ versus molar ratio of solutes indicating 1:1 stoichiometry of tryptophan-chloranil complex in 50% aqueous ethanol at 35°C

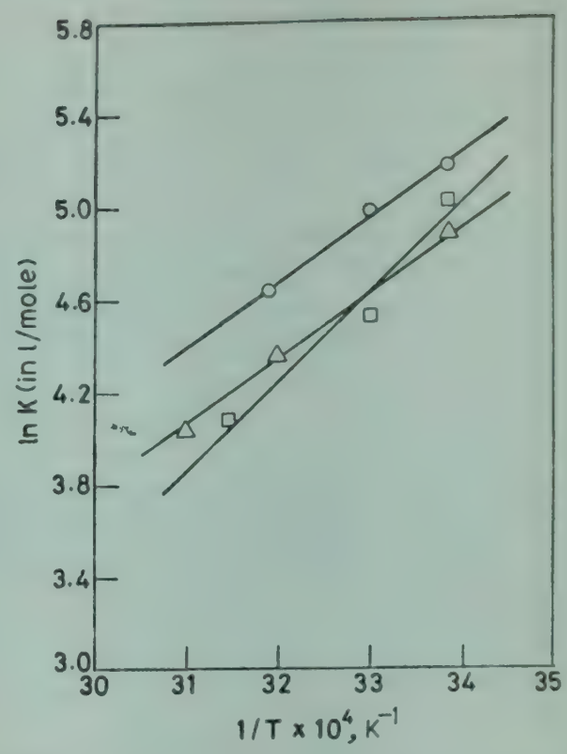

Fig. 6—Plots of ln K versus $1/T$ for the complex formation between chloranil with tryptophan (○—○—○), tyrosin (□—□—□) and phenylalanine (△—△—△)

Table 1—Thermodynamic Parameters and Equilibrium Constants for Complex Formation Determined from Electrical Conductance Measurements at Different Temperatures

Donor	$1/T\times10^4$	K_1 (l.mole^{-1})	ΔH (kcal/mole)	ΔS eu
Tryptophan	33·89	177·77 ± 5·5	5·5	18·98
	33·00	148·14 ± 4·0		
	31·94	104·10 ± 4·5		
Tyrosin	33·89	150·37 ± 4·5	7·5	16·02
	33·00	92·37 ± 3·5		
	31·44	60·06 ± 3·5		
Phenylalanine	33·89	133·33 ± 4·5	5·32	17·41
	32·00	80·00 ± 3·0		
	31·00	57·14 ± 2·5		

where C and C' are the maximum concentrations of both the systems and k is the maximum deviation from the additive line when molar ratio is plotted against square of the refractive index (n^2). The equilibrium constant (K_1) has also been calculated by modified Yoshida and Osawa's method as suggested by Sahai and Singh[25] in which instead of a plot of n^2 versus molar ratio of solutes, the $\Delta\Omega C_{DA}$ [the refraction/cm³ due to charge-transfer complex calculated

Table 2—Equilibrium Constant (K_1) and Extent of Electronic Polarization (α) Data for 1 : 1 Molecular Complexes of Some Aromatic Amino Acids with Chloranil in 50% Aqueous Ethanol at 35°C

Complex	Equilibrium constant (K_1), l.mole^{-1} Refractometric method					Spectrophotometric method		$\alpha \times 10^5$ from		
	From Eq. (2)	From Eq. (3)	From Eq. (4)	From the plot of n^2 versus molar ratio of solutes	From the plot of $\Delta\Omega C_{DA}$ versus molar ratio of solutes	K_1	T °C	Eq. (2)	Eq. (3)	Eq. (4)
Tryptophan-chloranil	221·23±5·2	208·33±5·0	156·25±2·5	208·00±10·5	157·54±5·5	176·00[26]	20	5·05	4·63	3·58
Tyrosin-chloranil	166·66±5·0	172·41±4·5	142·85±2·0	191·30± 8·5	140·72±4·0			3·93	3·98	3·52
Phenylalanine-chloranil	151·51±3·5	166·66±5·0	131·57±2·0	157·54± 5·0	127·16±2·5			3·81	4·09	2·97

from Eq. (7)] is plotted against molar ratio of solutes. A representative plot of $\Delta\Omega C_{DA}$ versus molar ratio of solutes indicating 1 : 1 stoichiometry of the complex is shown in Fig. 5.

A plot of ln K against $1/T$ gave a good straight line (Fig. 6). The heat of formation (ΔH) and the entropy change (ΔS) for the complexation were obtained from the slope of the straight line and its intersection with ordinate respectively. These values are given in Table 1. The standard deviations given in Tables 1 and 2 have been calculated by using regression analysis.

3. Results and Discussion

Tryptophan, tyrosin and phenylalanine have shown very little conductance in 50% aqueous ethanol. Also a solution of chloranil has a very low conductance value. On mixing a solution of aromatic amino acid in 50% aqueous ethanol with a solution of chloranil in the same solvent, an appreciable increase in conductance was noticed. Similarly in refractometric measurements, an appreciable increase in refractive index was noticed with increase of donor concentration. There may be doubt that this relative increase in refractive index may be due to the donor concentration and not due to the charge-transfer interaction. This problem has been solved by taking the refractive index of donor and acceptor separately. On mixing equal amounts of donor and acceptor solutions, the refractive index increases appreciably more than that of the maximum value of separate components. This appreciable increase in refractive index is due to the charge-transfer interaction and not due to the donor concentration. Thus this relative increase in both conductance and refractive index of solution may be interpreted due to the charge-transfer from lone pair (n) of amino group (—NH_2) of aromatic amino acid to π^*-orbital of chloranil†.

The refractive index of donor as well as that of chloranil in 50% aqueous ethanol increases with concentration. The plot of Δn, the difference in refractive indices of calculated and observed values, against that of the complex is linear indicating that there is no interaction between the complex and individual species. A change in electron cloud density in the neutral atom or molecule will lead to a change in the polarizability. Since the complex is generally more polar than the components, the electronic polarizability or refractive index increases and the deviation depends upon the extent of interaction between the donor and acceptor. Therefore, the stronger the complex, the larger is the deviation in the refractive index value. In the present cases, the deviation is positive and maximum is observed at 1 : 1 molar ratio. Because of the limited accuracy of the Bausch and Lomb refractometer, it was necessary to raise the concentration of the solute to $10^{-2}M$ in order to get the variation at the 4th place of the decimal. At this large concentration, however, the data obtained are less reliable because of the self-association of solutes.[24]

†Spectrophotometric[26] results have indicated that the donation is taking place from the lone pair of amino group and not from the π-orbital of the benzene nucleus. But above techniques can only provide the information regarding the charge-transfer, not the probable site of donation. On the basis of equilibrium constant data one may simply propose the probable site of interaction.

The equilibrium constant data obtained by refractometric and conductometric methods are listed in Tables 1 and 2 respectively and are in good agreement with those of spectrophotometric method. From Table 1, it is clear that K_1 obtained from Eq. (2) is not so reliable as those obtained from Eqs. (3) and (4). From Eq. (4), in which the refraction/cm^3 due to charge-transfer complex has been taken into account, the values of K_1 obtained are the best. From this it is clear that the solvent itself contributes little to equilibrium constant by acting either as electron donor or as electron acceptor. This is in agreement with the observations from spectrophotometric investigations, in which water[27] and ethanol[28] have been reported to be the electron donor*. From the equilibrium constant data it is clear that the interaction is stronger in case of tryptophan than in cases of tyrosin and phenylalanine. Also tyrosin shows stronger interaction than phenylalanine. From theoretical calculation of Pullman[29] it is also evident that tryptophan having an indole nucleus should behave as a better electron donor.

The dipole moment of the complex always depends upon the total polarizability of the complex. But in calculation of dipole moment of the complex so far, the electronic polarizability is neglected on the ground that the electronic polarizability of the complex is equal to the sum of the electronic polarizabilities of individual molecules.[30-33] But from the electronic polarizability data (Table 2) and from Fig. 6 it is clear that as soon as the complex formation takes place, the electronic polarizability increases over that of the additive values and is linear with the equilibrium constant of the complex. So if one wants to get the exact value of dipole moment of the complex, the electronic polarizability should not be neglected.

The present investigation is in support of the view of the recently developed "Electronic theory of cancer" proposed by Szent-Gyorgyi[34] and also the theme of his paper, "Protein, Regulation and Cancer"[5] in which he has proposed that the life is based on the two miracles. Miracle one was the creation and folding of the protein molecule. Miracle two was the transformation of this molecule into a highly reactive radical. The cancer cell seems to be unable to perform miracle two. On the basis of our present investigation it seems that miracle two is not performed by the cell due to the charge-transfer complexation of protein with the carcinogen.

*Here we should give the importance of this technique. Now-a-days spectrophotometric method has extensively been used to study these molecular complexation, but this technique is unable to give appropriate results where there is a slight perturbation of either donor or acceptor absorption bands due to the weak interactions. In such cases neither we can get correct stoichiometry of the complex formed nor the accurate values of equlibrium constants and absorption coefficient. Also, in that case one cannot get the absorption bands, where solvent itself absorbs more than that of donor or acceptor. This difficulty has been overcome in refractometric technique by employing the technique mentioned in the present investigation.

Acknowledgement

Authors are grateful to Prof. P P Singh (M L K College, Balrampur) and Prof. P C Nigam (Indian Institute of Technology, Kanpur) for providing electrical conductance and refractometric facilities. They are also grateful to Prof P R Singh (I I T, Kanpur) for constant encouragement during the progress of this work. One of us (VS) wishes to thank the University Grants Commission for providing with a fellowship.

References

1. Szent-Gyorgyi A, *Electronic biology and cancer*, (M Dekker, New York), 1976.
2. Szent-Gyorgyi A, *The living state with an observation on cancer*, (Academic Press, New York), 1972.
3. Szent-Gyorgyi A, *Introduction to a submolecular biology*, (Academic Press, New York), 1960.
4. Slifkin M A, *Charge transfer interaction of biomolecules*, (Academic Press, New York), 1971.
5. Szent-Gyorgyi A, *Int. J. quant. Chem.: Quant. Biol. Symp.*, 4 (1977), 179.
6. Qkamote Y & Brenner W, *Organic semi-conductors*, (Reinhold, London), 1964, Ch. 8, 159-170.
7. Foster R, *Organic charge transfer complexes* (Academic Press, New York), 1969, Ch. 12, 335-373.
8. Weinstein H & Osman R, *Int. J. quant. Chem.: Quant. Biol. Symp.*, 4 (1977), 353.
9. Sahai R, *Indian J. Chem.*, 15A (1977), 236.
10. Matsumura F & O'Brein R D, *J. Agr. Food. Chem.*, 14 (1966), 38.
11. Thomas J H, *Int. J. Environ. Stud.*, 1 (1970), 43.
12. Agthe C, Garcia H, Shubik P, Tomaltis L & Charles E M W, *Proc. Soc. exp. Biol. Med.*, 134 (1970), 113.
13. Durhan W F, *J. Dairy Sci.*, 54 (1971), 701.
14. Kraybill H F, *Pest. Control*, 43 (1975), 10.
15. Kilgore W W & Li M Y, *Residue Rev.*, 4 (1973), 141.
16. Terricini B, *Oncol. Proc. 10th int. Cancer Congr.*, 1970, 5 (1971), 250.
17. Habermann R T & Fitzhugh O G, *Toxicol. appl. Pharmacol.*, 20 (1971), 122.
18. Durham W F & Williams C H, *Ann. Rev. Entomol.*, 17 (1972), 123.
19. Lind J E & Fuoss R M, *J. phys. Chem.*, 65 (1961), 999.
20. Badoni V N, *Studies on the molecular complexes in metal acetylacetonates*, Ph D thesis, Kanpur University, Kanpur, 1978.

21. Sahai R, Pande P C & Singh V, *Indian J. Chem.*, **18A** (1979), 217.
22. Sahai R & Singh V, Paper accepted for the presentation at 67th Session of Science Congress, held at Calcutta during February 3-7, 1980.
23. Sahai R & Singh V, *J. Solution Chem.*, (1980), in press.
24. Yoshida Z & Osawa E, *Bull. chem. Soc. Japan*, **38** (1965), 140.
25. Sahai R & Singh V, *Bull. chem. Soc. Japan*, in press.
26. Birks J B & Slifkin M A, *Nature Lond.*, **197** (1963), 42.
27. Bhowmik B B & Chattopadhyay S P, *Indian J. Chem.*, **17A** (1979), 85.
28. Slifkin M A, *Spectrochim. Acta*, **20** (1965), 1543.
29. Pullman B & Pullman A, *Proc. natn. Acad. Sci. USA*, **44** (1958), 1197.
30. Singh R A & Bhat S N, *J. phys. Chem.*, **82** (1978), 2323.
31. Singh R A & Bhat S N, *Indian J. Chem.*, **16A** (1977), 1106.
32. Foster R & Kulevsky N, *J. chem. Soc. Faraday Trans.*, **69** (1973), 1427.
33. Kulevsky N, *Molecular association*, Vol. I, edited by R Foster (Academic Press, New York), 1975.
34. Szent-Gyorgyi A, *Int. J. quant. Chem. : Quant. Biol. Symp.*, **3** (1976), 45.

Indian Journal of Pure & Applied Physics
Vol. 18, July 1980, pp. 510-515

Cationic Effect on the Intramolecular Forces of $B^{VI}O_6$ Octahedra in Ordered Cubic Perovskites $A_2B^{II}B^{VI}O_6$*

A N Pandey & U P Verma

Molecular Spectroscopy Research Laboratory, Department of Physics, Meerut College, Meerut 250 001

&

J R Chopra

Department of Physics, Lajpatrai College, Sahibabad (Ghaziabad)

Received 15 *March* 1979

The influence of A and B^{II} cations in the ordered cubic perovskites of the type $A_2B^{II}B^{VI}O_6$ (B^{VI}=Mo, W, U, Te; A = large cation such as Ba; B^{II} = a smaller cation such as Ni, Co, Mg, Zn,...) has been recognized on the intramolecular forces in $B^{VI}O_6$ octahedron on the basis of their infrared and Raman spectra. The stretching force constant, $f_{B^{VI}-O}$ in $B^{VI}O_6$ octahedra (B^{VI} = Mo and W) possessing the same cation A but different cation B^{II} (given in parentheses) varies in the order f_{B-O} (Zn) < f_{B-O} (Mg) < f_{B-O} (Ca) < f_{B-O} (Cd). In the case of tellurates A_2MgTeO_6 (A = Sr, Ba or Pb), the stretching force constant f_{Te-O} follows the trend f_{Te-O} (Ba_2) < f_{Te-O} (Pb Ba) < f_{Te-O} ($Pb_{1\cdot5}$-$Ba_{0\cdot5}$) < f_{Te-O} (Pb_2) and f_{Te-O} (Sr_2) > f_{Te-O} (Sr Ba) > f_{Te-O} (Ba_2). The trend is interpreted on the basis of mass effect. Moreover, the Raman-active, fundamental frequency ν_2 (E_g), unobserved in most of the cases, has been predicted on the basis of our results. For those cases where this fundamental is experimentally observed, the root-mean square deviation between observed and calculated values comes out to be 4·5 cm^{-1} and the overall per cent deviation is 0·1.

1. Introduction

Liegeois-Duyckaerts and Tarte[1] have studied the infrared and Raman spectra of a number of ordered cubic perovskites of the type $A_2B^{II}B^{VI}O_6$ and reported the wavenumbers of most of the bands, predicted by a group theoretical analysis. They also categorized the observed wavenumbers into internal and external modes and interpreted the internal modes on the basis of octahedral symmetry. A survey of the vibrational wavenumbers corresponding to the internal modes reveals that these are influenced by A and B^{II} cations. Therefore, it is interesting to study the influence of these cations on intramolecular forces of $B^{VI}O_6$ octahedron, which in turn help us in understanding the bonding properties of these ions. Moreover, the Raman-active fundamental $\nu_2(E_g)$ has not been reported earlier in most of the cases. Therefore, an attempt has also been made to predict these fundamentals.

2. Method of Computation

In order to study the intramolecular forces we have selected the general valence force field (GVFF) and modified the Urey-Bradley force field (MUBFF) models and followed the Wilson's *FG* matrix method.[2] The second order secular equation occurring in F_{2u} species has been solved by *L-F* approximation method[3] and the *G* matrices are taken from Cyvin.[4] One of the important bond properties such as bond order has been obtained from the relations, given by Siebert[5]

$$N = 0{\cdot}69 \frac{}{f_{MO}} + 0{\cdot}37 \text{ if } \frac{f_r}{f_{MO}} > 1{\cdot}5$$

$$\text{otherwise } N = \frac{f_r}{f_{MO}} \qquad \ldots(1)$$

where, M is for B^{VI} metal, f_r, the M—O stretching force constant and f_{MO}, covalent bonding force constant (both in 10^2 Nm^{-1}) given by the relation

$$f_{MO} = 7{\cdot}2\, Z_M Z_O / n_M^3 n_O^3$$

where Z_M and Z_O are atomic numbers and n_M and n_O the principal quantum numbers of valence electrons for M and O atoms, respectively.

3. Results and Discussion

The observed wavenumbers which are used in the present study are given in Table 1. In order to predict the unobserved fundamental ν_2 (E_g), we have first computed the stretch-stretch interaction force constants f_{rr} and f'_{rr} in cases where allowed fundamental frequencies are observed. The results are listed in Table 2 along with their ratio f'_{rr}/f_{rr}. It is apparent from Table 2 that this ratio is greater than unity in case of oxyanions of transition elements

*Presented at the National Seminar on Molecular Spectroscopy and Lasers held at the Banaras Hindu University, Varanasi, during Jan. 29-31, 1979.

while in case of oxyanions of non-transition elements it is less than unity. Such observations have also been made by previous workers.[6,7] Further, it is notable that this ratio is approximately equal for $Mo^{VI}O_6$ and $W^{VI}O_6$ octahedra and the same is true in case of $Te^{VI}O_6$ octahedra in different complexes.

Employing the mean value of the ratio f'_{rr}/f_{rr} and assuming, to a first approximation, that stretch-stretch interactions are of similar nature in different ordered complex perovskites, the unobserved fundamental $\nu_2(E_g)$ has been calculated. The overall percentage deviation between observed and calculated values of the $\nu_2(E_g)$ fundamental for $Mo^{VI}O_6$ and $W^{VI}O_6$ octahedron comes out to be 0·1 and the root-mean square deviation is 7·5 cm^{-1}. For $Te^{VI}O_6$ octahedra, the percentage deviation between observed and calculated values of the same fundamental is 0·003 and the root-mean square deviation is 2·3 cm^{-1}. From this it is evident that the computed values

Table 1—Vibrational Wavenumbers (in cm^{-1}) of $B^{VI}O_6$ Octahedra in Some Ordered Cubic Perovskites $A_2B^{II}B^{VI}O_6$

Complex	ν_1	ν_2	ν_3	ν_4	ν_5	ν_6
Ba_2ZnMoO_6	785	(634·5)	594	385	428	303
Ba_2MgMoO_6	779	(636·6)	605	387	438	310
Ba_2CaMoO_6	802	650 (646·0)	603	360	407	288
Ba_2CdMoO_6	808	(654·0)	615	350	401	284
Ba_2ZnWO_6	822	(671·7)	605	357	431	305
Ba_2MgWO_6	813	674 (673·9)	618	381	441	312
Ba_2CaWO_6	838	675 (686·1)	620	338	413	292
Ba_2CdWO_6	845	(689·3)	620	340	405	286
Ba_2NiWO_6	816	(671·4)	610	382	434	307
(BaSr) $MgWO_6$	847	(707·8)	656	380	446	315
(BaSr) $CaWO_6$	828	(678·6)	614	343	423	299
Ba_2MgTeO_6	724	(543·9)	650	410	414	293
Ba_2CaTeO_6	748	(571·6)	680	402	402	284
Ba_2CdTeO_6	745	557 (556·6)	667	392	385	272
Pb_2MgTeO_6	761	572 (572·3)	685	373	359	254
$(Pb_{1\cdot5}Ba_{0\cdot5})$ $MgTeO_6$	753	564 (563·6)	675	395	364	257
(PbBa) $MgTeO_6$	742	(556·9)	666	409	364	257
$(Pb_{1\cdot5}Sr_{0\cdot5})$ $MeTeO_6$	766	580 (580·9)	693	395	362	256
(PbSr) $MgTeO_6$	775	(586·3)	700	402	366	259
(BaSr) $MgTeO_6$	758	(586·5)	695	410	420	297
Sr_2MgTeO_6	782	(602·4)	715	413	431	305
(BaLa) $LiTeO_6$	716	(579·3)	675	417	428	303
(BaLa) $NaTeO_6$	742	(579·3)	666	409	364	257
Ba_2MgUO_6	753	(573·3)	604	341	352	249
Ba_2ZnUO_6	762	(568·6)	600	310	348	246
Ba_2NiUO_6	743	(563·7)	595	315	350	247
Li_6ReO_6	680	505	620	425	360	255
$Sr_5(ReO_6)_2$	685	565	628	365	335	237
$Sr_4Ca(ReO_6)_2$	685	585	628	365	340	240

Values given in parentheses are the calculated frequencies

Table 2—Stretch-Stretch Interaction Constants of a Few $B^{VI}O_6$ Octahedra and Their Ratio (in 10^2 Nm^{-1})

Complex	f_{rr}	f'_{rr}	f'_{rr}/f_{rr}	av. f'_{rr}/f_{rr}
Ba_2CaMoO_6	0·347	1·016	2·928	2·824
Ba_2MgWO_6	0·312	0·941	3·016	
Ba_2CaWO_6	0·387	0·978	2·527	
Ba_2CaTeO_6	0·377	0·154	0·408	0·367
$(Pb_{1\cdot5}Ba_{0\cdot5})$ $MgTeO_6$	0·389	0·146	0·375	
$(Pb_{1\cdot5}Sr_{0\cdot5})$ $MgTeO_6$	0·393	0·138	0·351	
Pb_2MgTeO_6	0·399	0·134	0·340	

of the $\nu_2(E_g)$ fundamental in other complexes are reasonable.

Once the unobserved fundamental frequency is known for the complexes presently under study we have computed the internal force constants in GVFF and MUBFF models for $B^{VI}O_6$ (B = Mo, W, Te) octahedra and the results are presented in Tables 3 and 4. As the results of the same octahedra in different complexes are now available it is interesting to study the cationic effect on the principal stretching force constants f_r of an octahedra. The influence of the nature of B^{II} cations, keeping the A cation fixed, on the stretching force constant of Mo—O bond is

Table 3—GVFF Force Constants (in 10^2 Nm^{-1}) and Bond Order (N) of B^{VI} – O Bond of Some $B^{VI}O_6$ Octahedra

Complex	f_r	f_{rr}	$f_{r\alpha}-f''_{r\alpha\alpha}$	$f_\alpha-f''''_{\alpha\alpha}$	$f_{\alpha\alpha}-f''_{\alpha\alpha}$	$f'_{\alpha\alpha}-f''''_{\alpha\alpha}$	N
La_2MgTiO_6	2·987	0·299	0·149	0·503	−0·028	−0·028	1·207
Ba_2ZnMoO_6	3·520	0·335	0·099	0·449	0·009	0·009	1·46
Ba_2MgMoO_6	3·561	0·317	0·100	0·462	0·005	0·005	1·47
Ba_2CaMoO_6	3·644	0·355	0·088	0·405	0·001	0·001	1·49
Ba_2CdMoO_6	3·742	0·354	0·084	0·382	0·001	0·001	1·52
Ba_2ZnWO_6	3·963	0·353	0·060	0·451	0·006	0·006	1·48
Ba_2MgWO_6	4·015	0·325	0·068	0·461	0·017	0·017	1·49
Ba_2CaWO_6	4·139	0·364	0·054	0·408	0·003	0·003	1·49
Ba_2CdWO_6	4·172	0·375	0·055	0·403	0·008	0·008	1·53
Ba_2NiWO_6	3·973	0·338	0·067	0·487	0·022	0·022	1·48
(BaSr) $MgWO_6$	4·445	0·339	0·068	0·497	0·014	0·014	1·61
(BaSr) $CaWO_6$	4·052	0·353	0·056	0·403	0·001	0·001	1·50
Ba_2MgTeO_6	3·377	0·359	0·097	0·485	0·040	0·040	1·13
Ba_2CaTeO_6	3·680	0·365	0·094	0·462	0·040	0·040	1·23
Ba_2CdTeO_6	3·552	0·385	0·090	0·433	0·042	0·042	1·19
Pb_2MgTeO_6	3·736	0·395	0·083	0·386	0·041	0·041	1·25
$(Pb_{1\cdot5}Ba_{0\cdot5})$ $MgTeO_6$	3·637	0·391	0·092	0·419	0·053	0·053	1·21
(PbBa) $MgTeO_6$	3·543	0·377	0·097	0·438	0·063	0·063	1·18
$(Pb_{1\cdot5}Sr_{0\cdot5})$ $MgTeO_6$	3·823	0·392	0·092	0·417	0·054	0·054	1·28
(PbSr) $MgTeO_6$	3·903	0·403	0·095	0·430	0·057	0·057	1·30
(SrBa) $MgTeO_6$	3·837	0·362	0·099	0·491	0·037	0·037	1·28
Sr_2MgTeO_6	4·061	0·390	0·100	0·506	0·034	0·034	1·36
(BaLa) $LiTeO_6$	3·620	0·278	0·112	0·508	0·038	0·038	1·21
(BaLa) $NaTeO_6$	3·620	0·278	0·098	0·500	0·032	0·032	1·21
Ba_2MgUO_6	3·432	0·334	0·046	0·367	0·038	0·038	1·60
Ba_2ZnUO_6	3·418	0·370	0·039	0·326	0·020	0·020	1·59
Ba_2NiUO_6	3·332	0·337	0·040	0·333	0·022	0·022	1·56
Li_6ReO_6	3·093	0·448	0·082	0·482	0·088	0·088	—
$Sr_5(ReO_6)_2$	3·342	0·236	0·062	0·375	0·055	0·055	—
$Sr_4Ca(ReO_6)_2$	3·414	0·199	0·062	0·379	0·053	0·053	—

apparent in Table 3. The magnitude of the force constant f_{Mo-O} for different B^{II} cations (given in parenthesis) is in the order f_{Mo-O} (Zn) < f_{Mo-O} (Mg)< f_{Mo-O} (Ca) < f_{Mo-O} (Cd). This trend cannot be explained on the basis of atomic masses or ionic radii. This trend can only be explained if the atomic radii of cations Ca^{II} (0·99Å), Cd^{II} (0·97Å), Zn^{II} (0·75Å) and Mg^{II} (0·65 Å) and their atomic masses are considered simultaneously.

The variation of the W—O bond stretching force constant (f_{W-O} in complexes of the type $Ba_2B^{II}WO_6$ (B = Zn, Mg, Ca and Cd) has a similar trend as that of Mo—O bond. The values of f_{W-O} in complexes Ba_2NiWO_6 and Ba_2ZnWO_6 are the same because their atomic masses and ionic radii are nearly equal. The stretching force constant K in MUBFF also follows the same trend as that of f_r in GVFF for the case of molybdates and tungstates.

Vibrational spectra of tellurates are entirely different from those of tungstates and molybdates. For Ba_2ZnTeO_6 and Ba_2NiTeO_6, eight Raman bands are observed in Raman spectra. First two higher frequencies are assigned to A_{1g} mode and the next two higher frequencies to E_g mode. The remaining frequencies correspond to T_{2g} mode. Liegeois-Duyckaerts[8] have shown that these compounds have both hexagonal and cubic symmetries and assigned the highest frequency of A_{1g} mode to the symmetric stretch of the TeO_6 octahedron in which its apexes shared with the apexes of ZnO_6 or NiO_6 octahedron. The next frequency of the A_{1g} is assigned to the same motion of the TeO_6 octahedron and sharing faces with ZnO_6 or NiO_6 octahedron. No distinction is

Table 4—MUBFF Force Constants (in 10^2 Nm^{-1}) of Some $B^{VI}O_6$ Octahedra

Complex	K	H	F	F'	k	h	g
Ba_2ZnMoO_6	3·123	0·113	0·434	−0·236	0·946	−0·219	0·009
Ba_2MgMoO_6	3·159	0·145	0·417	−0·216	0·892	−0·206	0·005
Ba_2CaMoO_6	3·307	0·052	0·435	−0·258	1·016	−0·125	0·004
Ba_2CdMoO_6	3·405	0·028	0·438	−0·269	0·997	−0·133	0·002
Ba_2ZnWO_6	3·724	0·098	0·413	−0·293	0·995	−0·140	0·006
Ba_2MgWO_6	3·770	0·181	0·379	−0·244	0·941	−0·105	0·017
Ba_2CaWO_6	3·874	0·021	0·442	−0·333	0·978	−0·163	0·003
Ba_2CdWO_6	3·952	0·028	0·430	−0·320	1·058	−0·152	0·008
Ba_2NiWO_6	3·702	0·149	0·405	−0·269	0·952	−0·113	0·022
(BaSr) $MgWO_6$	4·172	0·158	0·407	−0·271	0·956	−0·121	0·014
(BaSr) $CaWO_6$	3·828	0·071	0·409	−0 297	0·997	−0·147	0·001
Ba_2MgTeO_6	2·987	0·126	0·456	−0·261	0·129	−0·090	0·040
Ba_2CaTeO_6	3·352	0·163	0·393	−0·203	0·349	−0·060	0·040
Ba_2CdTeO_6	3·206	0·055	0·468	−0·287	0·153	−0·101	0·042
Ba_2NiTeO_6	3·124	0·275	0·300	−0·105	0·073	−0·010	0.042
Pb_2MgTeO_6	3·395	0·013	0·482	−0·316	0·134	−0·117	0·041
$(Pb_{1\cdot5}Ba_{0\cdot5})$ $MeTeO_6$	3·274	0·029	0·481	−0·297	0·146	−0·095	0·053
(PbBa) $MgTeO_6$	3·153	0·060	0·475	−0·280	0·136	−0·077	0·063
$(Pb_{1\cdot5}Sr_{0\cdot5})$ $MgTeO_6$	3·450	0·024	0·485	−0·301	0·138	−0·096	0·054
(PbSr) $MgTeO_6$	3·330	0·026	0·495	−0·308	0·336	−0·097	0·057
(BaSr) $MgTeO_6$	3·44	0·129	0·460	−0·263	0·130	−0·094	0·037
Sr_2MgTeO_6	3·659	0·115	0·491	−0·290	0·140	−0·110	0·034
(BaLa) $LiTeO_6$	3·169	0·230	0·390	−0·165	0·100	−0·044	0·038
(BaLa) $NaTeO_6$	3·227	0·223	0·376	−0·180	0·100	−0·057	0·032
Ba_2MgUO_6	3·263	−0·006	0·421	−0·328	0·398	−0·126	0·038
Ba_2ZnUO_6	3·276	−0·079	0·443	−0·365	0·425	−0·162	0·020
Ba_2NiUO_6	3·185	−0·034	0·408	−0·328	0·386	−0·142	0·022

made for the frequencies of other modes. Similar is the case in the infrared spectra.[8] On the basis of computed results for TeO_6^{6-} ions in other cubic perovskites in above cases, the values of $\nu_2(E_g)$ and $\nu_3(T_{1u})$ are computed using higher frequency of the A_{1g} species. For Ba_2ZnTeO_6, the computed values of $\nu_3(E_g)$ and $\nu_3(T_{1u})$ frequencies are 607 cm^{-1} and 638 cm^{-1} respectively, which are different from their experimental values. This shows that for cubic perovskites and hexagonal perovskites, frequencies occurring in a species are highly coupled with others.

Influence of the nature of A cation on the Te—O stretching force constant in the tellurates A_2MgTeO_6 (A = Sr, Ba, or Pb) is quite obvious from Table 3 in that it increases with the increase of the mass of the A cation belonging to the same group, whereas with the increase of the mass of A cation belonging to the same period it decreases as shown below:

$$f_{Te\text{-}O}\,(Ba_2) < f_{Te\text{-}O}\,(PbBa) < f_{Te\text{-}O}\,(Pb_{1.5}Ba_{0.5}) < f_{Te\text{-}O}\,(Pb_2)$$

and

$$f_{Te\text{-}O}\,(Sr_2) > f_{Te\text{-}O}\,(SrBa) > f_{Te\text{-}O}\,(Ba_2)$$

Similar is the case for K values in MUBFF.

This trend is in line with the ionic radii, which varies in the order Ba^{2+} (1·33 Å) > Pb^{2+} (1·20 Å) > Sr^{2+} (1·13 Å). This influences the cell parameter and hence the Te—O bond lengths. The values of $f_{Te\text{-}O}$ in (BaLa) $LiTeO_6$ and (BaLa) $NaTeO_6$ cubic perovskites show that these are not affected by the cations of the alkali metal.

The ν_2 (E_g) fundamental in the complexes of UO_6 octahedron has been obtained assuming $f_{rr} = f'_{rr}$. It is observed from Table 3 that for the same Ba_2 cation, $f_{U\text{-}O}$ (Mg) > $f_{U\text{-}O}$ (Zn) as for molybdate and tungstate.

A comparative study of the stretching force constants shows that if the A and B cations are the same, they vary in the order $f_{W\text{-}O} > f_{Mo\text{-}O} > f_{U\text{-}O} > f_{Te\text{-}O}$ except for Ca cation in tellurate. This trend is in accordance with the bonding energies of the corresponding bonds.[1]

The effects of the A and B cations on the bending interaction constant $(f_\alpha - f''_{\alpha\alpha})$, stretch interaction force constant (f_{rr}), stretch-bend interaction force constant $(f_{r\alpha} - f''_{r\alpha})$ and bend-bend interaction force constant $(f_{\alpha\alpha} - f''_{\alpha\alpha})$, are also very interesting. Corresponding to the same A cation, $(f_\alpha - f''_{\alpha\alpha})$ and f_{rr} exhibit opposite trends to each other for MoO_6 and WO_6 octahedrons, having different B cations. It is also evident from Table 3 that the stretch-stretch interaction force constant (f_{rr}) varies in the sequence f_{rr} (Mg) < f_{rr} (Zn), whereas f_{rr} (Ca) ≈ f_{rr} (Cd). The remaining interaction force constants are also split into two groups one corresponding to Mg and Zn as B cation and the other corresponding to Ca and Cd as B cation.

The cation Li or Na has no influence on any interaction force constant in tellurates. Similar is the effect of A cation on the force constants possessing the same B cation (Mg). With the increase of the mass of A cation belonging to the same period, the bending force constant $(f_\alpha - f''_{\alpha\alpha})$ has the opposite trend of the stretching force constant. The other force constants such as, $(f_{r\alpha} - f''_{r\alpha})$, f_{rr} and $(f_{\alpha\alpha} - f''_{\alpha\alpha})$ vary in the same way as the stretching force constant.

On the other hand, the force constants $(f_\alpha - f''_{\alpha\alpha})$ and $(f_{r\alpha} - f''_{r\alpha})$ show increasing tendency while f_{rr} and $(f_{\alpha\alpha} - f''_{\alpha\alpha})$ show decreasing tendency with the increase of mass of the A cation belonging to the same group.

It is interesting to study the non-bonded interaction in octahedral complexes. For this purpose the useful information is contained in the non-bonded interaction force constants F and F'. An observation of these values from Table 4 shows that the non-bonded interactions are not influenced with respective cations but the cationic effect on this interaction is more pronounced in MoO_6 octahedra as compared to WO_6 octahedron. From this it may be concluded that large value of F for MoO_6 octahedra is responsible for weakening of Mo—O bond as compared to W—O bond.

The computed values of the bond orders are included in the last column of Table 3. An inspection of these values with respect to A and B cations shows that they follow the same trend as the corresponding stretching force constants. It is further noted that the π-bonding in ordered cubic perovskites of the oxyanions Mo, W and U is more pronounced as compared to that in tellurates. The values of bond order for the tetrahedral oxyanions of Mo and W are 2·1 and 2·2 respectively.[9] A comparison of these values with the corresponding values for octahedral oxyanions (Table 3) clearly shows that the π-interaction dominates in tetrahedral as compared to octahedral oxyanions.

Acknowledgement

One of the authors (ANP) is thankful to the University Grants Commission, New Delhi for financial assistance and another author (UPV) is thankful to CSIR, New Delhi, for awarding him a post doctoral fellowship.

References

1. Duyckaerts M L & Tarte P, *Spectrochim. Acta*, **30A** (1974), 1771.
2. Wilson (Jr) E B, Decius J C & Cross P C, *Molecular vibrations* (McGraw-Hill, New York), 1955.
3. Pandey A N, Sharma D K, Verma U P, Arora L D, Gupta S L & Singh B P, *Indian J. pure appl. Phys.*, 14 (1976), 815.
4. Cyvin S J, *Molecular vibrations and mean square amplitudes* (Elsevier, Amsterdam), 1968.
5. Siebert H, *Z. anorg. allgem. Chemie*, 273 (1953), 170.
6. Pandey A N, Sharma D K & Dublish A K, *Spectrosc. Lett.*, 6 (1973), 491.
7. Ahmad P & Sanyal N K, *Spectrosc. Lett.*, 9 (1976), 39.
8. Duyckaerts M L, *Spectrochim. Acta*, 31A (1975), 1585.
9. Gupta S L, Verma U P & Pandey A N, *Acta Phys. Polon.*, A55 (1979), 153.

Indian Journal of Pure & Applied Physics
Vol. 18, July 1980, pp. 516-523

Molecular Constants of Some Hexahaloanions of Group IV A & Group V A Belonging to O_h Point Group

P C Sarkar & G C Singh

Department of Physics, St. Andrew's College, Gorakhpur 273 001

Received 6 *May* 1979

Some mutual relations between quadratic potential constants, kinetic constants and mean square amplitude quantities have been examined. The necessary molecular constants have been obtained from symmetry force constants, inverse elements of G-matrices and symmetrized mean square amplitude matrices using Wilson's GF matrix method. The second order secular equation has been solved by the kinetic constant method. Symmetry force constants calculated by MOVFF and MUBFF are in reasonable agreement with the evaluated force constants. The Coriolis coupling constants ξ_3 (f_{1u}) have been calculated using symmetry force constant values and are found to be in exact agreement with those calculated by the formula given by A Muller, B Kreb and S J Cyvin [*J. molec. Phys.*, **14** (1968), 491]. This confirms the accuracy of the present computation.

1. Introduction

From an analogy of the expressions of kinetic and potential energies in terms of Wilson's G and F matrices,[1] Thirugnanasambandam and Srinivasan[2] defined the so called kinetic constants. They pointed out certain interesting mutual relations between these kinetic constants for many simple molecular systems.[3-7] Later Sanyal *et al.*[8-10] pointed out the influence of kinetic constants on quadratic potential constants. Recently, Sarkar and Singh,[11-13] guided by the structural similarity of the expressions for symmetry force constants, inverse elements of G matrices and symmetrized mean square amplitude matrices with the quadratic potential constants, kinetic constants and mean square amplitude quantities, showed that similar mutual relations exist in the case of potential constants and mean square amplitude quantities, though there are certain differences.

Since the octahedral system contains some identical G matrix elements in different species with the result that some kinetic constants vanish, whereas the corresponding quadratic potential constants do not vanish, we considered it relevant to examine the mutual relations between the molecular constants of this system.

2. Theoretical Consideration

Octahedral molecules of the type XY_6 give rise, according to the relevant selection rules,[14] to 15 vibrational degrees of freedom forming 6 fundamental frequencies. They are distributed under the various irreducible representations as:

$$\Gamma = a_{1g} + e_g + 2f_{1u} + f_{2g} + f_{2u}$$

Calculations of symmetry force constants and symmetrized mean square amplitude matrices of a_{1g}, e_g, f_{2g} and f_{2u} species, which involve single frequencies, are straightforward. F and Σ matrices for the degenerate f_{1u} species can be obtained by solving the second order secular equation by various approximate methods. Kinetic constant method which

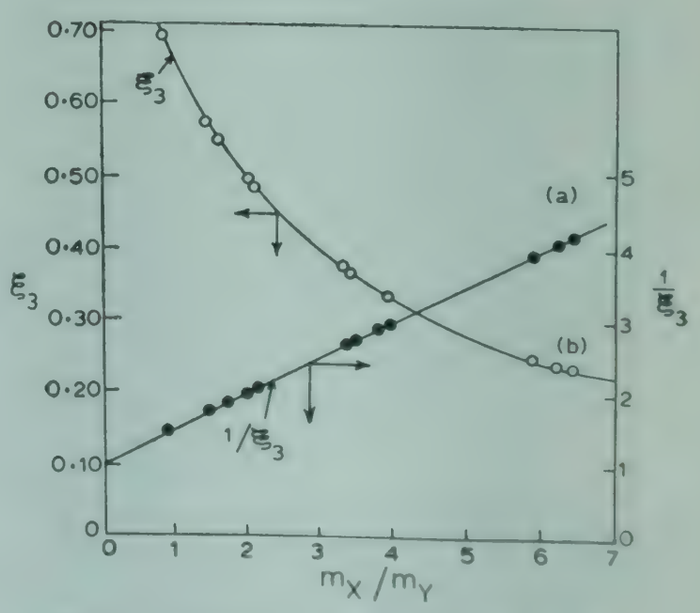

Fig. 1—Variation of m_X/m_Y with ξ_3 and $1/\xi_3$ for octahedral XY_6 type ions

is equivalent to Peacock and Muller's L-matrix approximation method $L_{12} = 0$ (Ref. 15 and 16) was adopted for the calculation of F and Σ matrices. Symmetry force constants calculated using OVFF[17] and UBFF[18] methods are in close agreement. To further test the accuracy of the calculated force constants, Coriolis coupling constant ξ_3 (f_{1u}) was calculated using Cyvin's[19] formula as well as that of Muller *et al.*[20] Identical results obtained from both the formulae confirm the reliabilities of the force constants.

Effect of mass ratio m_x/m_y on the Coriolis coupling constants ξ_3 (f_{1u}) has been studied by plotting ξ_3 versus m_x/m_y, as well as by plotting $1/\xi_3$ versus m_x/m_y (Fig. 1). In Fig. 1, since plot (a) is linear and any deviation from straight line can be detected more easily than from the conventional plot (b), it appears that plot (a) is more desirable than plot (b).

The various molecular constants involved in the present study have been defined in Table 1. Using relevant symmetry coordinates from literature,[21]

Table 1 – Notations Used for Defining Molecular Constants

Nature	GVFF constants	Kinetic constants	Mean square amplitude quantities
Stretching	f_r	k_r	σ_r
Bond-bond interaction adjacent bond	f_{rr}	k_{rr}	σ_{rr}
Opposite bonds	f'_{rr}	k'_{rr}	σ'_{rr}
Bending	f_α	k_α	σ_α
Angle-angle interaction			
An angle with an angle in a perpendicular plane with common bond	$f_{\alpha\alpha}$	$k_{\alpha\alpha}$	$\sigma_{\alpha\alpha}$
An angle with an angle adjacent to it in the same plane	$f'_{\alpha\alpha}$	$k'_{\alpha\alpha}$	$\sigma'_{\alpha\bar{\alpha}}$
An angle with an angle in a perpendicular plane (no common bond)	$f''_{\alpha\alpha}$	$k''_{\alpha\alpha}$	$\sigma''_{\alpha\alpha}$
An angle with a distant angle in the same plane	$f'''_{\alpha\alpha}$	$k'''_{\alpha\alpha}$	$\sigma'''_{\alpha\alpha}$
Bond-angle interaction			
A bond with an adjacent angle	$f_{r\alpha}$	$k_{r\alpha}$	$\sigma_{r\alpha}$
A bond with an angle in a perpendicular plane	$f'_{r\alpha}$	$k'_{r\bar{\alpha}}$	$\sigma'_{r\alpha}$
A bond with a distant angle	$f''_{r\alpha}$	$k''_{r\alpha}$	$\sigma''_{r\alpha}$

Table 3—Fundamental Frequencies (in cm^{-1}) of Some Octahedral XY_6 Type Ions

Ion	ν_1 (a_{1g})	ν_2 (e_g)	ν_3 (f_{1u})	ν_4 (f_{1u})	ν_5 (f_{2g})	ν_6 (f_{2u})*	Ref.
SiF_6^{2-}	663	477	741	483	408	289	26
GeF_6^{2-}	624	471	603	359	335	237	26
SnF_6^{2-}	592	477	559	300	252	178	26
PF_6^-	751	580	830	558	477	337	26
AsF_6^-	685	576	699	392	372	263	26
SbF_6^-	668	558	669	350	294	208	26
$BiCl_6^{2-}$	251	202	171	120	134	95	27
$GeCl_6^{2-}$	318	213	310	213	198	140	27
$SnCl_6^{2-}$	310	245	300	165	175	124	27
PCl_6^-	353	262	444	285	238	168	27
$AsCl_6^-$	337	289	348	220	202	143	27,28
$SbCl_6^-$	329	280	348	182	170	120	28

* Calculated by Wilson's rule.

Table 2—F, K (G^{-1}) and Σ Matrices in Terms of GVFF, Kinetic Constant and Mean Square Amplitude Quantities

Species	F	GVFF	K (G^{-1})	Kinetic constant	Σ	Mean square amplitude quantities
a_{1g}	F_{11}	$f_r + 4f_{rr} + f'_{rr}$	K_{11}	$k_r + 4k_{rr} + k'_{rr}$	Σ_{11}	$\sigma_r + 4\sigma_{rr} + \sigma'_{rr}$
e_g	F_{22}	$f_r - 2f_{rr} + f'_{rr}$	K_{22}	$k_r - 2k_{rr} + k'_{rr}$	Σ_{22}	$\sigma_r - 2\sigma_{rr} + \sigma'_{rr}$
f_{1u}	F_{33}	$f_r - f'_{rr}$	K_{33}	$k_r - k'_{rr}$	Σ_{33}	$\sigma_r - \sigma'_{rr}$
	F_{44}	$f_\alpha + 2f_{\alpha\alpha} - 2f''_{\alpha\alpha} - f'''_{\alpha\alpha}$	K_{44}	$k_\alpha + 2k_{\alpha\alpha} - 2k''_{\alpha\alpha} - k'''_{\alpha\alpha}$	Σ_{44}	$\sigma_\alpha + 2\sigma_{\alpha\alpha} - 2\sigma''_{\alpha\alpha} - \sigma'''_{\alpha\alpha}$
	F_{34}	$2(f_{r\alpha} - f''_{r\alpha})$	K_{34}	$2(k_{r\alpha} - k''_{r\alpha})$	Σ_{34}	$2(\sigma_{r\alpha} - \sigma''_{r\alpha})$
f_{2g}	F_{55}	$f_\alpha - 2f'_\alpha + f'''_{\alpha\alpha}$	K_{55}	$k_\alpha - 2k'_{\alpha\alpha} + k'''_{\alpha\alpha}$	Σ_{55}	$\sigma_\alpha - 2\sigma'_\alpha + \sigma'''_{\alpha\alpha}$
f_{2u}	F_{66}	$f_\alpha - 2f_{\alpha\alpha} + 2f''_{\alpha\alpha} - f'''_{\alpha\alpha}$	K_{66}	$k_\alpha - 2k_{\alpha\alpha} + 2k''_{\alpha\alpha} - k'''_{\alpha\alpha}$	Σ_{66}	$\sigma_\alpha - 2\sigma_{\alpha\alpha} + 2\sigma''_{\alpha\alpha} - \sigma'''_{\alpha\alpha}$

relations between symmetry force constants, symmetrized mean square amplitude matrices and the corresponding general valence force constants and mean square amplitude quantities can be easily obtained. Similarly using the G matrices from literature,[21] the relation between the symmetrized kinetic constants K_{ij} defined as $K_{ij} = G^{-1}$ and the corresponding kinetic constants pertaining to stretching, bending and interaction modes can be obtained. Structural similarities between F, G^{-1} and Σ matrices with the corresponding GVFF, kinetic constants and σ matrices are evident from Table 2.

Use of the following redundancy constraints makes it possible to compute all the relevant molecular constants.

Table 4—Symmetry Force Constants (in 10^5 dyne/cm) and Coriolis Coupling Constants of Some Octahedral XY_6 Type Ions

Ion	Method	F_{33}	F_{34}	F_{44}	ξ_3	ξ_4	Ion	Method	F_{33}	F_{34}	F_{44}	ξ_3	ξ_4
SiF_6^{2-}	a	3·4154	0·6984	0·6073			$BiCl_6^{2-}$	a	0·4816	0·0506	0·0998		
	b	3·2849	0·6445	0·6094	0·5750	−0·0750		b	0·5002	0·1278	0·1236	0·2531	0·2469
	c	3·7822	0·6473	0·4536				c	0·5749	0·1264	0·0933		
GeF_6^{2-}	a	2·8735	0·2938	0·4275			$GeCl_6^{2-}$	a	1·2489	0·2355	0·2383		
	b	2·9932	0·3909	0·4326	0·3436	0·1564		b	1·3842	0·3206	0·2491	0·4941	0·0059
	c	3·5007	0·5115	0·3055				c	1·5106	0·3176	0·2047		
SnF_6^{2-}	a	2·7294	0·1645	0·3392			$SnCl_6^{2-}$	a	1·2678	0·1216	0·1627		
	b	2·5309	0·0006	0·3551	0·2425	0·2575		b	1·4281	0·2697	0·1849	0·3739	0·1261
	c	3·3458	0·3753	0·1734				c	1·3873	0·2055	0·1592		
PF_6^-	a	4·4694	0·9137	0·8291			PCl_6^-	a	1·9388	0·4936	0·3546		
	b	4·4120	0·8880	0·8294	0·5501	−0·0501		b	1·8778	0·4725	0·3553	0·6960	−0·1960
	c	4·6324	0·6948	0·6211				c	1·6482	0·3188	0·2968		
AsF_6^-	a	3·8616	0·3460	0·5141			$AsCl_6^-$	a	1·4647	0·1699	0·1747		
	b	4·0477	0·5024	0·5232	0·3365	0·1635		b	2·0741	0·4436	0·2043	0·4388	0·0161
	c	4·1199	0·4196	0·4545				c	1·5199	0·1712	0·2126		
SbF_6^-	a	3·9236	0·2210	0·4646			$SbCl_6^-$	a	1·7066	0·1466	0·1993		
	b	3·6647	−0·0009	0·4842	0·2378	0·2622		b	1·7793	0·2004	0·2016	0·3679	0·1321
	c	4·6729	0·4117	0·2353				c	1·8717	0·1700	0·2126		

a, Kinetic constant method; b, MOVFF method; c, MUBFF method

Table 5—Kinetic Constants (in 10^{-23} g) of Some Octahedral XY_6 Type Ions

Ion	k_r	k'_{rr} k''_{rr}	k_α	$-k'''_{\alpha\alpha}$ $k''_{\alpha\alpha}$	$-k''_{r\alpha}$	ΣK_{ij}	$6\mu_y \Sigma K_{ij}$
SiF_6^{2-}	2·7323	0·0000 0·4217	0·7748	0·3805 0·1054	0·2109	18·9240	36·0000
GeF_6^{2-}	2·8328	0·0000 0·3212	0·8250	0·4308 0·0803	0·1606	18·9240	36·0000
SnF_6^{2-}	2·8965	0·0000 0·2575	0·8569	0·4626 0·0644	0·1288	18·9240	36·0000
PF_6^-	2·7406	0·0000 0·4134	0·7789	0·3847 0·1033	0·2067	18·9240	36·0000
AsF_6^-	2·8450	0·0000 0·3090	0·8311	0·4369 0·0773	0·1545	18·9240	36·0000
SbF_6^-	2·8999	0·0000 0·2541	0·8586	0·4643 0·0635	0·1271	18·9240	36·0000
$BiCl_6^{2-}$	5·3900	0·0000 0·4947	1·5916	0·8560 0·1227	0·2473	35·3083	36·0000
$GeCl_6^{2-}$	5·1535	0·0000 0·7312	1·4734	0·7378 0·1828	0·3656	35·3083	36·0000
$SnCl_6^{2-}$	5·2552	0·0000 0·6295	1·5242	0·7886 0·1574	0·3147	35·3083	36·0000
PCl_6^-	5·0286	0·0000 0·8561	1·4109	0·6753 0·2140	0·4281	35·3083	36·0000
$AsCl_6^-$	5·1718	0·0000 0·7129	1·4825	0·7469 0·1782	0·3565	35·3083	36·0000
$SbCl_6^-$	5·2611	0·0000 0·6237	1·5271	0·7916 0·1559	0·3118	35·3083	36·0000

Redundancy constraints

$$f'_{r\alpha} = 0 \qquad K'_{r\alpha} = 0$$

$$f_{r\alpha} + f''_{r\alpha} = 0 \qquad K_{r\alpha} + K''_{r\alpha} = 0$$

$$f_{\alpha\alpha} + f''_{\alpha\alpha} = 0 \qquad K_{\alpha\alpha} + K''_{\alpha\alpha} = 0$$

$$f_{\alpha} + 2 f'_{\alpha\alpha} + f'''_{\alpha\alpha} = 0 \quad K_{\alpha} + 2 K_{\alpha\alpha} + K'''_{\alpha\alpha} = 0$$

$$\sigma'_{r\alpha} = 0 \qquad \sigma_{\alpha\alpha} + \sigma''_{\alpha\alpha} = 0$$

$$\sigma_{r}\alpha + \sigma''_{r\alpha} = 0 \qquad \sigma_{\alpha} + 2\sigma''_{\alpha\alpha} + \sigma'''_{\alpha\alpha} = 0$$

3. Results and Discussion

The frequencies necessary for the present calculation are given in Table 3; ν_6 (f_{2u}) which is inactive has been computed by Wilson's rule ($\nu_6 = 1/\sqrt{2}\,\nu_5$). Symmetry force constants belonging to f_{1u} species calculated by using various force fields are presented in Table 4 along with Coriolis coupling constants. Kinetic constants, GVFF constants and mean square amplitude quantities, are presented in Tables 5, 6 and 7 respectively. Wherever available, molecular constants reported by other authors are presented in parentheses.

Table 6—Force Constants (in 10^5 dyne cm^{-1}) of Some Octahedral XY_6 Type Ions

Ion	f_r	f_{rr} f'_{rr}	f_a	$-f'''_{\alpha\alpha}$ $-f''_{\alpha\alpha}$	$f'_{r\alpha}$	$\Sigma f_{ij}=6F_{11}$	$\frac{6\mu_y \Sigma f_{ij}}{\lambda_1}$	Ref.
SiF_6^{2-}	3·3767 (3·220)	0·3956 −0·3867 (0·400) (0·110)	0·3878 (0·385)	0·1549 0·0162 (0·155) (0·020)	0·1746 (0·150)	29·5224	36·0000	23
GeF_6^{2-}	2·9909 (2·950)	0·3126 0·1174 (0·310) (0·150)	0·2661 (0·2575)	0·1090 0·0131 (0·0925) (0·0050)	0·0735 (0·0550)	26·1511	36 0000	23
SnF_6^{2-}	2·9074 (2·860)	0·2293 0·0982 (0·230) (0·150)	0·1747 (0·175)	0·0859 0·0197 (0·0850) (0·0200)	0·0411 (0·0350)	23·5380	36·0000	23
PF_6^{-}	4·5421 (4·350)	0·4246 0·0727 (0·420) (0·270)	0·5295 (0·530)	0·2112 0·0221 (0·210) (0·025)	0·2284 (0·190)	37·8795	36·0000	23
AsF_6^{-}	4·0441 (4·010)	0·2564 0·1825 (0·260) (0·210)	0·2035 (0·3225)	0·1117 0·0243 (0·1275) (0·015)	0·0843 (0·075)	31·5142	36·0000	23
SbF_6^{-}	3·9561 (3·940)	0·2516 0·0324 (0·250) (0·040)	0·2387 (0·2375)	0·1178 0·0270 (0·1125) (0·025)	0·0552 (0·050)	29·9694	36·0000	23
$BiCl_6^{2-}$	0·7442	0·0773 0·2626	0·0720	0·0251 0·0007	0·0126	7·8947	36·0000	
$GeCl_6^{2-}$	1·2919 (1·6226)	0·1941 0·0438 (0·1939) (0·3799)	0·1619 —	0·0596 0·0042 — (0·0041)	0·0589 (0·0583)	12·6711	36·0000	24
$SnCl_6^{2-}$	1·3863 (1·8173)	0·1256 0·1185 (0·1895) (0·4363)	0·1208 —	0·0408 0·0003 — (0·0055)	0·0304 (0·0153)	12·0423	36·0000	24
PCl_6^{2-}	1·8810 (2·3464)	0·1948 —0·0578 (0·1947) (0·3691)	0·2362 —	0·0884 0·0075 — (0·0074)	0·1234 (0·1261)	15·6148	36·0000	24
$AsCl_6^{-}$	1·7091 (2·1121)	0·1046 0·2444 (0·1045) (0·8173)	0·1503 —	0·0438 0 0059 — (0·0054)	0·0612 (0·0603)	14·2314	36·0000	24
$SbCl_6^{-}$	1·7759 (2·2522)	0·1039 0·0693 (0·1038) (0·5141)	0.1251 —	0·0497 0·0061 — (0·0043)	0·0367 (0·0423)	13·5637	36·0000	

Table 7—Mean Square Amplitude Quantities (in 10^{-4} Å^2) of Some Octahedral XY_6 Type Ions

Symbol	0 K	298 K	500 K	0 K	298 K	500 K
		SiF_6^{2-}			GeF_6^{2-}	
σ_r	22·5160 (22·518)	24·8921 (24·895)	31·2923 (31·405)	19·8569 (19·858)	22·7932 (22·833)	33·1694 (29·965)
$-\sigma_{rr}$	0·8697 (1·361)	1·3689 (1·051)	2·1972 (0·819)	0·7698 (1·600)	1·2450 (1·369)	2·0079 (1·305)
$-\sigma'_{rr}$	5·6551 (5·656)	4·8983 (4·899)	4·4575 (4·454)	2·5592 (2·559)	2·1250 (2·163)	5·2581 (2·052)
$\sigma_{r\alpha} = -\sigma''_{r\alpha}$	8·0988 (8·100)	8·5644 (8·566)	10·2776 (10·279)	3·8512 (3·851)	4·2811 (4·294)	6·6021 (5·500)
σ_α	63·5899 (150·834)	81·3115 (182·933)	113·5705 (247·722)	65·3304 (135·825)	97·7968 (196·055)	146·5866 (288·870)
$\sigma_{\alpha\alpha} = -\sigma''_{\alpha\alpha}$	8·1377 (8·145)	7·5838 (7·594)	8·4836 (8·501)	4·0728 (4·072)	3·6401 (3·647)	4·7050 (4·326)
$-\sigma'_{\alpha\alpha}$	21·7459 (21·748)	28·7948 (28·798)	41·2044 (41·209)	26·4846 (26·493)	39·5951 (39·599)	59·1382 (59·143)
$-\sigma'''_{\alpha}$	20·1130 (20·113)	23·7219 (23·743)	31·1616 (31·194)	12·3612 (12·361)	18·6066 (18·607)	28·3102 (27·556)
$\Sigma\sigma_{ij} = 6\,\Sigma_{11}$	80·2925	87·1085	108·2758	85·3107	94·1307	119·2770
$\frac{6\,\Sigma\sigma_{ij}}{\mu_y\,\Delta_1}$	36·0000	36·0000	36·0000	36·0000	36·0000	36·0000
		SnF_6^{2-}			PF_6^{-}	
σ_r	19·1743 (19·176)	22·3667 (22·369)	29·7396 (29·742)	18·9709 (18·971)	20·1794 (20·180)	24·2569 (24·257)
$-\sigma_{rr}$	0·6022 (1·896)	0·9867 (1·815)	1·5953 (2·015)	0·5810 (1·389)	0·8028 (1·274)	1·2517 (1·230)
$-\sigma'_{rr}$	1·7785 (1·779)	1·6087 (1·608)	1·7009 (1·701)	4·8348 (4·834)	4·5078 (4·507)	4·3599 (4·359)
$\sigma_{r\alpha} = -\sigma''_{r\alpha}$	2·5405 (2·541)	2·9070 (2·907)	3·8122 (3·812)	6·5580 (4·338)	6·8009 (6·800)	7·8834 (7·880)
σ_α	76·0028 (99·202)	133·5704 (171·149)	207·8267 (282·079)	53·5726 (125·382)	64·0943 (143·977)	86·1817 (187·561)
$\sigma_{\alpha\alpha} = -\sigma''_{\alpha\alpha}$	2·7937 (2·794)	1·9421 (4·382)	2·5912 (7·192)	6·4509 (6·450)	5·9464 (5·945)	6·3160 (6·315)
$-\sigma'_{\alpha\alpha}$	35·2077 (35·211)	64·8431 (64·955)	101·3222 (101·325)	18·6003 (18·602)	22·7315 (22·934)	31·2292 (31·232)
$-\sigma'''_{\alpha\alpha}$	5·5874 (5·587)	3·8842 (4·338)	5·1823 (14·383)	16·3720 (16·370)	18·6313 (18·629)	23·7233 (23·722)
$\Sigma\sigma_{ij} = 6\,\Sigma_{11}$	89·9220	100·8662	129·9456	70·8737	74·7614	89·3424
$\frac{6\,\Sigma\sigma_{ij}}{\mu_y\,\Delta_1}$	36·0000	36·0000	36·0000	36·0000	36·0000	36·0000
		AsF_6^{-}			SbF_6^{-}	
σ_r	16·8586 (16·860)	18·3789 (18·381)	22·9307 (22·932)	16·2136 (16·215)	17·8819 (17·884)	22·6059 (22·609)
$-\sigma_{rr}$	0·4085 (1·750)	0·5836 (1·739)	0·9187 (1·938)	0·4364 (1·777)	0·6374 (1·760)	1·0090 (1·936)
$-\sigma'_{rr}$	2·2722 (2·272)	2·1076 (2·107)	2·1101 (2·110)	1·1861 (1·186)	0·9509 (0·951)	0·7363 (0·731)
$\sigma_{r\alpha} = -\sigma''_{r\alpha}$	3·2189 (3·219)	3·4071 (3·447)	4·0224 (4·213)	2·0688 (2·070)	2·2392 (2·240)	2·7753 (2·776)
σ_α	58·7273 (122·033)	82·4691 (166·395)	117·9628 (240·145)	64·9537 (124·032)	102·3782 (164·110)	154·8676 (271·993)
$\sigma_{\alpha\alpha} = -\sigma''_{\alpha\alpha}$	3·6615 (3·661)	3·4071 (3·407)	4·0224 (4·028)	2·2989 (2·300)	1·7589 (1·115)	1·8869 (1·888)
$-\sigma'_{\alpha\alpha}$	23·8504 (23·852)	33·3411 (33·345)	48·7361 (48·733)	30·1780 (30·181)	49·4302 (49·437)	75·5469 (75·555)
$-\sigma'''_{\alpha\alpha}$	11·0265 (11·026)	15·7870 (15·787)	22·9894 (22·977)	4·5977 (4·600)	3·5178 (3·230)	3·7738 (3·775)
$\Sigma\sigma_{ij} = 6\Sigma_{11}$	77·7138	83·6206	102·8739	79·6916	86·2884	107·0007
$\frac{6\,\Sigma\sigma_{ij}}{\mu_y\,\Delta_1}$	36·0000	36·0000	36·0000	36·0000	36·0000	36·0000

Contd.

Table 7—Mean Square Amplitude Quantities (in 10^{-4} Å^2) of Some Octahedral XY_6 Type Ions (Contd.)

Symbol	0 K	298 K	500 K	0 K	298 K	500 K
		$BiCl_6^{2-}$			$GeCl_6^{2-}$	
σ_r	29·6256 (29·364)	70·8226 (70·853)	114·0809 (114·093)	25·0950 (25·094)	43·0428 (43·508)	67·0759 (66·753)
σ_{rr}	0·7659 (1·869)	2·8398 (2·895)	4·7574 (4·362)	1·2286 (1·126)	3·7773 (0·215)	6·6970 (2·265)
$-\sigma'_{rr}$	7·6165 (7·873)	24·4606 (24·474)	40·3303 (40·340)	5·2270 (5·227)	4·7705 (5·487)	5·3558 (5·680)
$\sigma_{\alpha\bar{\alpha}} = -\sigma''_{r\alpha}$	4·7167 (4·717)	12·0677 (12·074)	19·5563 (19·560)	7·4912 (7·491)	11·8125 (11·817)	17·8947 (17·896)
σ_α	92·7560 (170·422)	336·5635 (624·663)	555·0988 (865·387	70·5960 (100·154)	164·7355 (247·178)	264·3754 (399·909)
$\sigma_{\alpha\alpha} = -\sigma''_{\alpha\alpha}$	3·6067 (1·185)	0·4949 (5·902)	0·1376 (7·732)	6·3066 (1·095)	3·2120 (8·460)	3·4527 (14·239)
$-\sigma'_{\alpha\alpha}$	35·4871 (35·486)	113·5011 (113·560)	186·3375 (186·332)	24·0165 (24·016)	54·0142 (54·041)	86·5717 (56·974)
$-\sigma'''_{\alpha\alpha}$	21·7818	109·5613	182·4238	22·5630	56·7072	91·2320
$\Sigma\,\sigma_{ij} = 6\,\Sigma_{11}$	113·6718	210·0169	328·3255	89·7221	138·9789	209·5940
$\frac{6\,\Sigma\,\sigma_{ij}}{\mu_y\,\Delta_1}$	36·0000	36·0000	36·0000	36·0000	36·0000	36·0000
		$SnCl_6^{2-}$			PCl_6^{-}	
σ_r	21·6857 (21·685)	36·6508 (36·666)	56·3423 (56·344)	25·9095 (25·908)	36·3436 (36·354)	52·8220 (50·857)
$-\sigma_{rr}$	0·6783 (1·878)	2·0609 (1·969)	3·4467 (2·661)	0·7798 (1·465)	2·1605 (1·083)	3·6069 (1·187)
$-\sigma'_{rr}$	3·6330 (3·634)	4·2181 (4·221)	5·9129 (5·917)	9·3192 (9·319)	8·2406 (8·241)	9·6291 (9·671)
$\sigma_{r\alpha} = -\sigma''_{r\alpha}$	4·7339 (4·734)	7·6411 (7·645)	11·6399 (11·641)	12·2593 (12·259)	15·5150 (15·519)	21·7325 (20·368)
σ_α	77·5152 (135·369)	223·6582 (345·905)	364·6853 (645·254)	71·1522 (45·941)	130·3461 (123·102)	201·9081 (212·826)
$\sigma_{\alpha\bar{\alpha}} = -\sigma''_{\alpha\alpha}$	3·5562 (0·016)	−5·5224 (11·240)	−10·4624 (19·213)	11·4334 (5·584)	9·1248 (12·358)	10·9630 (18·153)
$-\sigma'_{\alpha\alpha}$	27·1730 (27·172)	68·1015 (68·138)	110·1903 (110·183)	19·9801 (19·980)	38·5198 (38·538)	60·1603 (60·614)
$-\sigma'''_{\alpha\alpha}$	23·1692 (15·087)	87·4552 (86·057)	114·3046 (126·900)	31·1919 (2·894)	53·3064 (10·118)	80·6875 (22·054)
$\Sigma\,\sigma_{ij} = 6\,\Sigma_{11}$	92·0375	145·1292	219·8547	80·8262	116·7662	172·5932
$\frac{6\,\Sigma\,\sigma_{ij}}{\mu_y\,\Delta_1}$	36·0000	36·0000	36·0000	36·0000	36·0000	36·0000
		$AsCl_6^{-}$			$SbCl_6^{-}$	
σ_r	21·1344 (21·131)	31·9880 (31·995)	47·9083 (47·901)	18·8793 (18·880)	29·0189 (29·030)	43·6306 (43·626)
$-\sigma_{rr}$	0·3906 (1·961)	1·0467 (2·456)	1·7465 (3·477)	0·4216 (1·987)	1·0861 (2·485)	1·9385 (3·519)
$-\sigma'_{rr}$	5·4614 (5·459)	6·7891 (6·789)	9·5753 (9·571)	2·7393 (2·741)	2·5014 (2·505)	3·0954 (3·104)
$\sigma_{r\alpha} = -\sigma''_{r\alpha}$	3·9771 (6·466)	5·7986 (9·431)	8·5959 (13·975)	3·9770 (3·978)	5·7986 (5·800)	8·5959 (8·598)
σ_α	77·7175 (100·267)	175·5668 (240·962)	280·8441 (389·287)	73·3899 (126·781)	201·4018 (341·234)	327·4255 (567·478)
$\sigma_{\alpha\alpha} = -\sigma''_{\alpha\bar{\alpha}}$	10·4614 (0·811)	11·7008 (7·761)	16·8407 (13·080)	2·8952 (−0·028)	−5·5689 (−10·280)	−10·4993 (−16·791)
$-\sigma'_{\alpha\alpha}$	23·5409 (23·540)	52·0417 (52·067)	83·2655 (83·280)	27·9722 (27·971)	71·9431 (71·972)	116·6324 (116·628)
$-\sigma'''_{\bar{\alpha}\alpha}$	30·6356 (8·124)	71·4834 (32·804)	114·3131 (54·819)	17·4455 (11·587)	57·5155 (48·069)	94·1607 (81·463)
$\Sigma\,\sigma_{ij} = 6\,\Sigma_{11}$	84·6635	126·0727	188·0825	86·7223	133·0375	196·6873
$\frac{6\,\Sigma\,\sigma_{ij}}{\mu_Y\,\Delta_1}$	36·0000	36·0000	36·0000	36·0000	36·0000	36·0000

Values in parentheses are from Ref. 25.

Table 8—Complementary and Supplementary Characters of the Molecular Constant Groups 1-3

GVFF	Kinetic constant	Mean square amplitude quantities
1. Stretching and bond-bond interaction constants		
$\Sigma f_r + \Sigma f_{rr} + \Sigma f'_{rr}$	$\Sigma K_r + \Sigma K_{rr} + \Sigma K'_{rr}$	$\Sigma \sigma_r + \Sigma \sigma_{rr} + \Sigma \sigma'_{rr}$
$= 6 f_r + 12 (2 f_{rr}) + 6 f'_{rr}$	$= 6 K_r + 12 (2 K_{rr}) + 6 K'_{rr}$	$= 6 \sigma_r + 12 (2 \sigma_{rr}) + 6 \sigma'_{rr}$
$= 6 f_r + 24 f_{rr} + 6 f'_{rr}$	$= 6 K_r + 24 K_{rr} + 6 K'_{rr}$	$= 6 \sigma_r + 24 \sigma_{rr} + 6 \sigma'_{rr}$
$= \frac{6 \lambda_1}{\mu_y}$	$= \frac{6}{\mu_y}$	$= 6 \Delta_1 \mu_y$
2. Bending and angle-angle interaction constants exhibit mutually complementary character as shown below		
$\Sigma f_\alpha + \Sigma f''_{\alpha\alpha}) + \Sigma f'_{\alpha\alpha} + 0$	$\Sigma K_\alpha + \Sigma K''_{\alpha\alpha} + \Sigma K'_{\alpha\alpha} = 0$	$\Sigma \sigma_\alpha + \Sigma \sigma''_{\alpha\alpha} + \Sigma \sigma'_{\alpha\alpha} = 0$
$12 f_\alpha + 6 (2 f''_{\alpha\alpha} + 12 (2 f'_{\alpha\alpha}) = 0$	$12 K_\alpha + 6 (2 K''_{\alpha\alpha}) + 12 (2 K'_{\alpha\alpha}) = 0$	$12 \sigma_\alpha + 6 (2 \sigma''_{\alpha\alpha}) + 12 (2 \sigma'_{\alpha\alpha}) = 0$
$f_\alpha + f''_{\alpha\alpha} + 2 f'_{\alpha\alpha} = 0$	$K_\alpha + K''_{\alpha\alpha} + 2 K'_{\alpha\alpha} = 0$	$\sigma_\alpha + \sigma''_{\alpha\alpha} + 2 \sigma'_{\alpha\alpha} = 0$
3. Bond-angle interaction constants		
$\Sigma f_{r\alpha} + \Sigma f''_{r\alpha} = 0$	$\Sigma K_{r\alpha} + \Sigma K''_{r\alpha} = 0$	$\Sigma \sigma_{r\alpha} + \Sigma \sigma''_{r\alpha} = 0$
$24 (2 f_{r\alpha}) + 24 (2 f''_{r\alpha}) = 0$	$24 (2 K_{r\alpha}) + 24 (2 K''_{r\alpha}) = 0$	$24 (2 \sigma''_{r\alpha}) + 24 (2 \sigma''_{r\alpha}) = 0$
$f_{r\alpha} + f''_{r\alpha} = 0$	$K_{r\alpha} = K''_{r\alpha} = 0$	$\sigma_{r\alpha} + \sigma''_{\alpha\alpha} = 0$

Mutual relations between molecular constants—Molecular constants may be grouped under three heads : (1) Stretching and bond-bond interaction constants; (2) Bending and angle-angle interaction constants; and (3) Bond-angle interaction constants.

Groups (2) and (3) are mutually complementary in character, whereas group (1) exhibits the supplementary property as is evident from Table 8.

Table 5, 6 and 7 show the validity of the above relations. It may be remarked that the mutual relationships between the molecular constants are similar to those of molecules belonging to D_{3h} and T_d point groups as was observed by the present authors.[11,12] Algebraic sum of the kinetic constants is purely dependent on the mass of Y atoms and as such, is constant for systems having common Y atoms, but the case is different for the algebraic sums of the GVFF constants and mean square amplitude quantities because the sum in these cases depends on masses as well as frequencies of a_{1g} species. To show that these quantities are structure-dependent, the algebraic sum of the molecular constants can be put in the following form:

$$6 \mu_y \Sigma K_{ij} = \frac{6 \mu_y \Sigma f_{ij}}{\lambda_1} = \frac{6 \Sigma \sigma_{ij}}{\mu_y \Delta_1}$$

$$= 36, \text{ for } XY_6 \text{ type molecules.}$$

It should be noted that since the GVFF constants pertaining to bending, angle-angle interaction and bond-angle interaction constants mutually cancel each other; the energy exchange during the vibration is dominated by the symmetry force constants of a_{1g} species. Further, since the symmetry force constants in this case will be the sum of stretching and bond-bond interactions in which the stretching interaction constant is the greatest, one may conclude that the changes in bond energy will be roughly proportional to f_r. This is also supported by the observation of Yeranos[22] that the bond energy is linearly related to the stretching force constants through ionicity, viz. E (cal/mole) $= K \omega + C = K (X + \theta_f) + C$, where $\omega = 16 (x_m - x_f) + 3{\cdot}5 (x_m - x_f)^2$, x_m and x_f being electronegativities of metals and halogens and θ_f assumes different values for different halides, and ionicity, $\omega = (X + \theta_f)$, is linearly related to stretching force constants.

Acknowledgement

The authors wish to express their sincere thanks to Prof. D Sharma, Vice-Chancellor, Indore University and Dr Y B Singh, Principal, St. Andrew's College, Gorakhpur, for their interest.

References

1. Wilson E B, Decius J C & Cross P C, *Molecular vibrations* (McGraw-Hill, New York), 1955.
2. Thirugnanasambandam P & Srinivasan G J, *Proceedings of the seminar on infrared and Raman spectroscopy* (University of Kerala, Trivandrum), 1964, 179.

3. Thirugnanasambandam P & Srinivasan G J, *J. chem. Phys.*, **50** (1969), 2467.
4. Thirugnanasambandam P & Mohan S, *J. chem. Phys.*, **61** (1949), 470.
5. Thirugnanasambandam P & Mohan S, *Indian J. pure appl. Phys.*, **12** (1974), 206.
6. Thirugnanasambandam P & Mohan S, *Bull. Soc. Chim. (Belg.)*, **84n** (1975), 987.
7. Thirugnanasambandam P & Karunanidhi K, *Indian J. Phys.*, **50** (1976), 527.
8. Sanyal N K, Dixit L, Subramanyam B R & Pandey A N, *Indian J. Phys.*, **47** (1973), 37.
9. Sanyal N K, Ahmad P & Dixit L, *Indian J. pure appl. Phys.*, **12** (1974), 155.
10. Sanyal N K, Dixit L, Ahmad P & Pandey C P, *Indian J. pure appl. Phys.*, **12** (1974), 437.
11. Sarkar P C & Singh G C, *Spectrosc. Lett.*, **10**(5) (1977), 319.
12. Sarkar P C & Singh G C, *Acta Phys. Polon.*, **A53** (1978), 105.
13. Sarkar P C & Singh G C, *Indian J. pure appl. Phys.*, **16** (1978), 1077.
14. Herzberg G, *Infrared and Raman spectra of polyatomic molecules* (D Van Nostrand Co Inc., New Jersey), 1956.
15. Alix A J P, Muller A & Mohan N, *J. molec. Struct.*, **27** (1975), 440.
16. Sarkar P C & Singh G C, *Indian J. Phys.*, **51B** (1977), 380.
17. Ramaswamy K & Muthusubramaniam P, *Indian J. Phys.*, **45** (1971), 477.
18. Thakur S N & Rai D K, *J. molec. Spectrosc.*, **19** (1966), 341.
19. Cyvin S J, Cyvin J B N, Burnvoll J, Anderson B & Stolevic R, *Selected topics in structure chemistry* (Universities Forlaget, Oslo), 1967.
20. Muller A, Kreb B, Cyvin S J, *J. molec., Phys.*, **14** (1968), 491.
21. Nagarajan G, *Bull. Soc. chim. (Belg.)*, **71** (1963), 537.
22. Yeranos W A, *J. chem. Phys.*, **50** (1969), 3670.
23. Sharma D K, Verma U P & Pandey A N, *Indian J. pure appl. Phys.*, **14** (1976), 319.
24. Singh B P, Subramaniam (Mrs) B R, Pandey A N & Sanyal N K, *Indian J. pure appl. Phys.*, **11** (1973), 701.
25. Singh B P, *Studies in molecular force-field and mean amplitudes of vibration of simple molecules*, Ph D thesis, Gorakhpur University, Gorakhpur, 1972.
26. Begum G M & Rutenberg A C, *Inorg. Chem.*, **6** (1967), 2212.
27. Beatie I R, Gilson T, Livingston K, Fawcett V & Ozin G A, *J. chem. Soc.*, **A5** (1967), 712.
28. Schmulbach C D, *Inorg. Chem.*, **4** (1965), 1232.

Indian Journal of Pure & Applied Physics
Vol. 18, July 1980, pp. 524-527

Development of a Horizontal Model of Calculable Cross-Capacitor

R N Dhar, S L Dahake & K Chandra
National Physical Laboratory, New Delhi 110 012

Received 10 *May* 1979

A horizontal model of calculable capacitor, based on the Thompson-Lampard principle and designed and fabricated at the National Physical Laboratory, New Delhi, is described in this paper. The value of capacitance realized from this capacitor is 1 pF, with an overall uncertainty of 2 parts in 10^6. The technique of transferring this value to standard silica dielectric capacitor of 10 pF by using a precision transformer ratio arm bridge is also briefly discussed. The entire capacitance scale from 10^{-6} pF to 10^6 pF is then built up using quartz, air and mica standard capacitors.

1. Introduction

Under the International System, the 'Farad' is defined as the capacitance of a capacitor whose electrical potential is increased by 1 V when a quantity of electricity of 1 coul is supplied to it. In principle, it should be theoretically possible to compute the capacitance of a capacitor from its geometrical dimensions. In earlier days, the traditional guarded ring or guarded cylinder types were used as standard capacitors, the capacitance of which is a function of three geometric dimensions which have to be determined with high degree of accuracy. Since three-dimensional measurements had to be made and each measurement gave rise to some uncertainty, this type of computable capacitor could not serve as a primary standard of capacitance.

In 1956, the famous theorem of Thompson and Lampard[1] was proposed and a calculable capacitor based on this theorem was first developed in Australia.[2] In many standards Laboratories of the world, the unit of capacitance is realized with high degree of accuracy through similar models of calculable cross-capacitors.[3-6] The capacitance is calculated by measuring only one parameter, viz. length. Such calculable cross-capacitors provide the basis of the primary standard. The unit of inductance 'henry' and the unit of resistance 'ohm' are ultimately derived from the unit of capacitance realized through the calculable capacitor.

The National Physical Laboratory (NPL), New Delhi, being the custodian of national standards of physical measurements, undertook the programme of establishing the primary standard of capacitance based on a calculable cross-capacitor. The present paper describes the design features and constructional details of a horizontal model of calculable capacitor. The overall uncertainty in the realization of the unit of capacitance and the technique used for assigning the value to a transfer standard of capacitance have also been discussed.

2. Principle of Calculable Cross-Capacitor

The salient features of the theory of calculable cross-capacitor as given by Lampard[7] are described below.

Consider an infinitely long cylindrical conducting shell of any arbitrary cross-section (Fig. 1), with at least one axis of symmetry (I-I'). It is divided into four segments by two mutually perpendicular planes whose line of intersection is parallel to the axis of the cylinder. If one of the planes contains the line of symmetry (I-I'), then Lampard has shown that the direct cross-capacitance per unit length between opposite sections of the shell in vacuum is given by

$$C = \frac{\epsilon_0 \ln 2}{\pi} \text{ (F/m)} \qquad \ldots(1)$$

where $\epsilon_0 = 1/\mu_0 c^2$, c being the velocity of light in vacuum.

Taking $c = 2{\cdot}997925 \times 10^8$ m/sec and $\mu_0 = 4\pi \times 10^{-7}$ H/m, we get

$$C = 1{\cdot}95354850 \text{ pF/m}$$

However, in practice, the cylindrical shell is always somewhat non-symmetrical and the two cross-capacitances C_1 and C_2 are unequal. In such a case, C_1 and C_2 are related by the expression

$$\exp(-\pi C_1/\epsilon_0) + \exp(-\pi C_2/\epsilon_0) = 1 \qquad \ldots(2)$$

The mean value of the two cross-capacitances $C_m = (C_1 + C_2)/2$ can be obtained from Eq. (2) by a series development with $\Delta C = C_1 - C_2$ and it is given by

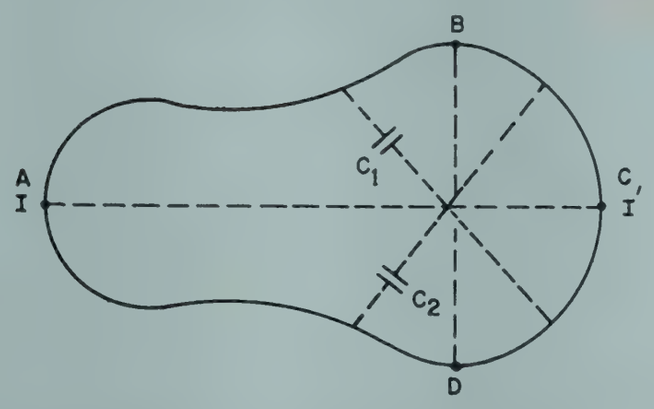

Fig. 1 – Diagrammatic representation of a cross-capacitor having any cross-section

$$C_m = \frac{\epsilon_0 \ln 2}{\pi}\left[1 + \frac{\ln 2}{8}\left(\frac{\Delta C}{C}\right)^2 - \frac{(\ln 2)^3}{192}\left(\frac{\Delta C}{C}\right)^4 + \frac{(\ln 2)^5}{2880}\left(\frac{\Delta C}{C}\right)^6 - \cdots\right] \quad \ldots(3)$$

The terms in bracket involving $\Delta C/C$ show the effect of asymmetry of the cross-capacitor.

When $\Delta C/C < 10^{-3}$, the uncertainty in the value of C_m due to neglect of the correction terms is less than 1 part in 10^7.

As seen from Eq. (3), the shape and dimensions of the cross-section of the capacitor do not enter into the calculation. The capacitance is determined by measuring only one dimension of the capacitor, viz. length, which can be measured with an accuracy of the order of 1 part in 10^7 to 10^8.

3. Design Data and Construction Details

While designing a calculable capacitor based on Thompson Lampard principle, it is important to achieve the equality of the two cross-capacitances C_1 and C_2 within 0·1% to minimize the effect of the correction terms in Eq. (3). This necessitates a high degree of symmetry of the cross-section. Thompson[2] showed that, out of the various alternatives for the shape of the cross-section, an arrangement consisting of four parallel circular cylindrical bars placed at the four corners of a square (Fig. 2a) is most suitable. The four quadrants of the metallic surface of the bars form the symmetrical cylindrical shell as shown in Fig. 2b. The insulating gaps between adjacent surfaces, located in reentrant positions, have negligible effect. Dunn[3] showed that the uncertainty due to gaps as large as 1/12 of the diameter of the bars is less than 1 part in 10^7. The cylindrical bars with circular cross-sections can be fabricated with close dimensional tolerances to ensure the required symmetry of cross-section. Lampard's capacitor is assumed to be infinitely long having the same cross-section throughout. It is, therefore, essential that

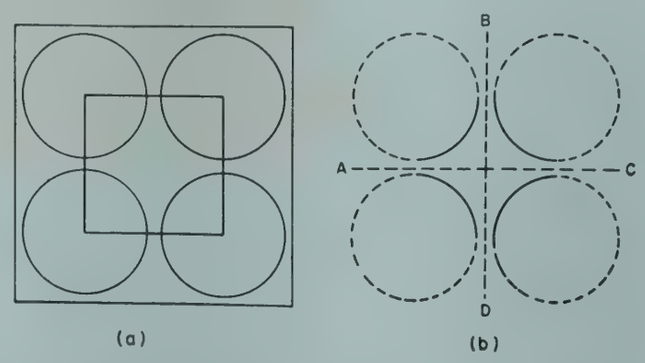

Fig. 2 – Cross-section of a capacitor with four cylindrical electrodes having circular cross-section

the bars should be straight and exactly circular throughout the length. Since any practical capacitor is of finite length, it is necessary that the uncertainty due to the inhomogeneous fringing of the electric field at the ends of the capacitor is eliminated. This is achieved by using split section bars with guard ends as described later.

Dunn has also examined the manner in which the uncertainties in the measured values of capacitance and length vary with the length of a cross-capacitor. He showed that, if the optimum length is kept between 3 and 30 cm, the total uncertainty (for both length and electrical measurements) is least.

The cross-section of the horizontal model of the calculable capacitor developed by us is shown in Fig. 3. It consists of eight cylindrical tool steel bars of circular cross-section. Each bar is 460 mm in length and 22 mm in diameter. These bars are arranged in two rows on a granite surface plate with flatness tolerance within a few micrometres. Each of the five bars of the bottom row rests on a 4 mm thick quartz plate and is separated from the adjacent bar by a 2 mm thick quartz spacer. Bars 4 and 8 have no electrical function; they are used to give mechanical support to the bars in the bottom row with the help of phosphor bronze springs. Bars 1, 2 and 3 in the top row rest on cylindrical quartz

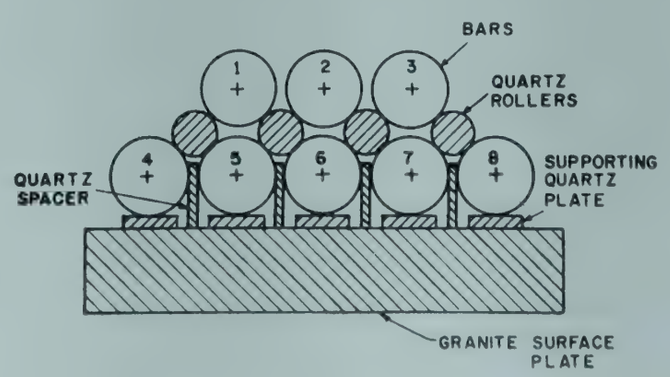

Fig. 3—Cross-section of a horizontal cross-capacitor

rollers of 12 mm diameter placed in the troughs between bars of the bottom row.

From Fig. 3 it is evident that the system consists of two cross-capacitors, one with bars 1, 2, 5 and 6 and the other with bars 2, 3, 6 and 7. If bar 1 is electrically connected to bar 3 and bar 5 to bar 7, the system represents two cross-capacitors in parallel. The capacitance is the same as that of a cross-capacitor consisting of four bars but of double the length.

Bars 2 and 6, generally called the detector bars, consist of five sections A, B, C, D and E as shown in Fig. 4(a). The end sections A and E, each 51 mm long, are insulated from the inner sections B and D by means of 0·3 mm thick mica spacers which are fixed rigidly to them. Sections B and D are also 51 mm long while the central section C is 256 mm long. All the eight bars have the same total length of 460 mm. Dimensions and finishing tolerances of bars and quartz spacers are listed in Table 1.

The outermost sections A and E constitute the guard ends and are grounded. The quartz spacers and rollers are all located within the guard sections so that no solid dielectric appears within the active length of the capacitor. The end sections are drilled throughout their length to provide coaxial connection to the inner active sections B, C and D. The single as well as split section bars are prepared with very close tolerances. The detector bars 2 and 6 can be assembled in two ways: (i) the 256 mm long section C may be placed in between the two 51 mm long sections B and D to give an active length of 358 mm (Fig. 4a) or (ii) it may be fixed to the other end of section E to provide an active length of 102 mm

Table 1—Dimensions of Bars and Spacers Used in the Horizontal Calculable Capacitor

Average diameter of all bars	= 22·2507 mm
Maximum difference in diameter along the length of a bar	= ± 13 μm
Maximum deviation from circularity	= ± 6 μm
Maximum deviation from linearity	= ± 14 μm
Length of central piece C	= 256·0975 mm ± 0·3 μm
Average thickness of supporting quartz plates	= 4·004 mm
Average thickness of quartz spacers	= 2·000 mm
Average diameter of quartz rollers	= 12·050 mm
Length of quartz rollers	= 12 mm
Deviation from circularity of quartz rollers	= ± 1 μm

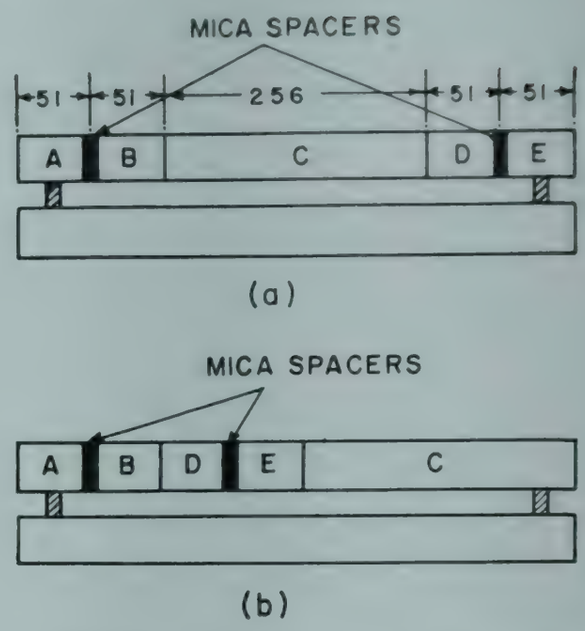

Fig. 4—Diagrammatic representation of the two arrangements of the detector bars in the cross-capacitor

Fig. 5—A view of the cross-capacitor developed at the NPL

(Fig. 4b). The overall length of all sections together remains the same in both the cases. The guard sections are undisturbed during the process. When the active bars are assembled in the two ways as described above, they constitute two cross-capacitors whose effective lengths are 358 mm or 102 mm without any other change in the system. The difference between the capacitance of the cross-capacitor corresponding to these two arrangements of the detector bars as calculated from Eq. (1) comes out to be close to 1 pF. The actual lengths of the sections C of the bars 2 and 6 are measured and corrected for any variation in temperature at which capacitances are compared using the value of the coefficient of thermal expansion of tool steel as 10 ppm/°C. The temperatures of the bars are measured with the help of thermocouples placed at different points along the surface of the bars away from the active length. Readings are taken only when temperature of the whole capacitor is stabilized to within ± 0·1°C. The whole capacitor assembly is placed in a chamber which is evacuated to a pressure of 10^{-2} torr to eliminate any effect due to

variations in the dielectric constant, humidity and pressure of the air. Fig. 5 is a photograph of the calculable capacitor with the vacuum lid removed.

4. Uncertainties in the Calculated Value of Capacitance

The major factors contributing to the uncertainty in the calculated value of capacitance of the calculable capacitor are discussed below.

Uncertainty due to asymmetry of the cross-capacitor—The asymmetry of the cross-capacitor gives rise to an uncertainty which can be estimated from Eq. (3). The first correction term (ln 2)/8 $(\Delta C/C)^2$ is calculated and taken into account. However, the uncertainty due to the second correction term which is of the order of ± 0·1 ppm is still present. The other correction terms are found to be much smaller than 0·1 ppm.

Uncertainty due to temperature variation—The fact that the temperature of the cross-capacitor does not remain constant during the process of measurement gives rise to an uncertainty in the actual length of the bars. The temperature variation of the capacitor is within ± 0·1°C. Taking the temperature coefficient of the bars as 10 ppm/°C, this leads to an uncertainty of about 1 ppm in the computed value of the capacitance.

Uncertainty due to length measurement—The length of the 256 mm long bars is measured with an accuracy of 0·5 ppm. This leads to an uncertainty of about 0·5 ppm in the computed value of the capacitance.

Uncertainty due to permittivity of air—Since the whole capacitor is evacuated to a pressure of less than 10^{-2} torr, the uncertainty due to the permittivity of residual air being different from that of vacuum is less than 0·1 ppm at this pressure.

Total uncertainty—The total uncertainty in the calculated value of the capacitance is the sum of the uncertainties listed above and comes out to be about 2·0 ppm. The value of capacitance realized with the help of this model is 1·000590 pF.

5. Calibration of Transfer Standard against the Calculable Capacitor

An outline of the technique to transfer the value of the calculable capacitor to the 10 pF (silica) capacitor is briefly given below.

First, four 1 pF, temperature-compensated, air dielectric capacitors are compared with the calculable cross-capacitor using precision transformer ratio arm bridge. The average value of these 1 pF capacitors is thus obtained and by comparing these 1 pF capacitors among themselves, the individual values of these capacitors are determined. The 1 pF capacitors are housed in an aluminium enclosure so that their temperatures do not differ by more than 0·1°C during the process of measurement. These capacitors have good short time stability.

The next step is to compare the 10 pF standard capacitor (silica dielectric) with each of these 1 pF capacitors using the same transformer ratio arm bridge. The 10 pF capacitor is maintained in an oil bath with a temperature stability of ± 0·01°C. This capacitor is very stable (± 0·3 ppm/year) and requires calibration once in a year. The accuracy of the calculable capacitor is thus transferred to the 10 pF transfer standard.

6. Setting-up the Scale of Capacitance

For scaling up the value of capacitance, a 100 pF standard capacitor is then compared with the 10 pF transfer standard using the transformer ratio arm bridge. A 1000 pF capacitor could similarly be calibrated against the 100 pF standard and so on. Thus the capacitance can be scaled up to 10^6 pF. Similarly, using standard capacitors of smaller denominations, the capacitance scale could be extended down to 10^{-6} pF.

Acknowledgement

The authors are extremely grateful to Dr A R Verma, Director, NPL, for constant encouragement and permission to publish this paper. Thanks are also due to Dr D Sen and Dr P C Jain for their valuable assistance. The authors also acknowledge the help given by Sarvashri Naib Singh and Ratinder Agarwal in the fabrication of the calculable capacitor.

References

1. Thompson A M & Lampard D G, *Nature, Lond.*, **177** (1956), 888.
2. Thompson A M, *Proc. Instn elect. Engrs*, **106B** (1959), 307.
3. Dunn A F, *Can. J. Phys.*, **42** (1964), 53.
4. Fiebiger A, Fleischhauer K & Klonz M, *Phys. Tech. Ber.*, **PTB-3** (1974), 1-33.
5. Rayner G H, *IEEE Trans.*, **IM-21** (1972), 361.
6. Cutkosky R D, *IEEE Trans.*, **IM-23** (1974), 305.
7. Lampard D G, *Proc. Inst. elect Engrs, Aust.*, **104-C** (1957), 271.

Indian Journal of Pure & Applied Physics
Vol. 18, July 1980, pp. 528-531

Self-Absorption-Free FeI Spectral Lines For Temperature Measurement in the dc Carbon Arc

M A Eid, K M El-Behery & S M Diab
Physics Department, National Research Centre, Cairo, Egypt

Received 25 *April* 1979

The self-absorption behaviour of FeI spectral lines is investigated in the spectrum of free-burning carbon arc in the region between 2440 and 3075 Å. The slope of the working curve, used in emission spectral analysis, is used as an indication of the presence or absence of self-absorption. The results of the investigation lead to selection of self-absorption-free spectral lines suitable for the determination of the excitation temperature in the arc.

1. Introduction

In emission spectral analysis, the temperature of the excitation source is an important quantity. Line intensity, freedom from interference and, in general, the analytical utility of the source are related to the excitation temperature. Different methods have been used for the determination of the excitation temperature from the spectra produced during the analysis. If the source is in a state of local thermal equilibrium, the intensity of a spectral line corresponding to a transition n—m is given by :

$$I_{nm} = \frac{d}{4\pi} A_{nm} \frac{hc}{\lambda_{nm}} N \frac{g_n}{U} \exp(-E_n/kT)$$

where d is the length of the emitting layer, A_{nm} the Einstein transition probability of the line, λ_{nm} the wavelength, h the Planck's constant, c the velocity of light, N the number density of the atoms in the ground state, U the partition function, k the Boltzmann's constant, g_n and E_n the statistical weight and the energy of the upper level respectively and T the excitation temperature.

The temperature T can be obtained using the foregoing equation, from the relative intensity of only two spectral lines. If the two lines belong to the same ionization stage, the partition functions and the number densities of the atoms in the ground state are the same and we get an equation in the form :

$$\frac{I_1}{I_2} = \frac{A_1 g_1 \lambda_2}{A_2 g_2 \lambda_1} \exp\left(\frac{E_1 - E_2}{kT}\right)$$

where indices 1 and 2 refer to the first and the second line respectively.

The accuracy of the temperature determination depends on the accuracy of the values of the transition probabilities A_1 and A_2. Unfortunately in many cases, the uncertainty in the values of the transition probabilities is large and in the ratio, this may cause large errors. Accuracy may be improved by measuring a number of different lines. A plot of log $I\lambda/gA$ against E_n gives a straight line whose slope is proportional to $1/T$. In order to attain high precision, lines of widely differing excitation energies should be employed.

Another important condition which should be satisfied in the spectral lines used for temperature determination, is that they should be free from self-absorption. The presence of self-absorption leads to scattering in the points in the previously mentioned plot and consequently to incorrect temperature values. In general, high temperature values are obtained when self-absorption is present.

Iron spectral lines have been used by a number of investigators for the determination of the excitation temperature of some sources used in emission spectral analysis. De Galan and Winefordner[1] used ten FeI lines for the determination of the excitation temperature of turbulent diffusion flames. These lines lie in the spectral region between 3720 and 3764 Å. The same group of lines has been employed by Rippotoe *et al.*[2] for measuring the excitation temperature in the plume of a dc plasma arc and by Rippotoe and Vickers[3] for the determination of the temperature of a rotating arc plasma jet. Applying these lines for the determination of the excitation temperature of a free-burning carbon arc,

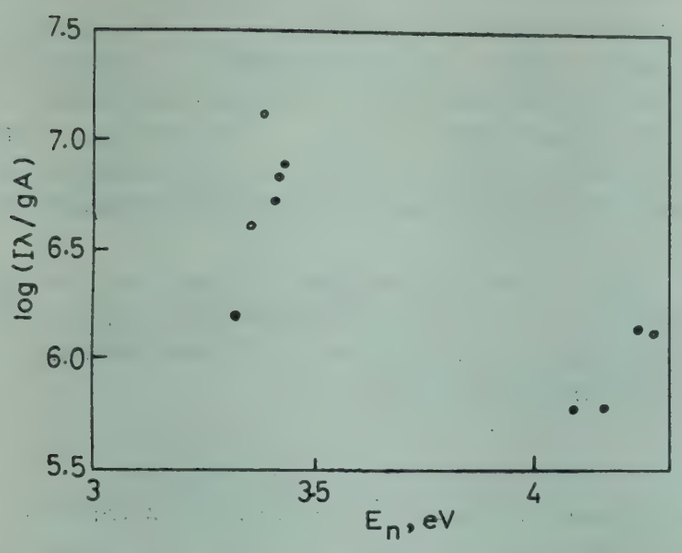

Fig. 1—Plot of log $I\lambda/gA$ versus E_n, showing the scatter in the points, when Fe-lines in the range 3720-3764 Å are used for temperature determination in the dc carbon arc [Based on the procedure of Ref. 1]

we obtained a plot as shown in Fig. 1, in which the points are so widely scattered that no correct temperature value can be assigned to the arc using these lines.

The present work was undertaken to study the self-absorption behaviour of iron spectral lines in the spectrum of the free-burning dc arc, in order to select self-absorption-free Fe-lines suitable for temperature determination. The spectral region investigated lies between 2440 and 3075 Å.

2. Self-Absorption of Spectral Lines

There are different procedures for checking the presence or absence of self-absorption of a spectral line.[4] The method adopted here depends on the basic equation used in spectrochemical analysis. That is the empirical relationship between the concentration C of an element and the intensity I of a spectral line in the source of excitation :

$$I = K\,C^m,$$

where K is a constant which depends on the composition of the material examined and the temperature of the plasma. The equation is based on the assumption that intensity is proportional to concentration. Deviation from this proportionality, primarily that caused by self-absorption, is taken into account by the value of the exponent m. Thus the slope of the plot of log I versus log C, which is commonly referred to as the working curve, serves as an indication of the presence or absence of self-absorption by the atoms in the cooler region of the discharge. Unit slope indicates that self-absorption is absent, while the presence of self-absorption yields m-values less than unity.

3. Experimental Procedure

In the present work a Q24 spectrograph (Carl-Zeiss Jena) was used with a slit width of 10 μm. Its dispersion at 3100 Å is 13 Å/mm. For illumination of the slit, a three-lens system was employed. This system provides an intermediate image so that the middle part of the arc column was always used for illuminating the slit The spectra were recorded on Ilford ordinary photographic plates.

The emulsion was calibrated using a six-step filter attached to the spectrograph slit and homogeneously illuminated by the continuous radiation emitted from the positive crater of a carbon arc whose electrodes are located at right angles to each other. The intensity distribution over the spectrum of the radiation was measured,[5,6] so that relative intensities of spectral lines lying in different regions of the spectrum can be determined.

3.1 Optimal Arcing Conditions

Before constructing the working curves, the various experimental variables influencing the excitation conditions were studied. These variables are mainly those which effect the volatilization of the sample and hence the line intensity. These are the arc current, the shape of the electrodes, the arc gap and the exposure time. The optimal values of these parameters are considered to be those which ensure regular volatilization rate of the sample, reproducible line intensity and the least ratio of background to line intensity. The optimal values of the parameters in the experimental set-up are as follows :

Anode crater wall thickness	0·5 mm
Anode crater internal diameter	3·0 mm
Anode crater depth	4·0 mm
Cathode solid angle	20°
Arc gap	4·0 mm
Arc current	10 A
Exposure time	40 sec

3.2 Working Curves

In this study, the Fe-spectral lines in the spectrum region between 2440 and 3075 Å were considered. The lines which showed spectral interference due to the resolution and the dispersion of the spectrograph were excluded. For the construction of the working curves, electrodes were packed with a mixture of spec pure Fe_2O_3 in graphite powder in concentrations of 40, 20, 10, 5, 2·5 and 1·25% respectively. The electrodes were then arced under the optimal conditions attained previously. The line intensities were corrected for background. The working curves were constructed by plotting log I versus log C for

71 lines. Table 1 gives the obtained values of the slopes (m) of the working curves.

4. Results and Discussion

Fig. 2 shows a plot of log $I\lambda/gA$ versus E_n for the Fe-lines given in Table 1. The gA-values as well as the E_n-values are taken from Corliss and Bozmann.[7] It is obvious that there is a large amount of scatter in the points. This scatter can be interpreted to be due to the self-absorption of the spectral lines. It can also be seen that a straight line can be passed through the points which represent spectral lines whose self-absorption is negligible. These are the spectral lines whose m-values are equal or very nearly equal to unity. These lines are indicated with a were (*) in Table 1. As the value of m decreases, the point gets away from the straight line.

Fig. 3 shows the same plot for the lines whose $m \simeq 1$, i.e. free from self-absorption for an arc current of 10 A. The excitation temperature obtained from this plot is 5130 K.

Table 1—Values of E_n, gA and slopes (m) of linear Plots of log I Versus C for 71 Spectral lines in the Region 2440-3075 Å

λ Å	E_n eV	gA	m	λ Å	E_n eV	gA	m
* 2439·74	7·48	32 00	1·00	2832·44	5·33	9·60	0·68
* 2440·11	7·53	23·00	1·00	2843·63	5.27	2·40	0·91
2443·87	5·93	4·90	0·88	2845·60	5·31	2·00	0·93
2457·60	5·90	17·00	0·70	* 2848·72	5·34	0·49	0·98
2468·88	5·88	13·00	0·74	* 2863·86	4·41	0·15	0·99
2496·53	5·88	13·00	0·75	* 2866·63	5·31	0·73	0·98
2507·90	5·90	9·50	0·82	2869·31	4·37	0·27	0·90
2576·69	5·67	5·90	0·84	2874·17	4·31	0·30	0·91
2584·54	5·65	15·00	0·64	2912·16	4·26	0·53	0·85
2606·82	5·67	9·50	0·78	* 2918·03	7·48	44·00	1·00
2623·53	5·68	9·20	0·80	* 2923·29	7·50	44·00	1·00
2841·65	5·61	3·10	0·91	2929·01	4·28	0·57	0·86
2679·06	5·49	7·20	0·81	2936·90	4·22	2·00	0·64
2689·21	5·52	5·30	0·83	2941·34	4·30	0·39	0·80
* 2706·02	6·98	23·00	0·98	* 2948·43	6 93	14·00	0·99
* 2708·57	7·13	30·00	0·97	2953·94	4·28	1·70	0·67
2711·65	5·49	3·20	0·90	2957·36	4·30	0·96	0·64
2723·58	4·64	4·20	0·61	* 2965·26	4·30	0·54	0·98
2724·96	5·49	3·40	0·90	2969·48	5·03	1·30	0·92
2728·02	5·46	2·30	0·92	2970·10	4·28	0·98	0·73
2733·58	5·39	23·00	0·65	2973·24	4·22	3·00	0·64
2735·48	5·45	10·00	0·77	2981·45	4·21	0·66	0·80
2737·31	4·64	4·20	0·65	2994·43	4·19	2·80	0·61
2743·56	5·48	2·00	0·94	2999·51	4·99	5·20	0·73
2746·98	5·37	12·00	0·64	3000·95	4·22	2·80	0·60
2750·14	4·56	3·50	0·60	3008·14	4·23	2·30	0·64
* 2750·88	6·68	9·10	0·99	3009·57	5·03	4·50	0·83
* 2766·91	5·49	0·84	0·98	3017·63	4·22	0·50	0·89
2772·08	5·33	5·20	0·83	3018·98	5·06	3·10	0·88
2778·22	5·32	4·30	0·85	3020·49	4·19	1·40	0·67
2788·10	5·30	19·00	0·62	3024·03	4·21	0·64	0 84
2797·78	5·34	2·40	0·94	3037·39	4·19	2·30	0·64
2804·52	5·33	4·50	0·86	3057·45	4·91	8·10	0·72
2806·98	5·33	4·70	0·86	3059·09	4·10	2·00	0·64
2813·29	5·32	12·00	0·71	3075·72	4·99	5 00	0·77
2823·28	5·35	15·00	0·69				

* Spectral lines for which plot of log $I\lambda/gA$ versus E_n is linear

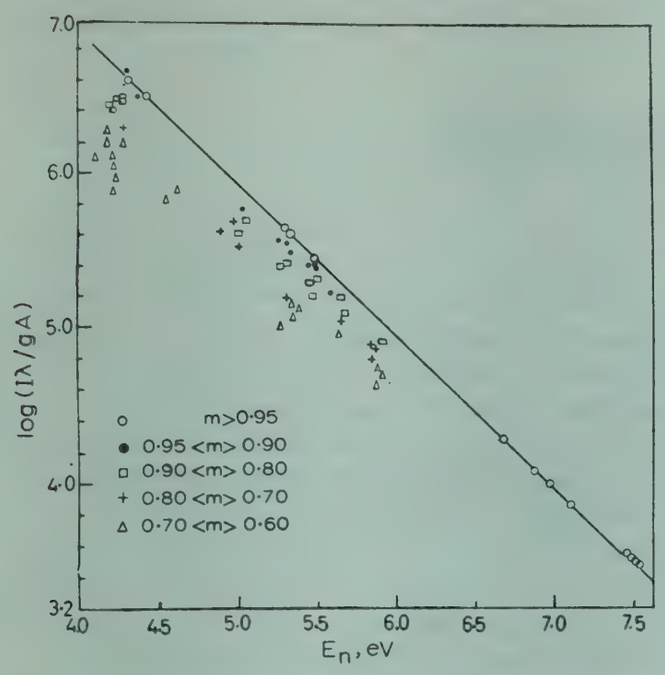

Fig. 2—Plot of log $I\lambda/gA$ versus E_n for 71 lines showing the effect of self-absorption on temperature determination

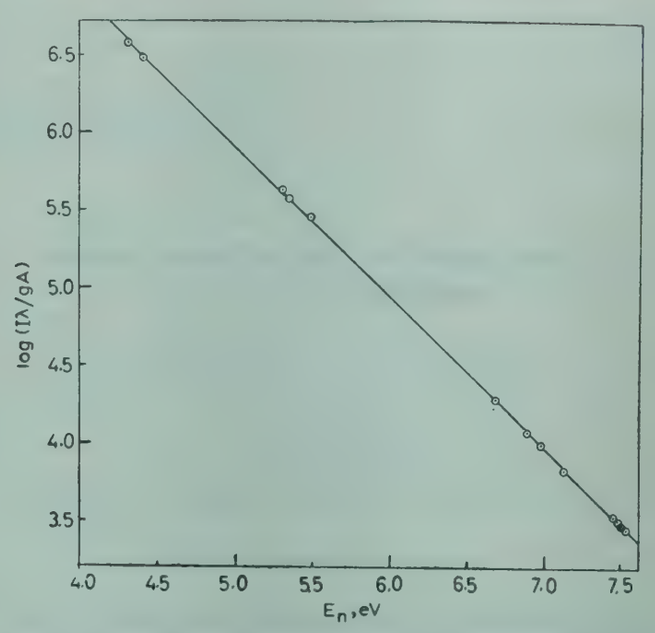

Fig. 3—Temperature determination using self-absorption-free Fe-spectral lines

5. Conclusion

The study of the self-absorption behaviour of the measured Fe-spectral lines has made it possible to select those lines which show negligible self-absorption. The upper energy levels of the selected lines extend from 4·30 to 7·53 eV which ensures accurate temperature determination using these lines. The straight lines which resulted from the plot of log $I\lambda/gA$ versus the excitation energy E_n for these lines proves their applicability for temperature determination. It should be mentioned here that iron is an element which is present in a majority of natu rally occurring samples. Thus while arcing these samples, there is no need to add external thermometric elements which may change the excitation condition in the arc.

References

1. De Galan L & Winefordner J D, *J. Quant. Spectrosc., Radiat. Transfer*, 7 (1967), 703.
2. Rippotoe W E, Jonson E R & Vickers T J, *Anal. Chem.*, 47 (1975), 436.
3. Rippotoe W E & Vickers T J, *Anal. Chem.*, 47 (1975), 2082.
4. Boumans P W J M, *Theory of spectrochemical excitation*, (Hilger & Watts Ltd, London), 1966.
5. Magdeburg H, *Z. Natur.*, 20A (1965), 980.
6. Hattenburg A T, *Appl. Opt.*, 6 (1967), 95.
7. Corliss C H & Bozmann W R, "*Experimental transition probabilities of spectral lines of seventy elements*," N B S Monograph-53 National Bureau of Standards, Washington, 1962.

Communications

I-V Characteristics of Semiconductor-Insulator-Semiconductor Solar Cells

K SEN, B K JAIN & V K BHATNAGAR

D B S College, Dehra Dun

&

V K SRIVASTAVA

Department of Physics, University of Roorkee, Roorkee

Received 6 *December* 1979

The *I-V* characteristics of a SIS (CdS-SiO_2-Si) solar cell are discussed theoretically. The lower forward voltage region is assigned to the recombination current while the high forward voltage region is attributed to the tunnelling current. The theoretical efficiency of the (CdS-SiO_2-Si) solar cell is calculated taking the above considerations into account.

It is well known that the introduction of a thin film of insulating layer between metal and semiconductor (MIS) increases[1] the open circuit voltage (V_{oc}). Further, the presence of a thin insulating film overcomes any mismatching problem between two dissimilar semiconductors.

The V_{oc} in the presence of insulating layer of thickness δ (in Å) increases to $V_{oc\delta}$ given by[1]

$$V_{oc\delta} = V_{oc} + \frac{nKT}{q} \chi_n^{1/2} \delta \qquad ...(1)$$

where χ_n is the tunnelling transmission coefficient (in eV), n the diode quality factor[2] given by

$$n \simeq 1 + \frac{\delta}{\epsilon_i \epsilon_0} q D_{ss} \qquad ...(2)$$

D_{ss} being the surface density of states.

Card and Yang[1] have shown in the case of Au-SiO_2-Si (MIS) structure $V_{oc\delta}$ increases with increase in value of δ upto a certain value ($\sim$20Å) and decreases with further increase in δ. It is also observed by them that the short circuit current (J_{sc}) remains constant for the thickness range in which $V_{oc\delta}$ increases with increase of δ. But when δ has a value above this threshold value, the thin insulating layer acts as a series resistance and degrades the solar cell performance.

The main difference between SIS and MIS structures is that in the metal of the MIS structure continuous energy levels are available while in the semiconductor of the SIS structure the continuity of energy levels is broken by the forbidden energy gap. In MIS and SIS structures, the dark current is, in general, explained on the basis of the thermionic emission process. Ghosh *et al.*[3,4] also considered the possibility of diffusion dominated current, but no well accepted explanation has so far been given. Keeping this in mind we have discussed the mechanism for the dark current and hence the efficiency of such cells.

Dark current—Forward dark current can be considered as flowing due to different mechanisms taking part separately or simultaneously in the system. This dark current in MIS and SIS structures can be written as sum of two exponentials as

$$I_d = I_{01} \left[\exp\left(\frac{q\,v}{n_1\,kT}\right) - 1 \right] + I_{02} \left[\exp\left(\frac{q\,v}{n_2\,kT}\right) - 1 \right] \qquad ..(3)$$

In different samples of SnO_2-SiO_2-Si (SIS) cells, Ghosh *et al.*[4] found that in the lower voltage range (< 0·4 V) the diode quality factor (n_2) varies between 2 and 3 with $I_{01} \approx 10^{-6}$ A/cm^2.

But at the higher voltages, value I_d is considerably influenced by the 2nd exponential term. At voltages greater than 0·4 V, $n_2 \approx 1$ and I_2 has values in the range 10^{-8}-10^{-11} A/cm^2. These authors[4] explained the dark current in the lower voltage range as tunnelling dominated while at the high voltage range as diffusion dominated.

Since the energy level diagram of [CdS-SiO_2-Si] shown in Fig. 1 (a) is similar to that of the [SnO_2-SiO_2-Si] structure (except for difference in the value of energy gaps of CdS and SnO_2) we expect and consider the dark current and diode quality factor to be of the same order. In such structures, the probability of tunnelling at lower forward voltages would be small in comparison to the tunnelling probability at a higher forward voltage, hence, one can expect that in the former case processes other than tunnelling should be dominating. So we attribute the possible value of reverse saturation current ($\sim 10^{-6}$ A/cm^2) as due to recombination at the depletion region corresponding to the diode quality factor of $n \simeq 2$. The saturation recombination current can be approximately written as[5]

$$I_{01} = \frac{q n_i W_n}{(\tau_p + \tau_n)} \qquad ...(4)$$

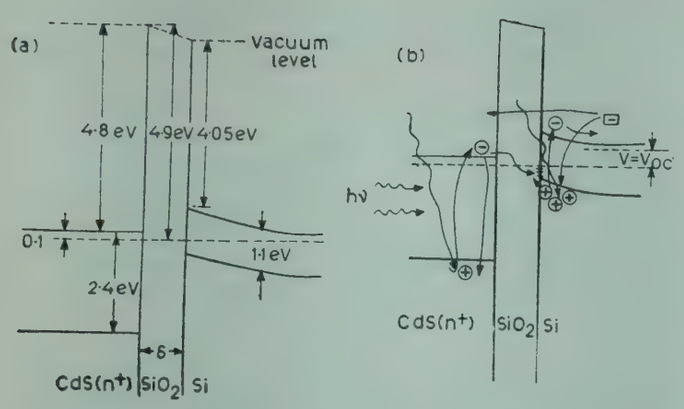

Fig. 1 (a)—Energy level diagram under equilibrium for [CdS (n^+)-SiO_2-Si] solar cell (b) level diagram under energy illumination [+ and − indicate holes and electrons respectively, ○ Refers to photo generated carriers □-refers to dark carriers under forward bias and →denotes their path]

where W_n is the width of the n region, τ_n and τ_p are respectively the electron and hole lifetimes and n_i the carrier density in Si. This recombination current is of the order 10^{-6} A/cm^2 and is in agreement with the reverse saturation current observed by Ghosh *et al.*[4]

At higher voltage ranges (> 0·4V), we consider the tunnelling mechanism to switch-in as the dominating current flow mechanism. The dark current can be written as[6]

$$I_d = A^* T^2 \exp\{-\phi_B/kT\}\left[\exp\left(\frac{qV}{kT}\right)-1\right] \quad ..(5)$$

where A^* is the modified Richardson constant and ϕ_B is the barrier height.

At the forward voltage of interest ($V_{oc} \simeq V_{mp}$) the photo holes at the Si-SiO_2 notch may not recombine with the photo electrons from CdS side, because these electrons will be repelled by the forward voltage thereby forcing the photo holes to recombine with the forward dark electrons from the Si conduction band. Further, this large forward voltage will assist the electrons to tunnel the insulating layer and hence we can rewrite the dark current equation [Eq. (5)] at $V > 0{\cdot}4$V as:

$$I_d = A^* T^2 \exp\{\phi_B/kT\}.\, T_n\left[\exp\left(\frac{qV}{kT}\right)-1\right] \quad ...(6)$$

$$\text{Or} \quad I_d \simeq I_{02} \exp\left(\frac{qV}{kT}\right) \quad ...(7)$$

where T_n is the tunnelling transmission probability given by $\exp\{-\chi_n^{1/2}.\,\delta\}$

Card and Yang[1] have observed a maximum value of $V_{oc} \simeq 0{\cdot}2$ V for $\delta \simeq 20$ Å in Au-SiO_2-Si cell. Here in the present structure (CdS-SiO_2-Si) we assume a reasonable maximum increment of 0·25 V to the value V_{oc} of the MIS structure due to the presence of semiconducting SiO_2 film. Thus with $n \simeq 1$ as obtained by Ghosh *et al.*[4]

$$\frac{kT\,\chi_n^{1/2}}{q}\cdot\delta = 0{\cdot}25\text{ V} \quad ...(8)$$

$$\text{or } \exp\left(-\chi_n^{1/2}\,\delta\right) \simeq 10^{-5} \quad ...(9)$$

as $kT/q \simeq 1/40$.

According to Eq. (1) lower increments to V_{oc} are expected for lower values of δ. Thus we can write the tunnelling transmission probability (T_n) to vary between 1 and 10^{-5} for value of δ in the range 0—20 Å.

Using $A^* = 264$ A/cm/K^2, $\phi_B = 0{\cdot}8$ eV, $T = 300$K and T_n varying between 10^{-2} and 10^{-5}, I_{02} varies between 10^{-8} and 10^{-11} A/cm^2. This is again in agreement with the experimental results of Ghosh *et al.*[4] in this voltage range.

Thus the total dark current in the whole voltage range can be considered as due to two mechanisms, viz. (i) recombination dominating at the lower voltage ranges and (ii) tunnelling dominating at higher voltage ranges.

Photo current—The photo electron produced in Si by the photons of energy 1·1 eV $< h\nu <$ 2·4 eV are swept by the built-in field and collected; while the photo holes get accumulated at the Si-SiO_2 notch [Fig. 1b]. These holes at low photo voltage can be said to recombine with the photo electrons at CdS produced by photons of $h\nu > 2{\cdot}4$ eV, through the interfacial states, thereby contributing to photo current. At the photo voltage of interest $V_{mp} \simeq V_{oc}$ where V_{mp} is the voltage at maximum power point, the holes at the Si notch may not contribute anything to the photo current.

The photo current can be calculated analytically (AM1) by Devos[7] approach. Accordingly

$$P(\lambda) = P_0\,[e^{-\lambda/\lambda_1} - Q_0\, e^{-\lambda/\lambda_2}] \text{ for } \lambda \geqslant \lambda_0 \quad ...(10)$$

$$P(\lambda) = 0 \qquad \text{for } \lambda \leqslant \lambda_0 \quad (11)$$

$$\lambda_0 = \frac{\lambda_1\,\lambda_2}{(\lambda_1\,\lambda_2)}\ln Q_0 \quad ...(12)$$

where, the symbols have the usual meaning.

$P_0 = 3{\cdot}82\times10^9$ W/m^3; $Q_0 = 120$; $\lambda_1 = 5{\cdot}90\times10^{-7}$m; $\lambda_2 = 0{\cdot}630\times10^{-7}$ m.

$$\text{The incident power } P_{in} = \int_0^\infty P(\lambda)\,d\lambda = 1136\text{ W/m}^2 \quad ...(13)$$

From Eqs (10)-(13) we may write the maximum photo current as

$$J_{ph} = \frac{\mu_e q}{\mu_e + \mu_h hc} \int P(\lambda)\, \lambda\, d\lambda = 285 \times 10^{-4}\ \text{A/cm}^2 \qquad \ldots(14)$$

where μ_e and μ_h are respectively the electron and hole mobilities.

The limits of integration in Eq. (14) will be λ values corresponding to $E_g = 1{\cdot}1$ eV ($\lambda = 1{\cdot}1 \times 10^{-6}$m) and $E_g = 2{\cdot}4$ eV ($\lambda = 0{\cdot}5 \times 10^{-6}$ m).

Open circuit voltage—At open circuit conditions, the total current J in the circuit is zero and $J_{ph} = J_{sc}$ the short circuit current

$$J = I_d - J_{ph} = 0 \qquad \ldots(15)$$

from Eq. (7)

$$I_d = J_{sc} = I_{02} \left[\exp\left(\frac{q\, V_{oc}}{kT} \right) - 1 \right] \qquad \ldots(16)$$

$$\text{or}\quad V_{oc} \approx \frac{kT}{q} \ln \left[\frac{J_{sc}}{I_{02}} \right] \qquad \ldots(17)$$

Fill factor—The fill factor (FF) is defined by

$$\text{FF} = \frac{J_{mp}\, V_{mp}}{J_{sc}\, V_{oc}}$$

where J_{mp} and V_{mp} are respectively current and voltage at maximum power point. Assuming $V_{mp} \simeq V_{oc}$, FF can be written as[4]

$$\text{FF} = \left[1 - \frac{1}{q\, V_{oc}/kT} \right] \left[1 - \frac{\ln (q\, V_{oc}/kT)}{q\, V_{oc}/kT} \right] \qquad \ldots(18)$$

Efficiency—Knowing FF, V_{oc}, J_{sc} and the incident power, one can calculate the efficiency (η) of the cell as

$$\eta = \frac{V_{oc}\, \text{FF}\, J_{sc}}{P_{in}} \qquad \ldots(19)$$

Calculations are made for different values of I_{02} varying between 10^{-6} and 10^{-11} A/cm^2 corresponding to the values of tunnelling transmission probability varying between 1 and 10^{-5}. Fig. 2 shows the variation of η, V_{oc} and FF with T_n for CdS-SiO_2-Si structure solar cell.

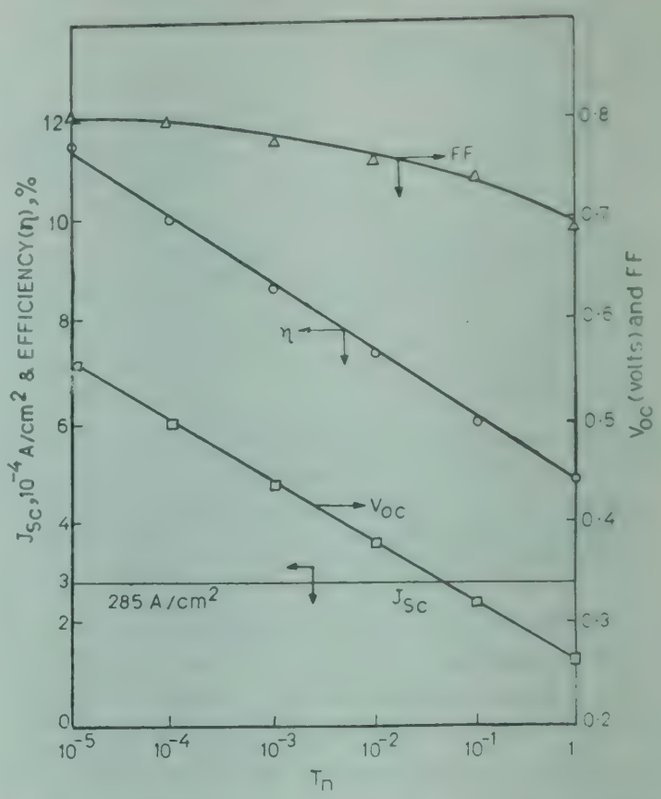

Fig. 2—Variation of η, V_{oc}, FF, and J_{sc} with tunnelling transmission coefficient (T_n) for (CdS-SiO_2-Si) solar cell

In the considered structure at the lower voltage region, the recombination current dominates while at the higher voltage region ($> 0{\cdot}4$V) the current is tunnelling dominated. These considerations lead to the reverse saturation current in the voltage range of interest ($V_{oc} \simeq V_{mp}$), varying between 10^{-8} and 10^{-11} A/cm^2 as observed by Ghosh *et al.*[4] Further the theoretical efficiency on these grounds is also in close agreement with the experimentally achievable efficiency.[4]

References

1. Card H C & Yang E S, *Appl. Phys. Lett.*, 29 (1976), 51.
2. Card H C & Rhodrick E H, *J. Phys.*, D4 (1971), 1589.
3. Ghosh A K, Fishman C & Feng T, *J. appl. Phys.*, 50 (5) (1979), 3454.
4. Ghosh A K, Fishman C & Feng T, *J. appl. Phys.*, 49 (6) (1978), 3490.
5. Fossum F G & Burgess E L, *Appl. Phys. Lett.*, 33 (3) (1978), 238.
6. Sze S M, *Physics of semiconductor devices* (Wiley-Eastern, New Delhi) 1979.
7. Devos A, *Energy conversion*, 16 (1976), 67.

Notes

On Sarma & Rao's Relation for τ for Binary Mixtures of Polar Liquids

B B Swain

Department of Physics, Ravenshaw College
Cuttack 753 003

Received 20 *March* 1979; *revised received* 13 *August* 1979

The empirical relation of Sarma and Rao for τ [*Aust. J. Phys.*, 27 (1974), 87], when applied to binary mixtures of polar liquids, viz. (a) methanol with (i) toluene (ii) aniline and (iii) *N*-butanol; and (b) *N*-butanol with (i) toluene (ii) aniline and (iii) methanol, has been found not applicable in the case of *N*-butanol where τ is governed by a distribution parameter.

Schallamach[1] observed that whereas a binary mixture of polar liquids having both components either associated or unassociated is homogeneous and has a single relaxation time, the mixture with one component associated and another unassociated shows a distribution of relaxation times.

Sarma and Rao[2] proposed an empirical relation to evaluate the dielectric relaxation time of polar liquids using a single microwave frequency instead of the Cole-Cole relation requiring measurements at a number of frequencies. One of the liquids studied by them was methyl alcohol, a highly lossy associated liquid. To evaluate the relaxation time of a mixture (methyl alcohol and benzene); they used the relation, $\tau=\omega^{-1}(\epsilon_s-\epsilon')/\epsilon''$, where ϵ' is the dielectric constant, ϵ'' the loss factor, ϵ_s the static dielectric constant, and $\omega=2\pi f$, f being the microwave frequency.

Plotting a graph between log $CT\tau$ and $(CT)^{-1}$ for different values of C, where C is the volume fraction of the polar liquid in the mixture, and T the temperature, a straight line was obtained for $C\geqslant 0{\cdot}5$ and extrapolating the graph to $C=1$ the relaxation time of the pure polar solute was determined.

In a preliminary investigation, we have attempted to examine the applicability of this method to binary mixtures of polar liquids and also to assess Schallamach's observation in this context.

The microwave frequency used was 9·725 GHz. ϵ_s was determined at 5 MHz. The chemicals used were of AnalaR grade. The mixtures studied were methanol with (i) toluene, a low loss liquid; (ii) aniline, a liquid with medium loss; and (iii) *N*-butyl alcohol, which also has medium loss but is associated unlike the first two liquids.

Table 1—Values of τ at 298 K and Slope of Straight Lines

Solvent	$\tau\times10^{12}$ sec	Slope of straight line	Viscosity of Solvent* cp
Toluene	53·68	69·1	0·586
Aniline	50·79	120·0	4·40
N-Butanol	56·03	38·52	2·95

*At 20°C, taken from the American Institute of Physics Handbook

For all mixtures, the plots of log $CT\tau$ against $(CT)^{-1}$ gave straight lines for $C\geqslant 0{\cdot}4$. The value of τ for pure methanol was determined by extrapolation of the straight line to $C=1$ for each mixture. These values, along with the slope of each straight line and the viscosity of the corresponding solvent are given in Table 1.

The values of relaxation time thus determined agree well with the reported value[3] of $53{\cdot}0\times10^{-12}$ sec at 298 K within the limits of experimental error. Therefore, the empirical relation given by Sarma and Rao is perhaps applicable to polar-polar mixtures with varying values of viscosity and dielectric loss. However, the linear plots yield different slopes for different solvents, leading to varying values of enthalpy which have no apparent correlation with the viscosity of the solvent as suggested by Sarma and Rao.

The straight line plots leading to the same value of τ show that the mixtures are characterized by a single relaxation time, though two of the three mixtures studied are associated-nonassociated and only one is associated-associated. This deviates from the Schallamach's observation.

Secondly, we have attempted to evaluate the relaxation times of *N*-butyl alcohol, taking carbon tetrachloride, toluene, aniline and methanol as solvents. The values of τ obtained are much lower than those of the reported values.[3] These results show that the empirical method of Sarma and Rao is not applicable to the case where the relaxation time is governed by a distribution parameter.

To test the generalizability of these observations, further investigations are in progress.

References

1. Schallamach A, *Trans. Faraday Soc.*, 42A (1946), 180.
2. Sarma B S & Rao V V, *Aust. J. Phys.*, 27 (1974), 87.
3. Syamalamba K & Premswarup D, *Indian J. pure appl. Phys.*, **3** (1965), 390.

Linear Potential & Phonons in Aluminium

K S Sharma* & C M Kachhava

Department of Physics, University of Rajasthan
Jaipur 302 004

Received 8 *March* 1979; *revised received* 18 *June* 1979

The phonon frequencies, binding energy, compressibility, elastic constants and energy band gap of metallic Al have been worked out using a simple one-parameter local potential which gave encouraging results earlier in the case of Na. The calculated values show a good accord with the experimental data.

A number of phonon frequency calculations for Al exist in literature along with some recent publications based on the use of the local potentials.[1-4] Some most outstanding calculations were performed by Coulthard,[5] Williams and Appapillai[6] for the optimized Heine-Abarenkov-Shaw nonlocal potential[7] and by Hafner and Schmuck,[8] and Hafner[9] on the basis of Harrison's first principle theory. Although the results of Coulthard[5] are the best among the nonlocal pseudopotential calculations, yet the local potentials have yielded a varied degree of success. The purpose of the present investigation is to report calculations on the modified version of Ashcroft's potential, which has been found to yield encouraging results for phonon frequencies when applied to metallic sodium.[10]

The new model potential, which is a modified form of Ashcroft's potential in as much as we assume it to vary linearly in the core region, is of the form:

$$V(r) = -c\,r \qquad r \leqslant R_M$$
$$= -\frac{z\,e^2}{r} \qquad r \geqslant R_M \qquad \ldots(1)$$

where e is the electronic charge, z the valence of the metal, R_M the effective core radius (to be treated as a parameter), and c a constant. The condition of continuity of the potential at $r = R_M$ provides

$$c = \frac{z\,e^2}{R_M{}^2}.$$

The momentum space version of the potential is given, in rydbergs, by

$$V(q) = -\frac{16\,\pi\,z}{\Omega_0\,R_M\,q^3}\left[\sin q\,R_M - \frac{1}{q\,R_M}(1-\cos q\,R_M)\right] \qquad \ldots(2)$$

where Ω_0 represents the atomic volume. To produce the screened form factors we use dielectric screening as proposed by Vashistha and Singwi.[11]

The value of potential parameter determined for a best overall fit of the phonon spectra is found to be $R_M = 1{\cdot}6$ au. The phonon frequencies along the three symmetry directions, calculated for this value of R_M, have been displayed in Fig. 1 along with the experimental data of Stedman and Nilsson.[12] It may be observed that the agreement with the experiment is excellent for [111] longitudinal, [111] transverse and [110] longitudinal branches; the respective average absolute percentage deviations (AAPD) being 1·7, 2·0 and 2·8. The agreement for [110] transverse branches is also encouraging, the AAPD being 4·0 and 4·5 respectively for T_1 and T_2 branches. For wave propagation along [100] direction, AAPD of 4·5 and 8·4 are observed for longitudinal and transverse branches respectively, showing an overall good agreement with the experimental data. It is gratifying to note that these deviations are of the order of those obtained by Prasad and Srivastava,[3] using a better fittable, two-parameter potential of Krasko and Gurskii. A comparison with the results of Gupta and Tripathi,[1] based on their two parameter potential further reveals that the present simple potential is capable of showing a better accord with the experimental phonon spectra along [110] direction. The unphysical kinks present in the phonon spectra obtained by Wallace[2] have now been smoothened out, showing that the present potential is less singular as compared to Harrison's potential. It may also be observed that the results from the present potential show a better accord of the phonon frequencies for [111] longitudinal branch; the overall agreement with the experimental data is as good as obtained by kachhava[4] on the basis of Ashcroft potential, except for [100] transverse branch for which the calculated frequencies are higher by a few per cent.

The calculated values of binding energy, compressibility and elastic constants are given in Table 1 along with the experimental data. Table 1 also contains theoretical values of elastic constants as obtained by Kachhava[4] on the basis of Ashcroft's potential. We have also reported the values of binding energy and compressibility on the basis of the parameters

* On leave from Maharani Shri Jaya College Bharatpur 321 001

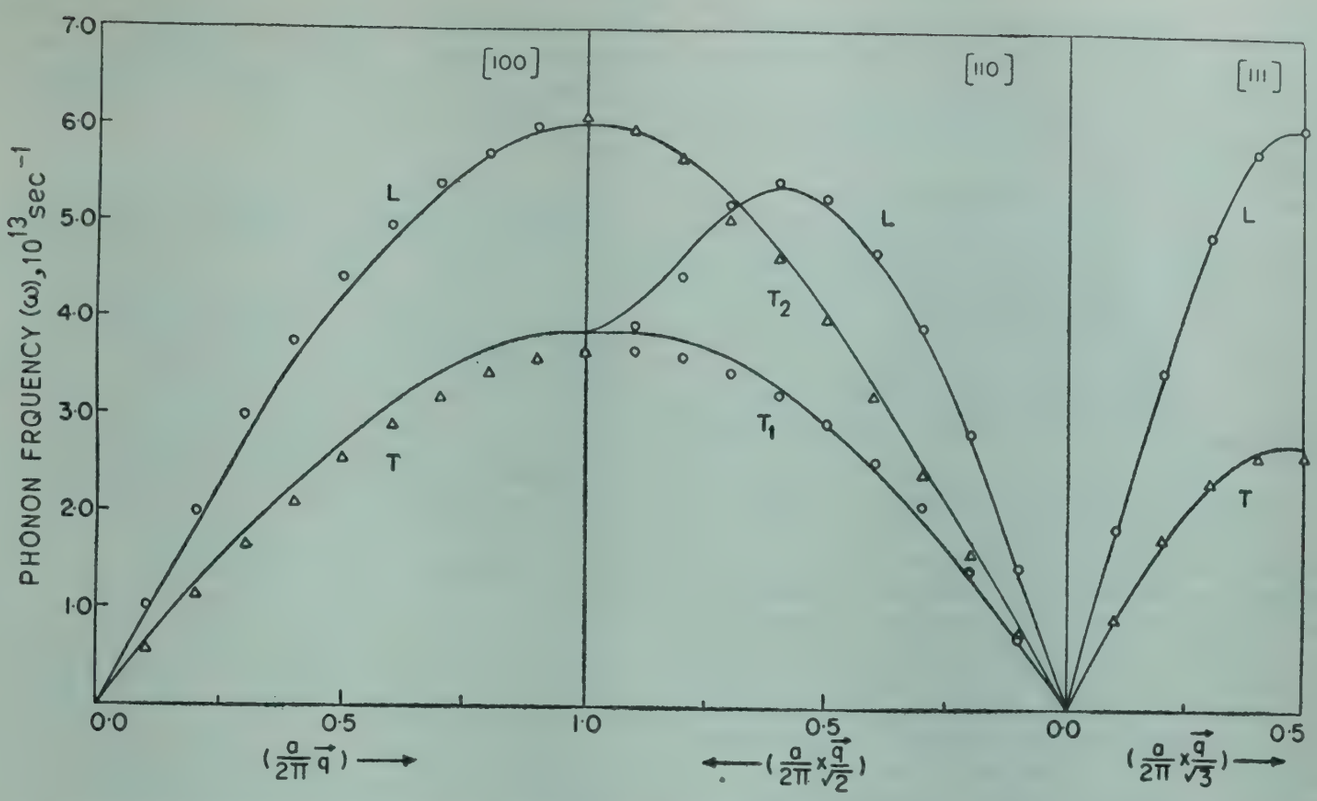

Fig. 1—Phonon frequencies of Al calculated with R_M=1·6 au along 3 symmetry directions [—, calc. values; ○, Δ exptl. values from Ref. 12]

Table 1—Binding Energy ($-U_0$, rydberg/at,) Compressibility (Ω_{0K} rydberg/at) and Elastic Constants in rydberg/au^3 of Aluminium

	Present work	Ashcroft potential	Exptl. val.	
$-U_0$	4·26	4·31	4·16	(Ref. 13)
Ω_{0K}	0·516	0·703	0·546	(Ref. 13)
c_{11}	6·25	4·56	7·26	(Ref. 14)
c_{12}	3·03	1·51	4 13	(Ref. 14)
c_{44}	2·91	2·50	1·92	(Ref. 14)

evaluated from phonon frequencies by Kachhava.[4] An inspection of Table 1 reveals that there is a satisfactory accord between the two sets of theoretical values and the experimental data. The linear potential form is capable of improving upon the results of various properties, except for c_{44} obtained on the basis of Ashcroft potential. This observation lends support to our approach of modifying the form of Ashcroft's potential in the core region, and justifies in an appropriate way the procedure which we have followed.

As a final test of the potential, we determined energy band gap values at the symmetry point W and obtained the values 0·0253, 0·0501 and 0·0754 rydbergs which are comparable with the values of 0·043, 0·104 and 0·147 rydbergs respectively predicted by Segall.[15]

Thus, we may conclude that the proposed potential could be successfully applied for the description of phonon dispersion and other allied crystalline properties of simple metals and holds good prospects for its application to relatively complex metals. The linear potential calculations on Pb, in progress, are encouraging and will be published in due course.

The authors express their deep sense of gratitude to Prof. T Toya, Hokkaido University, Japan for continual encouragement. One of the authors (KSS) is also thankful to the University Grants Commission, New Delhi for providing a teacher-fellowship and to the Director, Computer Centre, Aligarh Muslim University, Aligarh for extending the computer facilities required during this year.

References

1. Gupta H C & Tripathi B B, *Phys. Rev.*, **B2** (1970), 248.
2. Wallace D C, *Phys. Rev.*, **187** (1969), 991.
3. Prasad B & Srivastava R S, *Physics Lett.*, **A38** (1972), 527.
4. Kachhava C M, *Physica*, **65** (1973), 63.
5. Coulthard M A, *J. Phys.*, **C3** (1970), 820.
6. Williams A R & Appapillai M, *J. Phys.*, **F 3** (1973), 772, 759.
7. Shaw R W, *Phys. Rev.*, **174** (1968), 769.
8. Hafner J & Schmuck P, *Phys. Rev.*, **B9** (1974), 4138.
9. Hafner J, *Z. Phys.*, **B22** (1975), 351.
10. Sharma K S & Kachhava C M, *Solid St. Commun.*, **30** (1979), 749 in press.

11. Vashistha P & Singwi K S, *Phys. Rev.*, B6 (1972), 875.
12. Stedman R & Nilsson G, *Phys. Rev.*, 145 (1966), 492.
13. Kachhava C M, *Physics Lett.*, 39A (1972), 265.
14. Schmuck R E & Smith S C, *J. Phys. Chem. Solids*, 9 (1959), 100.
15. Segall B, *Phys. Rev.*, 124 (1961), 1797.

Frequency Moments & Viscosities of Liquid Rubidium

N S Saxena & Nilima Lodha

Department of Physics, University of Rajasthan, Jaipur 4

Received 19 *April* 1979; *revised received* 5 *July* 1979

Simplified numerical calculations are presented for the second and fourth frequency moments of the spectral functions of both the longitudinal and transverse current correlation for liquid rubidium. Model potential used is of D L Price [*Phys. Rev.*, A4 (1974), 358] and static pair-correlation function is that obtained by A Rahman [*Phys. Rev.*, A4 (1974), 1667] from the molecular dynamics calculations. A memory function approach is used to calculate the longitudinal and shear viscosities of liquid rubidium at its melting point. The results are in good agreement with the experimental values.

In earlier papers[1-3] attempts have been made to estimate the frequency moments for liquid argon. Recently, Bansal[4] has performed numerical calculations for the lower order frequency moments of the spectral functions of the longitudinal and transverse current correlation for liquid sodium and aluminium using Schiffs[5] model potential and corresponding static pair correlation function. Since his results for longitudinal and shear viscosities are of the right order of magnitude, using the memory function formalism, we thought it reasonable to carry out similar calculations in liquid rubidium, which exhibited good results[6] for the high frequency longitudinal or transverse phonon modes.

Results in the long wavelength limit for the frequency moments of the spectral functions of longitudinal as well as transverse current correlation in liquid rubidium have been presented in this note. The model potential and pair-correlation function used in these calculations are due to Price[7] and Rahman[8] respectively. These results have been used to estimate the longitudinal and shear viscosities in liquid rubidium employing memory function formalism. The modified exponential[3] and Gaussian[2] type of memory functions have been used in the calculation of these viscosities.

The expressions for the low-order frequency moments of the spectral functions of both longitudinal and transverse current correlations are well known. For the fourth frequency moment we use the end results obtained by Forster[1] in the long wavelength limit. Results for the various moments at density $0{\cdot}0102 \times 10^{24}$ cm^{-3} and at temperature $T = 312$ K are

$$\mathrm{Lt}\ q\to 0\ \frac{\langle \omega_e^2 \rangle}{q^2} = 0{\cdot}490 \times 10^{10}\ \mathrm{cm^2\ sec^{-4}} \qquad \ldots(1a)$$

$$\mathrm{Lt}\ q\to 0\ \frac{\langle \omega_e^4 \rangle}{q^2} = 1{\cdot}50 \times 10^{34}\ \mathrm{cm^2\ sec^{-4}} \qquad \ldots(1b)$$

$$\mathrm{Lt}\ q\to 0\ \frac{\langle \omega_t^2 \rangle}{q^2} = 0{\cdot}250 \times 10^{10}\ \mathrm{cm^2\ sec^{-2}} \qquad \ldots(2a)$$

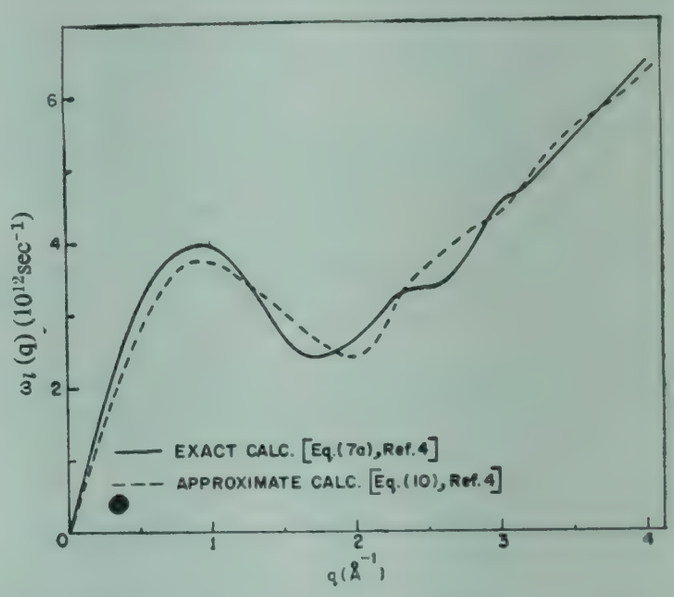

Fig. 1—Plot of longitudinal phonon frequency mode $\omega_l(q)$ against q.

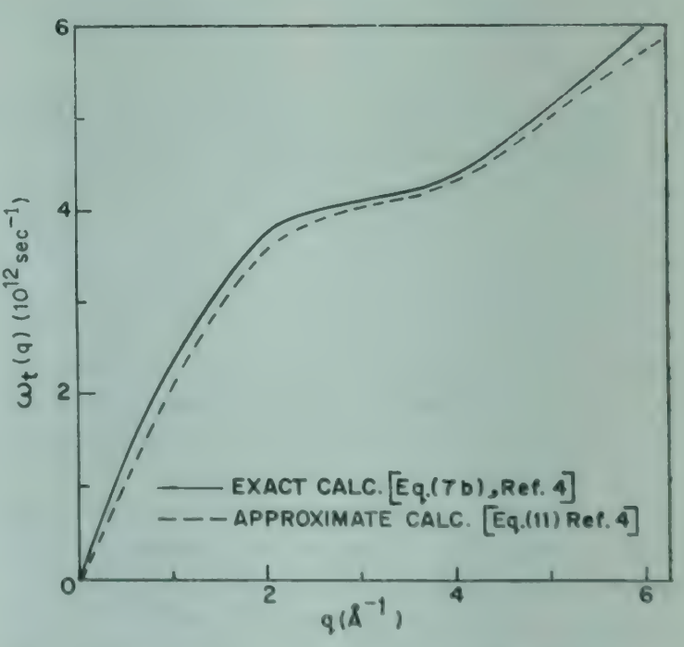

Fig. 2—Plot of transverse phonon frequency mode $\omega_t(q)$ against q

$$\text{Lt } q \to 0 \; \frac{\langle \omega_t^4 \rangle}{q^2} = 0{\cdot}390 \times 10^{34} \text{ cm}^2 \text{ sec}^{-4} \qquad \ldots(2b)$$

Results for $\omega_l(q)$ and $\omega_t(q)$ as a function of q have been presented in Figs. 1 and 2. For these calculations, use is made of the equations of Ref. 4. An independent estimate of $\omega_l(q)$ and $\omega_t(q)$ has also been made from Eqs. (10) and (11) of Ref. 4, using the argument that the product of static pair correlation function and second derivative of the interatomic potential is peaked near to the hard-core radius. Model potential due to Price for liquid rubidium gives $\omega_E = 1{\cdot}03 \times 10^{12}$ sec^{-1}. The maximum frequency as calculated from Debye temperature $\theta_D = 55{\cdot}5$ K for crystalline rubidium comes out to be $1{\cdot}156 \times 10^{12}$ sec^{-1} which is nearly equal to that obtained from the model potential of Price. The results for $\omega_l(q)$ and $\omega_t(q)$ for liquid rubidium with $\omega_E = 1{\cdot}03 \times 10^{12}$ sec^{-1} and $\sigma = 2{\cdot}15$ Å do not differ appreciably from those obtained by exact integration (Eqs. 7a & 7b) of Ref. 4. The slope of $\omega_l(q)$ at $q = 0$ comes out to be $7{\cdot}0 \times 10^4$ cm sec^{-1} from full curve and $6{\cdot}0 \times 10^4$ cm sec^{-1} from the dashed curve. Also the slope of $\omega_t(q)$ at $q = 0$ is $2{\cdot}5 \times 10^4$ cm sec^{-1} from the full curve and $2{\cdot}0 \times 10^4$ cm sec^{-1} from the dashed curve. Thus it appears that the results obtained using Eqs. 10a and 10b of Ref. 4 are good representatives of the actual curve.

Using the modified exponential[3] type and Gaussian[2] function, the results for longitudinal and shear viscosities together with relaxation times $\tau(0)$, $\tau_{gl}(0)$ and $\tau_{gt}(0)$ which are obtained from the memory function formalism are given in Table 1. Subscript g in various results stands for Gaussian. It is clear from all the equations of Ref. 4 in use that a change in the zero wavenumber limit of the static structure factor [$S(0)$] will affect the results of both the longitudinal as well as shear viscosities in the analysis of Gaskell. But in the Gaussian memory function formalism only longitudinal viscosity is affected. This is due to the fact thot Gaskell's analysis uses the same relaxation time for the calculation of both longitudinal and shear viscosities whereas Gaussian memory function formalism uses different relaxation times.

The value of the ratio of specific heats as calculated from the experimental data comes out to be 1·15, which has been used in the present calculations. The results of course, depend upon the value of $S(0)$. We have used $S(0) = 0{\cdot}04$ obtained by Rahman from molecular dynamics calculations.[8] This value of $S(0)$ is larger than the value obtained from the experimentally determined isothermal compressibility, which is equal to 0·02. To see the sensitivity of the results to $S(0)$, we have compared the viscosities in Table 1 with the so calculated values of $S(0)$.

We have used the model potential of Price and the correlation function of Rahman to calculate the longitudinal and transverse frequency modes of $\omega_l(q)$ and $\omega_t(q)$ with wavevector q. Fig. 1 shows that the first minimum in the longitudinal mode lies at a value of $q = 1{\cdot}75$ Å^{-1} which is very close to the value of $q = 1{\cdot}5$ Å^{-1}, where a peak in the structure factor, $S(q)$, occurs in the liquid rubidium. These longitudinal and transverse phonon frequency modes have been used to calculate the low-order frequency moments of the spectral functions of the longitudinal and transverse current correlations. An independent estimute of the frequency moments of both longitudinal and transverse current correlation functions have been made which certainly makes these results more reliable. These results have been employed to calculate the value of longitudinal and shear viscosities in liquid rubidium. To the best of our knowledge an experimental value of the longitudinal viscosity for liquid rubidium is not available. The shear viscosity for liquid rubidium has been measured experimentally[9] at 312 K and is $9{\cdot}05 \times 10^{-3}$ P. Thus the value of shear viscosity obtained by us is smaller than the experimental value by a factor of about two. This difference seems to be due to the fact that model potential of Price does not reproduce the value of measured isothermal compressibility. Thus the modified exponential-type of memory function and Gaussian-type memory function formalism give a good

Table 1—Values of Longitudinal and Shear Viscosities and Relaxation Times

Exponential memory function approach with			Gaussian memory function approach with		
	$S(0) = 0{\cdot}04$	$S(0) = 0{\cdot}02$		$S(0) = 0{\cdot}04$	$S(0) = 0{\cdot}02$
$\tau(0)$	$1{\cdot}474 \times 10^{-12}$ sec	$1{\cdot}318 \times 10^{-12}$ sec	$\tau_{gl}(0)$	$1{\cdot}120 \times 10^{-12}$ sec	$0{\cdot}986 \times 10^{-12}$ sec
η_l	$8{\cdot}420 \times 10^{-3}$ P	$5{\cdot}256 \times 10^{-3}$ P	$\tau_{gt}(0)$	$1{\cdot}003 \times 10^{-12}$ sec	$1{\cdot}003 \times 10^{-12}$ sec
η	$5{\cdot}39 \times 10^{-3}$ P	$4{\cdot}238 \times 10^{-3}$ P	$\eta_\perp$	$6{\cdot}397 \times 10^{-3}$ P	$5{\cdot}825 \times 10^{-3}$ P
			η	$3{\cdot}667 \times 10^{-3}$ P	$3{\cdot}667 \times 10^{-3}$ P

description of frequency moments and viscosities in liquid rubidium at 39°C.

References

1. Forster D, Martin P C & Yip S, *Phys. Rev.*, **170** (1968), 155; **170** (1968), 160.
2. Ailawadi N K, Rahman A & Zwanzig R, *Phys. Rev.*, **A4** (1971), 1616.
3. Gaskell T, *Physics and chemistry of liquids*, **2** (1971), 237.
4. Bansal R, *J. Phys.*, C6 (1973), 1204.
5. Schiff D, *Phys. Rev.*, **186** (1969), 151.
6. Saxena N S & Bhandari R C, *Indian J. pure appl. Phys.*, 15 (1977), 490.
7. Price D L, *Phys. Rev.*, A4 (1974), 358.
8. Rahman A, *Phys. Rev.*, A4 (1974), 1667.
9. Thrope & Rodger, *Phil. Trans. R. Soc. Lond.*, 185 (1895), 397.

Force Field & Vibrational Amplitudes of Alkali Metal Halide Dimers Using Electron Gas Model Data

V Kumar

Department of Physics, M M College, Modinagar 201 204

and

U P Verma & A N Pandey

Molecular Spectroscopy Research Laboratory, Department of Physics, Meerut College, Meerut 250 001

Received 24 *February* 1978; *revised received* 6 *December* 1979

The molecular force constants and mean amplitudes of vibration at temperatures 298·15 and 500 K have been determined using the electron gas model data. The *L-F* approximation method has been applied to evaluate force constants for alkali metal halide dimers, of the type X_2Y_2 (X=Li, Na, K, Rb; Y=F, Cl) and their mean amplitudes of vibration have also been evaluated using Cyvin's secular equation. The reliability of vibrational frequencies has been examined. It has been found that electron gas model data furnish satisfactory results in the case of molecules containing lighter alkali metal atom.

In recent years considerable interest in the study of the properties of alkali metal halide dimers has been developed. Trugman and Gordon[1] studied the vibrational frequencies for some X_2Y_2 type alkali metal halide dimers, assuming the electron gas model. Since their results (with no adjustable parameters) are well comparable to those of previous semi-empirical models[1] with several adjustable parameters and provide the complete set of vibrational frequencies, it was considered worthwhile to apply, for the first time, the *L-F* approximation method[2,3] to evaluate molecular force field, and mean amplitudes of vibration at 298·15 and 500 K. The results of the present study are well supported by the trend observed in experimental dissociation energies[1] for these dimers.

Theory—The planar rhombic X_2Y_2 type system belongs to symmetry group, D_{2h}, and the six vibrational modes are classified according to symmetry type as :

$$\Gamma_{vib} = 2A_g + B_{1g} + B_{1u} + B_{2u} + B_{3u}$$

where the subscripts g represents the gerade modes which are Raman active and u represents ungerade modes which are infrared active.

Wilson's *FG* matrix method[4] has been used in the present study to calculate the force constants in the GVFF model.[4] F and G matrix elements are taken from Lesiecki and Nibler.[5] In order to compute the symmetrized force constants under A_g species, the *L-F* approximation method[2] has been used. The symmetrized mean amplitudes of vibration have been computed using Cyvin's secular equations.[6] The expressions for the root mean-square amplitudes in terms of symmetrized mean-square amplitude matrix elements are determined by introducing symmetry coordinates.[5] The analytical expressions used for bond atom-pairs and non-bond atom-pairs are[3] :

$$U_{X-Y} = [\tfrac{1}{4}\{\Sigma_{11}(A_g) + \Sigma_{33}(B_{1g}) + \Sigma_{55}(B_{3u}) + \Sigma_{66}(B_{2u})\}]^{\frac{1}{2}} \quad \ldots(1)$$

and

$$U_{Y\ldots Y} = [\Sigma_{22}(A_g)]^{\frac{1}{2}} \quad \ldots(2)$$

Results and discussion—The vibrational frequencies[1,5] used in the present computations for alkali metal halide dimers X_2Y_2 (X = Li, Na, K, Rb; Y = F, Cl) are presented in Table 1. Internal force constants evaluated in the present study are summarized in Table 2. It is evident from Table 2 that stretching force constant f_r varies in the order $(f_r)_{X-F} > (f_r)_{X-Cl}$. The trend in the bond distances, energies and experimental dissociation energies[1] for these dimers support this variation in f_r values. Also a comparison in f_r values for X—F and X—Cl

Table 1—Vibrational Frequencies (in $10^2 m^{-1}$) of Alkali Metal Halide Dimers

Molecule	$\nu_1(A_g)$	$\nu_2(A_g)$	$\nu_3(B_{1g})$	$\nu_4(B_{1u})$	$\nu_5(B_{3u})$	$\nu_6(B_{2u})$
Li_2F_2	713	424	522	360	644	609
Li_2Cl_2	471	218	331	226	403	391
Na_2F_2	400	225	325	178	373	368
Na_2Cl_2	252	139	207	111	235	235
K_2F_2	329	153	275	131	305	305
K_2Cl_2	218	106	190	85	207	209
Rb_2F_2	209	103	263	107	283	285
Rb_2Cl_2	170	74	143	67	156	158

Table 2—Internal Force Constants* (in 10^2 Nm^{-1}) of Alkali Metal Halide Dimers

Molecule	f_r	f_{rr}^{*}	f'_{rr}	f''_{rr}	f_R	$f^{\dagger}_{op}$	f_{rR}^{**}
Li_2F_2	1·367	0·461	0·297	0·177	1·319	0·776	−0·526
Li_2Cl_2	0·667	0·235	0·194	0·126	0·595	0·349	−0·272
Na_2F_2	0·869	0·138	0·110	0·027	0·621	0·388	−0·165
Na_2Cl_2	0·484	0·080	0·081	0·030	0·342	0·202	−0·120
K_2F_2	0·713	0·078	0·078	0·012	0 401	0·258	−0·082
K_2Cl_2	0·486	0·047	0·057	0·012	0·251	0·158	−0·073
Rb_2F_2	0·751	0·062	0·071	0·012	0·327	0·210	−0·040
Rb_2Cl_2	0·371	0·034	0·044	0·007	0·197	0·132	−0·937

*f_{rr} is an interaction through a common alkali atom; f'_{rr} an interaction through a common halide atom and f''_{rr} an interaction between opposite sides of the ring

†f_{op} : out-of-plane

**f_{rR} : stretch stretch interaction between bonded (X-Y) and nonbonded (X . X) distances

Table 3—Mean Amplitudes of Vibration (in 10^2 pm) of Alkali Metal Halide Dimers

Molecule	U_{X-Y}		U_{Y-Y}	
	298·15 K	500 K	28·15 K	500 K
Li_2F_2	0·079 (0·070*)	0·089	0 084	0·093
Li_2Cl_2	0·101	0·128	0·124	0·132
Na_2F_2	0·080	0.096	0·093	0·116
Na_2Cl_2	0·102	0·128	0·130	0·164
K_2F_2	0·084	0·103	0·108	0·138
K_2Cl_2	0·099	0·124	0·140	0·179
Rb_2F_2	0·080	0·099	0·114	0·147
Rb_2Cl_2	0·110	0·140	0·150	0·193

*Electron diffraction data from Refs. 7 and 8

bonds shows that the variation is regular except in case of K_2Cl_2 and Rb_2F_2. The reason for such an irregular behaviour in f_r values can be attributed to the inaccuracy in calculation of vibrational frequencies reported in the literature[1] as is reflected from the percentage error in theoretical and experimental values of dissociation energies (the percentage error is 16·2 for K_2Cl_2 and 27·3 for Rb_2F_2). The non-bonded stretching force constant f_R shows the expected trend and a similar behaviour is exhibited by all interaction force constants.

The mean amplitudes of vibration for bonded and non-bonded atom-pairs, (Table 3), are of the right order of magnitude and show the expected variation. It is apparent from Table 3 that, for bonded atom pairs, the mean amplitudes increase with the increase of mass of alkali metal atom except for K_2Cl_2 and Rb_2F_2, the reason being the same as stated for the corresponding f_r values.

It is concluded from the above that electron gas model data furnish satisfactory results in the case of molecules containing lighter alkali metal atom. Since the experimental data for these dimers are rather scanty, the results of the present work will be helpful in the interpretation of electron diffraction data whenever available.

Financial assistance to two of the authors VK and ANP provided by University Grants Commission, New Delhi, is thankfully acknowledged. Another author (UPV) is thankful to CSIR, New Delhi, for the grant of a post-doctoral fellowship.

References

1. Trugman S & Gordon R G, *J. chem. Phys.*, 64 (1976), 4625.
2. Pandey A N, Sharma D K, Verma U P, Arora L D, Gupta S L & Singh B P, *Indian J. pure appl. Phys.*, **14** (1976), 815.
3. Sharma D K, Verma U P, Pandey A N & Kumar V, *Pramana*, 8 (1977), 36.
4. Wilson (Jr) E B, Decius J C & Cross P C, *Molecular vibrations* (McGraw-Hill, New York) 1955, 208.
5. Lesiecki M L & Nibler J W, *J. chem. Phys.*, **63** (1975), 3452.
6. Cyvin S J, *Molecular vibrations and mean square amplitudes* (Elsevier, New York) 1968, 91, 94.
7. Akishin P A & Rambidi N G, *Zh. Neorg. Khim.*, **5** (1960), 23.
8. Akishin P A & Rambidi N G, *Z. phys. Chem.*, **213** (1960), 111.

Estimation of Ground State Wavefunctions & ESR Parameters of Cu^{2+} Ion

B N Misra, Faujdar & Ramesh Babu

Department of Physics, University of Allahabad
Allahabad 211 002

Received 16 *January* 1979; *revised received* 15 *January* 1980

The ground state wavefunctions of Cu^{2+} doped single crystal lattices as well as coordination complexes in powder form, characterized by axially symmetric ESR spectra. have been estimated with the help of M M Zaripov and G K Chirkin theory [*Paramagnetic resonance* (Ist Kzansk. Gos. Univ. Kazan), 196 .] The hyperfine interaction parameters P and Fermi contact term K have also been determined. The signs of hyperfine interaction constants have been discussed on the basis of estimated anisotropy of g-value. The results thus obtained have been found quite satisfactory.

Various important properties of cupric ion and the nature of the interactions when the ion is placed in the crystalline field of ligands can be explained with the

help of ESR studies. Abragam and Bleaney[1-4] developed the theory of paramagnetic resonance on the basis of ESR study of Cu^{2+} ion in tutton salts. The phenomenon of paramagnetic resonance of Cu^{2+} ion arises due to the presence of a hole in its five-fold degenerate $3d^9\ ^2D$ orbitals. When such an ion is placed in a crystalline field its orbital angular momentum is quenched, and this subsequently affects the ESR parameters such as $A_{\parallel}, A_{\perp}, g_{\parallel}, g_{\perp}, K, \lambda$, as well as the electronic wavefunctions of the ground state of the ions.[5,6] Hence, in order to understand the nature of the interactions involved between the ligands and the central ion, the modified values of the ESR parameters and ground state wavefunctions are required. Therefore, the authors have undertaken the present studies in the hope of explaining the effect of very complicated type of the interactions on the physical and chemical properties of the ion in different ligands and the results are reported here.

Theory—The ground state of the Cu^{2+} ion as revealed by spectroscopic data[7] is $3d^9\ ^2D$ and is five-fold degenerate. The degeneracy is being removed by the crystalline field of different symmetries in different ways. The equivalent operator Hamiltonian in presence of cubic field superimposed with tetragonal distortion, as given by Abragam and Bleaney can be written as

$$\mathcal{H} = B_4 (O_4^0 + 5\, O_4^4) + B_2^0\, O_2^0 + B_4^0\, O_4^0 \quad ...(1)$$

where the symbols have their usual meaning.

In this connection, it is necessary to recall an important assumption by Abragam and Bleaney[8], viz. 'any small departure from ideal tetragonal field will not alter the main features of the spectrum and hence the theory is still valid.' Under these circumstances, following the theory of Zaripov and Chirkin,[9,10] the ground state wavefunctions of Cu^{2+} ion placed in the crystal field of different ligands have been calculated and are given in Table 1.

The expressions for spin hamiltonian parameters $A_{\parallel}$ and $A_{\perp}$ in terms of spectroscopic splitting factors $g_{\parallel}$ and $g_{\perp}$ were given by Abragam and Pryce[2] as :

$$A_{\parallel} = P\left[-K + \Delta g_{\parallel} + \frac{3}{7}\Delta g_{\perp} - \frac{4}{7}\right]$$

$$A_{\perp} = P\left[-K + \frac{11}{14}\Delta g_{\perp} + \frac{2}{7}\right] \quad ...(2)$$

where $\Delta g_{\parallel} = g_{\parallel} - 2{\cdot}0023$

$\Delta g_{\perp} = g_{\perp} - 2{\cdot}0023$

The above expressions are valid for the ground state $|x^2-y^2\rangle$ or when $g_{\parallel} > g_{\perp}$. And also the small admixture from the higher configuration (at the same parity) to the ground state $|x^2-y^2\rangle$ has been taken care of by introducing a factor K called 'Fermi contact term'. From Eq. (2) one can easily deduce that

$$\Delta g = \Delta g_{\parallel} - \Delta g_{\perp} = \frac{A_{\parallel} - A_{\perp}}{P} - \frac{9}{14}\Delta g_{\perp} + \frac{6}{7} \quad ...(3)$$

with $\Delta g = g_{\parallel} - g_{\perp}$ ...(4)

Eq. (3) has been used later to discuss the signs of $A_{\parallel}$ and $A_{\perp}$. The necessary experimental data have been taken from previous studies [11-17] and are summarized in Table 2.

Results and discussion — A general survey of the experimental g values suggests the ground state to be $|x^2-y^2\rangle$ with a little admixture of other excited states.[18,19] Using the experimental values of $g_{\parallel}$ and $g_{\perp}$ from Table 2, the ground state wavefunctions (Table 1) have been evaluated.

Although Abragam and Pryce have used Eq. (2) to calculate the ratio $A_{\parallel}/A_{\perp}$ with $P = 0{\cdot}036\ cm^{-1}$ (which is the free ion value), they choose the value of K in such a way that the calculated values of $A_{\parallel}/A_{\perp}$ agree with the observed ones. The values of hyperfine interaction parameters P of Cu^{2+} in crystal lattices or in complexes does not remain the same as that of the free ion value because of the quenched nature of the orbital angular momentum.[6,20] Therefore, values of P and K have been calculated using the experimental values of $A_{\parallel}$ and $A_{\perp}$ (Table 2) for $A_{\parallel}/A_{\perp} > 0$ and $A_{\parallel}/A_{\perp} < 0$ and are reported in Table 1. For both these cases, the values of P have been found to obey the well known theoretical relationship

$$\frac{P}{P_0} \sim \frac{\lambda}{\lambda_0}$$

where $P_0 = 0{\cdot}036\ cm^{-1}$ (the free ion value of P) and λ and λ_0 are the spin-orbit coupling constants of Cu^{2+} ion in complexes and in free ion state respectively. A general survey of these values (Table 1) shows that P values are always less than $0{\cdot}036\ cm^{-1}$, as is expected. The only discrepancy observed is the large value of $P = 0{\cdot}0410\ cm^{-1}$ for $A_{\parallel}/A_{\perp} < 0$ of Cu^{2+} in aspartic acid. So it seems reasonable to assume that the signs of $A_{\parallel}$ and $A_{\perp}$ in aspartic acid are always such that $A_{\parallel}/A_{\perp} > 0$ and in this case the value $P = 0{\cdot}0351\ cm^{-1}$ (Table 1) is acceptable.

Further, the values of K and P obtained from the two sets of calculation seem to be of reasonable magnitude. Hence on this basis no definite assignment of the signs of $A_{\parallel}/A_{\perp}$ can be made. However,

Table 1—Ground State Wavefunctions and ESR Parameters of Cu^{2+} Ion

Samples	Ground state wavefunctions	$A_{\parallel}/A_{\perp} > 0$		$A_{\parallel}/A_{\perp} < 0$	
		K	$\lvert P \rvert \times 10^4$ cm^{-1}	K	$\lvert P \rvert \times 10^4$ cm^{-1}
Cu (II)-Glycine	$0{\cdot}73238 \left\lvert \pm 2, \pm \frac{1}{2} \right\rangle + 0{\cdot}68029 \left\lvert \mp 2, \pm \frac{1}{2} \right\rangle + 0{\cdot}02938 \left\lvert \mp 1, \mp \frac{1}{2} \right\rangle$	0·40221	254·07	0·29863	301·88
Cu (II)-β-Alanine	$0{\cdot}73735 \left\lvert \pm 2, \pm \frac{1}{2} \right\rangle + 0{\cdot}67432 \left\lvert \mp 2, \pm \frac{1}{2} \right\rangle + 0{\cdot}04277 \left\lvert \mp 1, \mp \frac{1}{2} \right\rangle$	0·38127	270·53	0·36740	277·37
Cu (II)-DL-Methionine	$0{\cdot}72763 \left\lvert \pm 2, \pm \frac{1}{2} \right\rangle + 0{\cdot}68576 \left\lvert \mp 2, \pm \frac{1}{2} \right\rangle + 0{\cdot}02167 \left\lvert \mp 1, \mp \frac{1}{2} \right\rangle$	0·38889	255·61	0·28060	301·92
Cu (II)-DL-Valine	$0{\cdot}73464 \left\lvert \pm 2, \pm \frac{1}{2} \right\rangle + 0{\cdot}67803 \left\lvert \mp 2, \pm \frac{1}{2} \right\rangle + 0{\cdot}02469 \left\lvert \mp 1, \mp \frac{1}{2} \right\rangle$	0·41785	245·87	0·27086	317·91
Cu (II)-L-Cystine	$0{\cdot}71766 \left\lvert \pm 2, \pm \frac{1}{2} \right\rangle + 0{\cdot}68607 \left\lvert \mp 2, \pm \frac{1}{2} \right\rangle + 0{\cdot}01549 \left\lvert \mp 1, \mp \frac{1}{2} \right\rangle$	—	—	—	—
Cu (II)-L-Glutamic acid	$0{\cdot}73574 \left\lvert \pm 2, \pm \frac{1}{2} \right\rangle + 0{\cdot}67649 \left\lvert \mp 2, \pm \frac{1}{2} \right\rangle + 0{\cdot}03435 \left\lvert \pm 1, \pm \frac{1}{2} \right\rangle$	0·36383	287·68	0·34873	295·48
Cu (II)-DL-Aspartic acid	$0{\cdot}74069 \left\lvert \pm 2, \pm \frac{1}{2} \right\rangle + 0{\cdot}67079 \left\lvert \mp 2, \pm \frac{1}{2} \right\rangle + 0{\cdot}04037 \left\lvert \mp 1, \mp \frac{1}{2} \right\rangle$	0·41095	351·58	0·33112	410·55
Cu (II)-L-Asparagine	$0{\cdot}73375 \left\lvert \pm 2, \pm \frac{1}{2} \right\rangle + 0{\cdot}67886 \left\lvert \mp 2, \pm \frac{1}{2} \right\rangle + 0{\cdot}02846 \left\lvert \mp 1, \mp \frac{1}{2} \right\rangle$	0·43561	229·11	0·27374	301·71
Cu (II)-*trans* bis (Glycinato) Zinc (II)	$0{\cdot}73020 \left\lvert \pm 2, \pm \frac{1}{2} \right\rangle + 0{\cdot}68299 \left\lvert \mp 2, \pm \frac{1}{2} \right\rangle + 0{\cdot}02024 \left\lvert \pm 1, \pm \frac{1}{2} \right\rangle$	0·45582	208·50	0·23525	296·46
Cu (II) DGBC : substitutional	$0{\cdot}73116 \left\lvert \pm 2, \pm \frac{1}{2} \right\rangle + 0{\cdot}68176 \left\lvert \mp 2, \pm \frac{1}{2} \right\rangle + 0{\cdot}02738 \left\lvert \pm 1, \pm \frac{1}{2} \right\rangle$	0·41906	194·75	0·28052	243·84

Table 2—Experimental Data for $A_{\parallel}$, $A_{\perp}$, $g_{\parallel}$ and $g_{\perp}$

Sample	$g_{\parallel}$	$g_{\perp}$	$A_{\parallel} \times 10^4$ cm^{-1}	$A_{\perp} \times 14^4$ cm^{-1}	Ref.
Cu(II)-Glycine	2·289	2·079	166·18	14·29	11
Cu(II) β-Alanine	2·344	2·115	152·23	1·90	11
Cu(II) DL-Methionine	2·233	2·059	180·45	14·99	12
Cu(II) DL-Valine	2·316	2·065	159·50	20·38	12
Cu(II) L-Cystine	2·232	2·042	175·04	—	13
Cu(II)-Glutamic acid	2·327	2·092	164·59	2·20	14
Cu(II) DL-Aspartic acid	2·384	2·107	195·41	15·12	14
Cu (II)-L-Aspargine	2·305	2·076	154·14	21·08	15
Cu (II) *trans* bis (Glycinato) Zinc (II)	2·264	2·054	155·0	27·0	16
Cu (II) DGBC : Substitutional	2·274	2·074	134·0	15·0	17

Table 3—Calculated and Experimental Values of Δg

Sample or crystal lattice	Calc. value				Exptl. Value
$A_{\parallel}$:	+Ve	− Ve	+ Ve	− Ve	
$A_{\perp}$:	+Ve	− Ve	− Ve	+ Ve	
Cu (II) Glycine	1·40566	0·21002	1·40566	0·21002	0·210
Cu (II) β-Alanine	1·34038	0·22902	1·34038	0·22902	0·229
Cu (II) Methionine	1·46801	0·17339	1·46802	0·17338	0·174
Cu (II) DL-Valine	1·38265	0·25101	1·38265	0·25101	0·251
Cu (II) L-Cystine	—	—	—	—	—
Cu (II) L-Glutamic acid	1·36395	0·23499	1·36394	0·23500	0·235
Cu (II) DL-Aspartic acid	1·30262	0·27704	1·30262	0·27704	0·277
Cu (II) L-Asparagine	1·39052	0·22900	1·39051	0·22901	0·229
Cu (II) *trans* bis (Glycinato) Zinc (II)	1·43780	0·21000	1·43781	0·20999	0·210
Cu (II) DGBC : substituted	1·42207	0·20001	1·42209	0·19999	0·200

the values of P obtained from the negative sign of $A_{\parallel}/A_{\perp}$ are nearer to free ion values; and also the values of K are relatively low, in agreement with the statement that only a small admixture from higher state of some parity is involved in the state $3\,d^9\,{}^2D$. Hence it is reasonable to choose the signs of $A_{\parallel}$ and $A_{\perp}$ in such a way that $A_{\parallel}/A_{\perp} < 0$ except for aspartic acid. Having once decided the sign of $A_{\parallel}/A_{\perp}$, the individual signs of $A_{\parallel}$ and $A_{\perp}$ can be obtained from Table 3, which gives the anisotropy in g values calculated from four possible combinations of signs of $A_{\parallel}$ and $A_{\perp}$ using Eq. (3) and the experimental values of the same. Obviously for the negative signs of $A_{\parallel}/A_{\perp}$, the $A_{\parallel}$ is negative and $A_{\perp}$ is positive as implied by the proper magnitude of g anisotropy. However, for aspartic acid where $A_{\parallel}/A_{\perp} > 0$, $A_{\parallel}$ as well as $A_{\perp}$ are negative.

One of the authors (Faujdar) is thankful to the University Grants Commission, New Delhi, for the financial assistance during this study.

References

1. Abragam A, *Phys. Rev.*, 79 (1950), 534.
2. Abragam A & Pryce M H L, *Proc. R. Soc.*, 206 (1951), 164.
3. Bleaney B, Bowers K D & Pryce M H L, *Proc. R. Soc.*, 228 (1955), 166.
4. Bleaney B & Low W, *Proc. phys. Soc.*, A68 (1955), 55.
5. Chadda C J, *J. phys. Soc. Japan*, 24 (1968), 976.
6. Sastry B A & Chary M N, *Indian J. pure appl. Phys.*, **13** (1975), 866.
7. Bowers K D & Owen J, *Rep. Prog. Phys.*, 18 (1955), 304.
8. Abragam A & Bleaney B, *Electron paramagnetic resonance of transition ions*, (Clarendon Press, Oxford), 1970 372.
9. Zaripov M M & Chirkin G K, *Paramagnetic resonance* (in Russian), No. 3, (Izt. Kzansk. Gos. Univ., Kazan), 1968.
10. Zaripov M M & Chirkin G K, *Soviet Phys. Solid St.*, 6 (1964), 1290.
11. Misra B N & Sharma S D, *J. chem. Phys.*, 63 (1975), 5322.
12. Misra B N & Sharma S D, *J. magn. Reson.* **24** (1976), 8.
13. Misra B N & Sharma S D, *Chem. Phys., Lett.*, Communicated.
14. Misra B N & Sharma S D, *Indian J. pure appl. Phys.*, **14** (1976), 705.
15. Misra B N, Sharma S D & Gupta S K, *Nuovo Cim.*, 42B (1977), 205.
16. Allen H C, Mandrioli M I & Becker J W, *J. chem. Phys.*, 56 (1972), 997.
17. Krishnan V G, Sathyanarayan S G & Sastry G S, *J. chem. Phys.*, 66 (1977), 1715.
18. Boas J F, Pilbrow I R, Hartzwell C R & Smith T D, *J. chem. Soc. (A)*, (1967), 572.
19. Graene F Bryce, *J. phys. Chem.*, 70 (1969), 94.
20. Misra B N & Faujdar, *Indian J. pure appl. Phys.*, **16** (1978), 67.

Study of the Cluster-size in p-Nucleon Interaction at 70 GeV/c

D C Ghosh, S C Naha, J Roy, K Sengupta & M Basu

Department of Physics, Jadavpur University
Calcutta 700 032

Received 9 *February* 1979; *revised received* 16 *November* 1979

The cluster size in the p-ionization region in p-nucleon interactions in emulsion at 70 GeV/c is determined, following a 'model-independent method' proposed in a recent paper by R K Shivpuri & Chandra Gupta [*Phys. Rev.*, D15 (1977), 3332]. It has been observed that the maximum charged particles (pions) constituting a cluster is three at this accelerator energy.

Recently the study of the existence of two-particle correlation in hadronic multiparticle production has provided a strong evidence for cluster formation in hadronic interactions.[1,2] But no detailed information is available regarding the side of the clusters. In a

very recent paper Shivpuri and Gupta[3] have proposed an analytical method to determine the sizes and hence the masses of the clusters. They have been able to show by means of three-, four- and n-particle correlations that clusters of various sizes are formed in nucleon-nucleon interaction at cosmic ray energies in the range 0·1-2600·0 TeV. However, no work has yet been done to determine the cluster size with the help of this 'model-independent method' at accelerator energy levels.

In the present study, we have determined the cluster size in p-nucleon interactions in emulsion at 70 GeV/c with the help of the above mentioned method of Shivpuri and Gupta.[3] We represent the charged secondary particles (designated by strokes) for an event in rapidity space as in Fig. 1. We would not consider the particles at the two ends of the rapidity space since they constitute the leading and target particles. We want to find out the correlations for only the non-diffractive component of the cross-section. Now let us determine two-, three-, four-, etc. particle correlations. For determining two-particle correlation, the rapidity differences (r) of all the adjacent particles (pions) are to be considered.[4]

Next, to determine the three-particle correlation, the rapidity differences of particles 2 and 4, 3 and 5, 4 and 6, etc. are to be determined. The basic reasoning proposed[3] for the existence of three-particle correlation is that if particles, e.g. 2,3, 4 are the decay products of a single cluster, then the rapidity differences between 2 and 3, between 3 and 4 and also between 2 and 4 must be small, i.e. the particles 2, 3, 4 are closely spaced in rapidity. Since the rapidity difference between 2 and 3 and between 3 and 4 is already considered in two-particle correlation, the additional constraint for three-particle correlation to exist is that the rapidity difference between the particles 2 and 4 must be small.

Next, one can find four-particle correlations by considering the rapidity difference between the particles 2 and 5. The reason is that one has already determined the rapidity difference between the combinations of particles 2 and 3, 3 and 4, 4 and 5, 2 and 4, and 3 and 5, in the determination of two-particle and three-particle correlations and if the rapidity differences for all the above mentioned combinations of particles plus those for particles 2 and 5 are small, the correlations are present among all the four particles. In this way, one can find out five-particle or six-particle correlations. In general, n-particle correlation is shown by the distribution of the rapidity difference between the first and the nth particle in rapidity space.

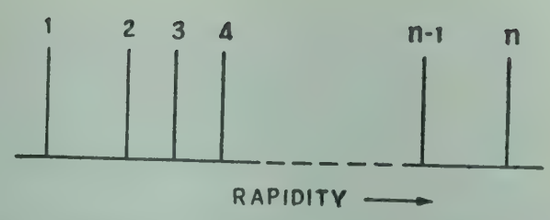

Fig. 1—Schematic representation of charged secondary particles in rapidity space.

In the present investigation, a set of BR-2 photoemulsion plates of dimension 10 cm × 10 cm × 400 μm exposed to 70 GeV/c proton beam of the Serpukov proton synchroton has been used. The scanning of the plates was performed on a Leitz-Wetzlar microscope provided with a Brower travelling stage. Plates were scanned using an oil immersion 53·1 × objective in conjunction with a 16·8 × ocular.

The events were chosen utilizing tne following criteria: (i) the beam track must be $\leqslant 3°$ to the mean beam direction in the pellicle, (ii) interaction should not be within the top or bottom 20 μ m thickness of the pellicle, and (iii) events should have no blob at the point of production. Further, all primary beam tracks were followed back to be sure that the events chosen do not include interactions from the secondary tracks of other interactions. The primaries originating from other interactions were observed and the corresponding events were removed from the sample. All the secondary tracks with grain density $g^* < 1{\cdot}4\, g_{min}$ were taken as pions, since these tracks are primarily due to pions. To ensure the best approximation for a nucleon-nucleon collision, the events with $N_h \leqslant 2$ and $n_s \leqslant 12$ were taken. With the above selection criteria 300 events were chosen for the analysis. The space angles of all the pions were measured with the help of a goniometer in the laboratory system[5,6] and hence the rapidities of all the particles were calculated using the earlier reported relation.

The rapidity differences (r) for two-,three-,four- and five-particles were calculated for all interactions.

To find out the two-particle correlation, we plot dn/dr against r. Fig. 2 shows the distribution of rapidity difference between adjacent particles ($r = y_2 - y_1$) where y_1 and y_2 are the rapidities of the two adjacent particles. The sharp peak in the distribution for low values of r clearly indicates the existence of two-particle correlation.

The distribution of the rapidity difference between the two alternate particles $r = y_3 - y_1$ of various combinations is shown in Fig. 3, where y_3 and y_1 are the rapidities of the two alternate particles. Again the plot clearly shows a three-particle correlation.

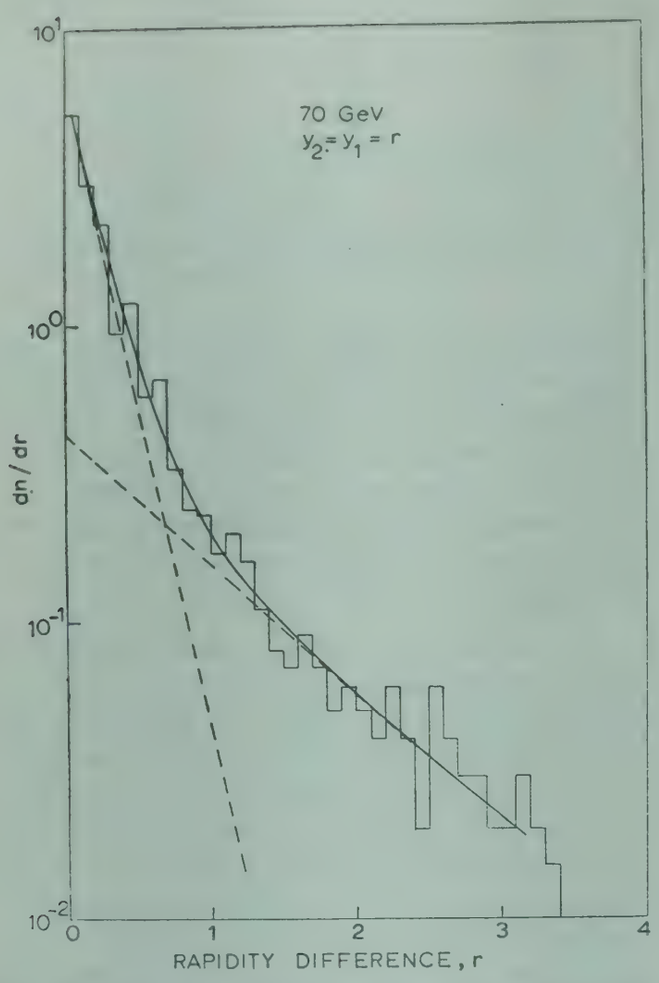

Fig. 2—Rapidity difference distribution of charged secondary particles for two adjacent particles

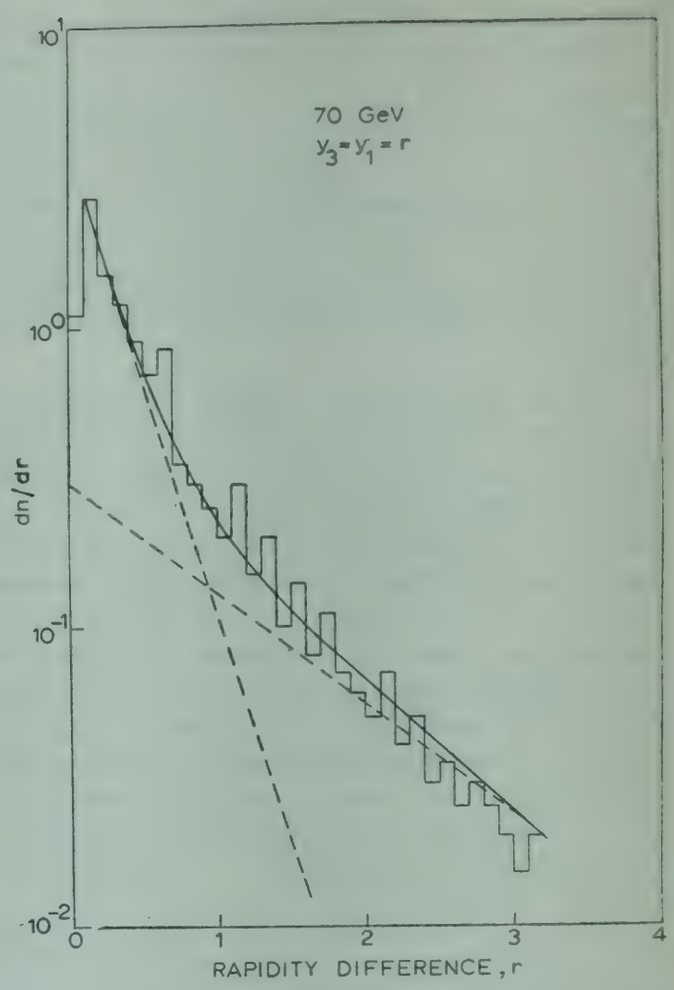

Fig. 3—Rapidity difference distribution of charged secondary particles for first and third particles

The four- and five-particles rapidity difference distributions are shown in Fig. 4 where no sharp peak is observed. Hence four-and five-particle correlations do not exist in these interactions.

According to Snider,[7] the two-particle rapidity difference distribution in high energy p-p collision is of the form

$$\frac{dn}{dr} \quad Ae^{-Br} + Ce^{-Dr} \qquad \ldots(1)$$

This is expected on the basis of multiperipheral model. In the present investigation, we have observed that the distributions for various combinations of particles also follow the same form as given in Eq. (1). The numerical equations of the theoretical curves represented by the solid line in Figs. 2 and 3, for two-particle and three-particle rapidity difference distributions are as follows:

$$\frac{dn}{dr} = 6{\cdot}25\, e^{-5{\cdot}01r} + 0{\cdot}46 e^{-1{\cdot}03r} \qquad \ldots(2)$$

$(\chi^2/D.O.F. = 42/34)$

$$\frac{dn}{dr} = 3\,48\, e^{-4{\cdot}16r} + 0{\cdot}5\, e^{-1{\cdot}01r} \qquad \ldots(3)$$

$(\chi^2/D.O.F. = 31/32)$

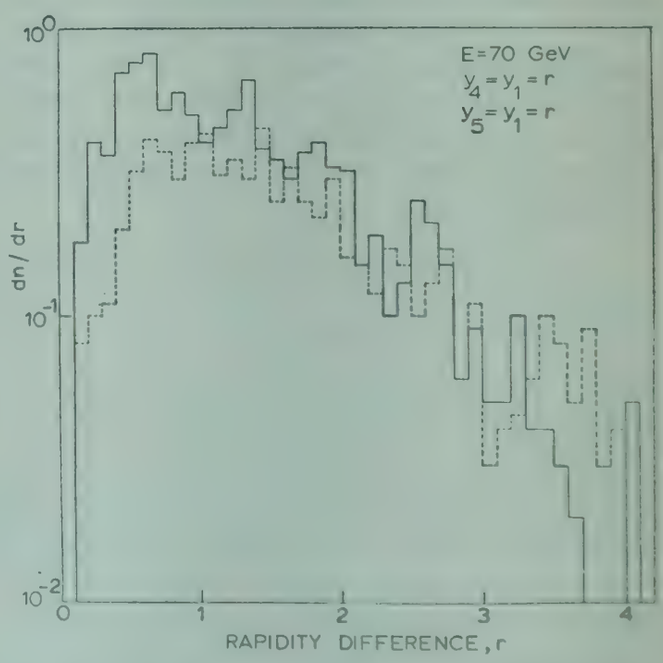

Fig. 4—Rapidity difference distribution of charged secondary particles for first and fourth particle (solid line) and first and fifth particle (dashed line)

The contributions of the two individual terms in Eqs. (2) and (3) are represented by the dashed lines in Figs. 2 and 3.

We can infer from the above equations that the value of the slope D in the second term is not a sensitive parameter; rather the value of the slope B provides a measure of the strength of the correlation. Also it is seen that with the increase of the number of particles in a cluster, the strength of the correlation tends to decrease. These results are in agreement with those of Shivpuri and Gupta.[3]

Thus from the above analysis, we conclude that the maximum number of charged particles constituting a cluster at 70 GeV is three, although two-particle clusters are also present in the interaction. It would be interesting and worthwhile to determine the cluster size, with this method at different accelerator energies for a better understanding about the dynamics of cluster formation at high energies.

The authors are deeply indebted to Prof. K D Tolostov of Dubna, USSR, for kindly supplying the exposed emulsion plates.

References

1. Slansky R, *Phys. Rev.*, **11C** (1974), 99.
2. Berger E L, *Nucl. Phys.*, **B85** (1975), 61.
3. Shivpuri R K & Chandra Gupta, *Phys. Rev.*, **D15** (1977), 3332.
4. Shivpuri R K, Chandra Gupta, Tarachand & Singh T, *Phys. Rev.*, **D19** (1979), 391.
5. Ghosh D C, Bhattacharjee D K, Daftari I K, Roy Chowdhury A, & Roy T, *Phys. Rev.*, **D19** (1979), 391.
6. Roy Chowdhury A, Daftari I K, Roy T & Ghosh D C, *Phys. Rev.*, **D13** (1976), 1502.
7. Snider D R, *Phys. Rev.*, **D11** (1975), 140.

Nuclear-Decay Data—The Statement of Uncertainties

At the annual general meeting of the International Committee for Radionuclide Metrology (ICRM) held in June 1979, at the Physikalisch-Technische Bundesanstalt, it was suggested that letters should be sent to the editors of journals that publish *nuclear-decay data*, drawing attention to *the need for specific statements of the uncertainties* that are associated with such data. Authors frequently fail to state clearly the nature of their estimates of uncertainty, and not all editors insist on such clarity, so that evaluators of nuclear-decay data often find that it is necessary to consult with the individual authors to arrive at the weighting factors appropriate to their data. If uncertainties could be clearly characterized in the abstracts or in the text of paper reporting values of nuclear parameters, there would be a corresponding shortening of the time required for the data to be evaluated and tabulated.

There are many methods of stating estimates of conventional random and systematic uncertainties that are acceptable, *provided that the methods used are described.* Thus random error may be stated as: (i) the estimate of the standard deviation (or the square root of the variance), which is in the same units as the observed data and indicates the order of magnitude of the spread of the data; (ii) the standard error (or the estimated standard deviation of the mean of the distribution); and (iii) the estimated limits for the mean at stated levels of confidence (CL), [e.g. limits at the 99% CL define the range within which there is a 99% probability of including the mean of a population]. Provided that the author states the number of independent measurements made of the given parameter, or the number of degrees of freedom, these statements of random uncertainty are related uniquely to each other.

The other component of the overall uncertainty is the estimate of possible systematic error. The significance, or meaning, of the estimate of systematic uncertainties should be clearly stated and also related to the method chosen to state the random uncertainties. Thus an estimate of maximum conceivable systematic uncertainties would logically be combined with a random uncertainty at a 99% confidence level. An appropriate fraction of the estimate of maximum conceivable systematic uncertainty would be chosen to match smaller random confidence levels. The methods used to combine random and systematic uncertainties should also be stated by authors, and an explicit listing of all components of these uncertainties will allow an evaluator of nuclear data to 'unravel' the statements of uncertainty and to choose weighting factors that are consistent for all the data to be evaluated. The need for expressing all nuclear-data measurements with the greatest possible clarity has been forcefully emphasized by Schmidt and Bartholomew.[1]

The philosophy of the estimation and statement of overall uncertainty is currently being studied by specialists at the Bureau International des Poids et Mesures, and their conclusions will be duly reported.

This short note has been discussed, directly or indirectly with Y Le Gallic, D D Hoppes, J Legrand, J S Merritt, J W Muller, T Radoszewski, A Rytz, and S Wagner, all of whose many and diverse opinions, I have attempted to combine into an acceptable whole. All these colleagues are, however, agreed that irrespective of the philosophical approaches to the treatment of uncertainty, all estimates of the parts of stated uncertainties should be fully enumerated and carefully evaluated.

References

1. Schmidt J J & Bartholomew G A, Presentation of Results of Nuclear Data Measurements, Int. J. appl. Radiat. Isotopes, 26 (1975), 45.

W B Mann
President, International Committee
for Radionuclide Metrology
National Bureau of Standards
Washington D C 20234 USA

INSTRUCTIONS TO CONTRIBUTORS

Manuscripts should be typewritten in double space and on *only one side* of good quality paper; the original and *one carbon copy are to be submitted.*

Papers must be written in clear and concise English. Good attention to spelling and grammar should be given. Long introductions should be avoided. Standard international nomenclature should be followed in giving names of chemical compounds. Standard abbreviations for units of measurement should be used in the text, tables and illustrations. The abbreviations should be used without fullstops.

Title—The title should be neither too brief/general nor unnecessarily long. It should reflect the content of the paper so as to derive the maximum advantage in indexing and information retrieval. A short title for use as running title should also be supplied. If a paper forms part of a series, a subtitle indicating the aspects of the work covered in the paper should be provided.

Abstract—The abstract should indicate the scope of the work and the principal findings of the paper. It should not exceed 3% of the length of the paper and, barring exceptional cases, it should not exceed 200 words. The abstract should be prepared in such a form that abstracting periodicals can use it without modification.

Data—Only such primary data as are essential for understanding the discussion and the main conclusions emerging from the study should be included. All such secondary data as are of interest to a specific category of readership may, if necessary, be deposited in the editorial office (or retained by the authors) for supply on demand. A footnote to this effect may be inserted at a suitable place in the paper.

Mathematical portions—Special attention should be given to the mathematical portions of the paper. Equations must be well separated from the text and written clearly with good separation between the successive lines. The usual norms of breaking long mathematical expressions may be adhered to. Equations should be numbered consecutively in Arabic numerals with the number in parentheses near the right hand margin. Superscripts and subscripts should be clearly indicated in pencil by $\vee$ and $\wedge$ sign respectively. Capital and small letters, particularly of the same letter when both occur, as well as letters or symbols likely to be confused one for the other, should be clearly distinguished. Special characters (e.g. Greek, script, vector, tensor, matrix, etc.) required must be indicated by marginal notes. Letters and symbols which should appear in bold face must be clearly indicated. To simplify typesetting: (i) long and complicated mathematical expressions which are frequently repeated should be replaced with single letter/symbol, without clashing with the others used in the paper; (ii) the "exp" form of complex exponential functions should be used: and (iii) to simplify fractions, the solidus (/) is to be used and fractional exponents are to be used instead of root signs, e.g.

write $\left(4\omega_{pl} K^2_{s\lambda} \Big/ \tilde{\omega}\ K^2_D\right)^{1/2}$ and *not* $\sqrt{4\dfrac{\omega_{pl} K^2_{s\lambda}}{\tilde{\omega}\ K^2_D}}$

write $\exp\{-i\omega_0 (t_1-t_2)/2\}$ and *not* $e^{-i\omega_0 (t_1-t_2)/2}$

Tables—Tables should be typed *on separate sheets* of paper without any text matter on the page. They should be numbered consecutively in Arabic numerals and should bear brief titles. *Column headings should be brief.* Units of measurements should be abbreviated and placed below the headings. Nil results should be indicated and distinguished clearly from absence of data. Graphs as well as tables, both representing the same set of data, must be strictly avoided. Inclusion of structural formulae inside the tables should be avoided as far as possible. Tables should be referred to in the text by numbers and not by terms like 'above', 'below', 'preceding' or 'following'.

Illustrations—All illustrations should be numbered consecutively in Arabic numerals. Captions and legends to the figures should be self-explanatory and should be typed on a separate sheet of paper and attached at the end of the manuscript. Line drawings should be made with Indian ink on white drawing paper (perferably Bristol board), cellophane sheet or tracing cloth. In addition to the originals, a set of blue-prints or photostat copies should be sent. For satisfactory reproduction, the graphs and line drawings should be drawn to approximately twice the printed size.

The lettering should be uniform, perferably in stencil, so as to be *not less than 2 mm after reduction* widthwise to 3" or 6" as required. The size of geometrical shapes (used to distinguish different graphs), dot, lines, etc. should be sufficiently large to permit the necessary reduction without loss of detail. In the case of *photographs*, prints *must be on glossy paper and contrasty*. If an illustration is taken from another publication, reference to the source should be given and prior permission secured. Illustrations should be protected by thick cardboard packing against creases, folds and broken corners during transit. Illustrations should be referred to in the text by numbers and not by terms like 'above', 'below', 'preceding' or 'following,.

Infrared, ultraviolet, NMR and other spectra, DTA curves, etc. should be included only if they pertain to new compounds and/or are essential to the discussion; otherwise only significant numerical data should be included in the text.

References—The list of references should be prepared strictly in accordance with the style followed

in the Journal. In the text, references to literatures should be numbered consecutively, in the order of their first occurence, and should be indicated by superscripts at the relevant places; as far as possible the placement of references on numerals of other symbols should be avoided; in such cases the reference may be given in parentheses in running text, e.g. "this yielded for n a value of 2·3 (Ref. 5)". Full bibliographic details for all the references mentioned in the text should be listed in serial order at the end of the paper.

In citing references to research papers, names and initials of authors should be followed, in order, by the title of the periodical in the abbreviated form (underlined), the volume number (two lines underneath), the year within circular brackets and the page reference [e.g. Venkatesh, H G & Guha Sarkar, G, *Indian J. pure appl. Phys.*, 12 (1974), 502]. For names of periodicals, the standard abbreviations listed in the *World list of scientific periodicals* edited by P Brown & G B Stratton (Butterworths & Co. Ltd, London), 4th Edition, 1963-65, should be used. If the reference is to an article published without any authorship in a periodical, the title of the article takes the place of the author in the citation [e.g. The content, influence and value of scientific conference papers and proceedings. *Unesco Bull. Ltbr.*, 16 (1952), 113-26.]. If a paper has been accepted for publication, the names of the authors and the journals should be given followed by the words "in press" within circular brackets [e.g. Sastry, B. A. & Sastry, G. S., *Physica*, (in press).].

In the list of references, unpublished work, accepted papers in press and personal communications should be clearly distinguished.

Even if a reference contains more than two authors, the names of all the authors with their respective initials should be given. The abbreviations *et al.*, *idem* and *ibid* should be avoided.

Reference to a book should include details in the following order: names and initials of authors, the title of the book (underlined), name of publisher and place of publication within circular brackets and year [e.g. Herzberg, G, *Spectra of diatomic molecules* (D Van Nostand & Co. Inc., New Jersey), 2nd Edn, 1950, 31.]. If the reference is to the work of an author published in a book by a different author or edited by a different person, the fact that it is cited from the source book should be clearly indicated [e.g. Garlick, G F J, cited in *Encyclopedia of Physics*, Vol. 26—*Light and matter* II, edited by S Flugge (Springer Verlag, Berlin), 1958, 1.].

Proceedings of conferences and symposia should be treated in the same manner as books. Reference to a paper presented at a conference, the proceedings of which are not published, should include, in the following order, names and initials of authors, title of the paper (underlined), name of the conference, place where the conference was held and date (Deekshitulu, B L, *Design and fabrication of drum scanner for picture processing*, paper presented in the Symposuim on Applied Optics, Indian Institute of Science, Bangalore, 28-30 Nov. 1974).

Reference to a thesis should include the name of the author, title of the thesis (underlined), university or institution to which it was submitted and year of submission (e.g. Chandrasekaran, K S., *Studies on crystal structure and absolute configuration of crystals*, Ph. D. thesis, Madras University, 1956).

Reference to a patent should include names of patentees, country of origin (underlined) and patent number, the organization to which the patent has been assigned within circular brackets, data of acceptance of the patent and reference to an abstracting periodical where available [Trepagnier, J H, *US Pat.* 2,463,219 (to E I du Pont de Nemours & Co.), 1 March 1949, *Chem. Abstr.*, 43 (1949), 7258.].

Abbreviations and symbols—Abbreviations used should conform to the style of the journals. The following prefixes to units of measurements may be used for expressing submultiples and multiples.

Submultiples	*Abbreviation*	*Multiples*	*Abbreviation*
Deci- ($=10^{-1}$)	deci	deca- ($=10^{1}$)	deca-
centi- ($=10^{-2}$)	c	hecto- (10^{2})	hecto
milli- (10^{-3})	m	kilo- ($=10^{3}$)	k
micro- ($=10^{-6}$)	μ	mega- ($=10^{6}$)	M
nano- ($=10^{-9}$)	n	giga- ($=10^{9}$)	G
pico- ($=10^{-12}$)	p	tera- ($=10^{12}$)	T
femto- ($=10^{-15}$)	f		
atto- ($=10^{-18}$)	at		

Frequently repeating combinations of words, e.g. electric field gradient (EFG), junction field effect transistor (JFET), stimulated Raman emission (SRE), should be abbreviated subsequently, indicating the abbreviated form in parentheses, as shown, at the place of their first occurrence,

Nomenclature—Where too many symbols are used in the text, a section entitled "Nomenclature", explaining the significance of the various symbols, may be given and placed just above the Acknowledgement section.

Acknowledgement—Acknowledgements should not be exuberant and must be made only to real assistance rendered in connection with the work reported in the paper.

Appendixes—Appendixes, typed on separate sheets, should be numbered consecutively, in Arabic numerals, in the order of their occurence in the text, and should be placed at the very end of the paper.

Printed and Published by Shri D S Sastry, Publications & Information Directorate, Council of Scientific & Industrial Research, New Delhi, at the Leipzig Press, D-52 South Extension Part I, New Delhi 110 049, India

Regd. D-(C)-540